

Extremely Nonlinear Optics with wavefront controlled ultra-short laser pulses

Dissertation zur Erlangung des
naturwissenschaftlichen Doktorgrades
der Julius-Maximilians-Universität Würzburg

Julius-Maximilians-

**UNIVERSITÄT
WÜRZBURG**

vorgelegt von
Stefan Eyring

aus Wassertrüdingen

Würzburg 2011

Extremely Nonlinear Optics with wavefront controlled ultra-short laser pulses

Dissertation zur Erlangung des
naturwissenschaftlichen Doktorgrades
der Julius-Maximilians-Universität Würzburg

vorgelegt von
Stefan Eyring

aus Wassertrüdingen

Würzburg 2011

Eingereicht am 30. Juni 2011
bei der Fakultät für Physik und Astronomie

1. Gutachter: Prof. Dr. C. Spielmann

2. Gutachter: Prof. Dr. B. Hecht

der Dissertation.

1. Prüfer: Prof. Dr. C. Spielmann

2. Prüfer: Prof. Dr. B. Hecht

3. Prüfer: Prof. Dr. H. Hinrichsen

im Promotionskolloquium.

Tag des Promotionskolloquiums: 21. Juni 2012

List of Publications

Parts of this work have been published previously in the following articles.

Journal articles

- D. Walter, S. Eyring, J. Lohbreier, R. Spitzenpfeil, and C. Spielmann
Spatial Optimization of Filaments
Appl. Phys. B **88**, 175-178, (2007)
- J. Lohbreier, S. Eyring, R. Spitzenpfeil, C. Kern, M. Weger, and C. Spielmann
Maximizing the brilliance of high-order harmonics in a gas jet
New J. Phys. **11**, 023016, (2009)
- R. Spitzenpfeil, S. Eyring, C. Kern, C. Ott, J. Lohbreier, J. Henneberger, N. Franke, S. Jung, D. Walter, M. Weger, C. Winterfeldt, T. Pfeifer, and C. Spielmann
Enhancing the brilliance of high-harmonic generation
Appl. Phys. A **96**, 69-81, (2009)
- S. Eyring, C. Kern, M. Zürch, and C. Spielmann
Improving high-order harmonic yield using wavefront-controlled ultrashort laser pulses
Opt. Expr. **20**, 5601-5606, (2012)

Conference contributions

- S. Eyring, J. Lohbreier, R. Spitzenpfeil, D. Walter, and C. Spielmann
Optimization and characterization of shaped high harmonic radiation
Ultrafast x-ray science workshop at BESSY, Berlin, Germany (2006)
- S. Eyring, J. Lohbreier, R. Spitzenpfeil, D. Walter, M. Weger, and C. Spielmann
Optimierung und Charakterisierung von Filamenten
Frühjahrstagung der Deutschen Physikalischen Gesellschaft, Düsseldorf, Germany (2007)

-
- J. Lohbreier, S. Eyring, R. Spitzenpfeil, and C. Spielmann
Optimization and Characterization of high-order harmonics by spatial shaping before the filament
Meeting of the SPP 1134, Munich, Germany (2007)
 - J. Lohbreier, S. Eyring, R. Spitzenpfeil, and C. Spielmann
Adaptive Shaping of High-order harmonics
ATTO 07, International Conference on Attosecond Physics, Dresden, Germany (2007)
 - S. Eyring, J. Lohbreier, R. Spitzenpfeil, D. Walter, M. Weger, and C. Spielmann
Optimierung und Charakterisierung von Filamenten
Frühjahrstagung der Deutschen Physikalischen Gesellschaft, Düsseldorf, Germany (2007)
 - S. Eyring, J. Lohbreier, R. Spitzenpfeil, M. Weger, and C. Spielmann
Spatial characterization and wavefront measurements of high-order harmonics
Frühjahrstagung der Deutschen Physikalischen Gesellschaft, Darmstadt, Germany (2008)
 - S. Eyring, C. Kern, J. Lohbreier, R. Spitzenpfeil, M. Weger, and C. Spielmann
Measuring the wavefront of high harmonics
Meeting of the SPP 1345, Jena, Germany (2008)
 - S. Eyring, C. Kern, J. Lohbreier, R. Spitzenpfeil, M. Weger, and C. Spielmann
Analysis of the brilliance of high-order harmonics
441. WEH Seminar: “Ultrafast x-ray methods for studying transient electronic structure and nuclear dynamics”, Bad Honeff, Germany (2009)

Foreword

Curiosity is one of humanity's major driving forces. Even children try to learn as much as possible about their surroundings by asking the famous "why" and "how" questions which often lead to the first (scientific) insights in the life of every human being. Over centuries many of these questions were asked, fundamental laws discovered, and processes developed to control and alter our everyday environment. These discoveries led to famous inventions like the steam engine, the combustion engine or the laser.

With the development of the laser by T. Maiman in 1965, a source of coherent radiation with unprecedented optical and temporal properties was finally available. This first ruby laser produced pulses with a duration of a few ns. Further development in the field of laser sources led to the invention of new types of lasers with ever shorter pulse durations. Today Ti:Sapphire oscillators deliver ultra-short laser pulses with a duration of only a few femtoseconds ($1 \text{ fs} = 10^{-15} \text{ s}$). With the help of these oscillators and the development of chirped-pulse amplification by G. Mourou in 1985, laser light with peak intensities of several TW/cm^2 can be created.

The high intensities created by modern lasers lead to many new and interesting effects. In our everyday experience most processes are of a linear nature. One example which can be easily understood is the field of music. By turning up the volume of music, i.e., increasing the amplitude of the sound wave, the music gets louder linearly. When reaching a certain amplitude the maximum capacity of the amplifier or speaker is reached and the linear behavior is no longer true, i.e., the music starts clipping. Similar effects can be seen in the interaction of laser light with matter. When reaching certain intensities several nonlinear processes gain importance. The scientific field describing these effects is called the field of nonlinear optics. In case of very high (peak) intensities, even "conventional" nonlinear optical theories cannot describe the resulting extremely nonlinear effects.

One of the extremely nonlinear optical effects discussed in this work is the generation of high-order harmonic radiation of a driving laser pulse. This effect generates photons with energies being integer multiples of the photon energies of the driving laser pulse with high orders. This typically results in a spectral conversion of near infrared laser light into the XUV (10 nm-100 nm) regime. With this technique, harmonic orders even greater than 450 can be obtained, resulting in radiation in the soft X-ray regime ($< 10 \text{ nm}$). The light generated this way is unique in many ways. It shares many of the properties of the driving laser pulse, and the process of high-order harmonic generation is a source of spatially and temporally coherent radiation.

In fact, the pulses generated by this process are the shortest events humans have ever produced, some being only as short as 63 as (1 as = 10^{-18} s).

When talking about optical phenomena it is necessary to keep in mind that light can be described as photons as well as waves. In order to completely describe a wave, information about the amplitude and the phase are necessary. For many of the nonlinear effects mentioned above to be efficient, the phase plays a very important role. In case of laser beams, the spatial phase distribution is called wavefront. As the efficiency of nonlinear effects depends on the phase, the main question discussed in this work will be:

How does the wavefront of ultra-short laser pulses influence extremely nonlinear optical processes?

Contents

List of Publications	iii
Foreword	v
I Laser pulses, Wavefronts and Extremely Nonlinear Optics	1
1 Beam optics	3
1.1 Basics	3
1.2 Gaussian beam optics	8
1.3 Real laser beams	10
2 Wavefronts	15
2.1 The concept of wavefronts	15
2.2 The Zernike polynomials	18
2.3 The Shack–Hartmann sensor	19
2.4 The wavefront and beam propagation	24
3 Ultra-short laser pulses & nonlinear optics	27
3.1 Ultra-Short Laser Pulses	28
3.2 Basics of Nonlinear Optics	30
4 Filamentation of ultra-short laser pulses	33
4.1 Fundamentals of filamentation	33
4.2 Filamentation of ultra-short laser pulses	37
5 High-order harmonic generation (HHG)	39
5.1 Single Atom Response	40
5.2 Phase matching	48
II Experiments	55
6 The experimental setup	57
6.1 Laser system	58
6.2 Spatial Light Modulator	59
6.3 Temporal compression	61
6.4 Beam and pulse diagnostics	62
6.5 High-order harmonic generation	63

7	Spatial optimization of filaments	65
7.1	Experimental setup	66
7.2	Spatial properties after filament	67
7.3	Spatial optimization of filaments	69
7.4	Optimization of HHG after filamentation	73
7.5	Conclusion	74
8	The wavefront of high-order harmonics	75
8.1	Experimental setup	76
8.2	The measurement	77
8.3	Experimental results	80
8.4	Conclusion	86
9	HHG with wavefront controlled pulses	87
9.1	Experimental setup	87
9.2	The measurement	89
9.3	Experimental results	90
9.4	Conclusion	97
10	Summary	99
11	Zusammenfassung	101
III	Appendices	103
A	Second-order beam moments	105
B	Zernike Polynomials	109
B.1	Fundamentals of the Zernike polynomials	109
B.2	Explicit expression of the Zernike polynomials	110
B.3	Using and Interpreting Zernike polynomials	112
C	The genetic algorithm	117
C.1	Basics	117
C.2	Parameterization	118
D	McPherson 248/310G	121
D.1	Basics	121
D.2	Detection & Spectral foreshortening	122
D.3	Mapping detector position to wavelength	124
D.4	The spectrometer software	128
IV	Lists and Literature	133
	Bibliography	135

List of Figures 147

List of Tables 149

Part I

Laser pulses, Wavefronts and Extremely Nonlinear Optics

Chapter 1

Beam optics – Principles, properties and propagation

When dealing with extremely nonlinear optics and wavefront controlled ultra-short laser pulses, many basic ideas of optics are still valid. Sometimes even the most classical models can give surprisingly accurate results.

For example, the high-order harmonic generation is actually an extreme nonlinear process. Nevertheless, when treating the electron in the laser-field as a simple particle and using classical motion, as discussed in Chapter 5, many results can be explained correctly.

Because of the importance of many basic principles even for extremely nonlinear processes, the principles and properties of beam optics are discussed here.

1.1 Basics

Maxwell's equations relate the electric and the magnetic fields to their sources. As such they are the fundamental equations for all electro-magnetic effects.

1.1.1 Maxwell's equations

When using the Gaussian CGS system [1] Maxwell's equations can be written as

$$\nabla \cdot \vec{D} = 4\pi\rho, \quad (1.1a)$$

$$\nabla \cdot \vec{B} = 0, \quad (1.1b)$$

$$\nabla \times \vec{E} = -\frac{1}{c_0} \frac{\partial \vec{B}}{\partial t}, \quad (1.1c)$$

$$\nabla \times \vec{H} = \frac{4\pi}{c_0} \vec{j} + \frac{1}{c_0} \frac{\partial \vec{D}}{\partial t}, \quad (1.1d)$$

where \vec{E} and \vec{D} are the electric quantities and \vec{H} and \vec{B} are the magnetic quantities, respectively. The electric and magnetic fields are \vec{E} and \vec{H} . The quantities \vec{D} and \vec{B} are the electric flux density and the magnetic flux density. The sources are denoted as ρ for the electric charge density and \vec{j} as the electric current density.

To determine the field distribution from Maxwell's equation additional information is needed on how substances react and change the fields generated by the sources. For isotropic media the material equations are expressed by

$$\vec{j} = \sigma \vec{E}, \quad (1.2a)$$

$$\vec{D} = \epsilon \vec{E}, \quad (1.2b)$$

$$\vec{B} = \mu \vec{H}. \quad (1.2c)$$

The specific conductivity σ and the dielectric permittivity ϵ describe how a substance reacts to electric fields. The magnetic permeability μ quantifies the response to magnetic fields.

For a part of the field where no currents ($\vec{j} = 0$) and no charges ($\rho = 0$) are present the general wave equation

$$\nabla^2 \vec{E} - \frac{\epsilon \mu}{c_0^2} \frac{\partial^2 \vec{E}}{\partial t^2} = 0 \quad (1.3)$$

can be derived from Equations (1.1) and (1.2). Here Equation (1.3) is only given for the electric field \vec{E} , but has exactly the same structure for the magnetic field \vec{H} .

1.1.2 The wave equation

The solutions of the general wave equation as given by Equation (1.3) are electromagnetic waves which propagate with the phase velocity c . Inside a medium the propagation velocity changes to

$$c = \frac{c_0}{n} \text{ with } n = \sqrt{\epsilon \mu} \quad (1.4)$$

where n is the index of refraction and ϵ and μ are the material parameters.

To describe the propagation of waves, it is convenient to define a vector \vec{k} which contains information about the propagation. This vector \vec{k} is called the wave vector and points in the direction of the propagation of the wave. For propagation through vacuum the vector has a value of

$$k_0 = \frac{2\pi}{\lambda_0} = \frac{\omega}{c_0}. \quad (1.5)$$

For propagation through media the propagation speed inside the medium, defined by Equation (1.4), has to be taken into account. This then leads to

$$k = n k_0. \quad (1.6)$$

The number k is typically called wave number and this definition is used in this work. In spectroscopy on the other hand the term wavenumber is used for the quantity $\kappa = \frac{1}{\lambda}$ which differs from k by a factor of 2π .

For a principle discussion let's consider the general wave equation in the form [2]

$$\nabla^2 u - \frac{1}{c^2} \frac{\partial^2 u}{\partial t^2} = 0. \quad (1.7)$$

All functions $u(\vec{r}, t)$ which satisfy Equation (1.7) are possible electro-magnetic waves. Furthermore, if two waves $u_1(\vec{r}, t)$ and $u_2(\vec{r}, t)$ are solutions of the wave equation, the wave resulting from the superposition $u(\vec{r}, t) = u_1(\vec{r}, t) + u_2(\vec{r}, t)$ is also a valid solution. This principle of superposition results directly from the linearity of Equation (1.7).

As a result it is possible to describe arbitrary waves as a superposition of harmonic waves. For this reason the principles of harmonic analysis and the Fourier transform can be used to examine the properties of electro-magnetic waves. To simplify the problem it is convenient to start with a monochromatic harmonic wave with angular frequency ω . The real wave function $u(\vec{r}, t)$ can be treated as the real part of a complex wave function

$$U(\vec{r}, t) = U(\vec{r}) e^{-i\omega t}. \quad (1.8)$$

where $U(\vec{r})$ is the complex amplitude of the complex wave function. The complex wave function then completely describes the monochromatic wave. The real wave function can be retrieved by

$$u(\vec{r}, t) = \Re \{ U(\vec{r}) e^{-i\omega t} \} = \frac{1}{2} [U(\vec{r}) e^{-i\omega t} + U^*(\vec{r}) e^{i\omega t}] \quad (1.9)$$

with $U(\vec{r}) = a(\vec{r}) e^{i\phi(\vec{r})}$.

Because $U(\vec{r}, t)$ completely describes the wave it also has to satisfy the wave equation. Inserting Equation (1.8) into Equation (1.7) leads to the so called Helmholtz equation

$$\nabla^2 U + n^2 k_0^2 U = 0. \quad (1.10)$$

1.1.3 Solutions of the wave equation

Complex wave functions whose amplitudes $U(\vec{r})$ satisfy the Helmholtz equation also satisfy the general wave equation. So the Helmholtz equation can also be used to look for possible wave functions.

Plane waves

The most simple solution of Equation (1.10) is a plane wave. The plane wave is defined as

$$U(\vec{r}) = A e^{-i\vec{k}\cdot\vec{r}} \quad \text{with } \vec{k} = (k_x, k_y, k_z). \quad (1.11)$$

The surfaces of constant phase are called wavefronts. The influence of the wavefronts on the properties of the wave is discussed in detail in Chapter 2. For plane waves the surfaces of constant phase are, as the name suggests, planes.

As mentioned above, arbitrary waves can be described as a superposition of waves. Harmonic plane waves are often used as fundamental waves for the superposition. This helps describe an arbitrary wave or the influence of linear optical systems on the wave. Due to its simplicity, many interesting effects can be easily found and understood. This field is called Fourier optics and is widely used [2].

Spherical waves

Another simple solution of Equation (1.10) is the spherical wave. It is given by

$$U(\vec{r}) = \frac{A_0}{r} e^{-ikr} \quad (1.12)$$

For spherical waves the wavefronts are concentric spheres which propagate with the phase velocity c .

Spherical waves are often used to study the diffraction properties of waves. For this the Huygens principle is used which states that all points of an arbitrary wavefront are the source of a new elemental spherical wave. The superposition of the spherical waves leads to a new wavefront. With this principle it is quite simple to calculate the diffraction of an incoming wave by a general aperture [1, 3].

Paraxial waves

A different class of solutions of the Helmholtz equation (1.10) are paraxial waves. In the simple model of Gaussian optics [1, 2] only special rays of light are used. These rays are called paraxial rays because they obey the paraxial approximation.

The paraxial approximation is valid for rays which form a small angle to the optical axis of the system, and lie close to the axis throughout the system [4]. Therefore, the small-angle approximations are valid.

In beam optics the solutions of the Helmholtz equation where the wavefront normals can be treated as paraxial rays are called paraxial waves. A general approach to

describe paraxial waves can be written as

$$U(\vec{r}) = A(\vec{r}) e^{-ikz}. \quad (1.13)$$

Here the plane wave e^{-ikz} is modulated by a complex amplitude $A(\vec{r})$. This complex amplitude has to fulfill certain boundary conditions so that $U(\vec{r})$ is a paraxial wave.

These boundary conditions are given by the fact that the wave should keep the character of a plane wave. This means that the wave should still propagate mainly in the direction of \vec{k} . To achieve this, the complex amplitude must vary only slowly with z . This assumption leads to the *slowly varying envelope approximation* or short SVEA. As a result, in differential equations the highest-order derivatives may be neglected. For the complex amplitude $A(\vec{r})$ the SVEA can be written as

$$\left| \frac{\partial A}{\partial z} \right| \ll kA, \quad (1.14a)$$

$$\left| \frac{\partial^2 A}{\partial z^2} \right| \ll k^2 A. \quad (1.14b)$$

In order to solve the wave equation using paraxial rays, substituting Equation (1.13) into Equation (1.10) and neglecting the highest-order derivatives according to Equation (1.14), leads to

$$\nabla_t^2 A - i2k \frac{\partial A}{\partial z} = 0 \text{ with the transversal } \nabla_t^2 = \frac{\partial^2}{\partial x^2} + \frac{\partial^2}{\partial y^2}. \quad (1.15)$$

This equation is called the paraxial Helmholtz equation. It is the approximation of the Helmholtz equation (1.10) under the boundary conditions given by the slowly varying envelope approximation.

The simplest solution of Equation (1.15) is the paraboloidal wave, which is also called the Fresnel approximation of the spherical wave. The paraboloidal wave is given by

$$U(\vec{r}) = \frac{A_0}{z} e^{-ikz} e^{-ik \frac{x^2+y^2}{2z}}. \quad (1.16)$$

The use of the paraboloidal wave as approximation for the spherical wave is only valid for $(x^2 + y^2)^2 \ll 4z^3\lambda$.

The most interesting and commonly used solution however is the Gaussian beam

$$U(\vec{r}) = \frac{A_1}{q(z)} e^{-ikz} e^{-ik \frac{x^2+y^2}{2q(z)}}. \quad (1.17)$$

The complex quantity $q(z) = z + iz_R$ is called Gaussian beam parameter or just q-parameter. The characteristic length z_R is called Rayleigh length.

The Gaussian beam can be derived from the paraboloidal wave [2], but has completely different properties. Because of the importance of Gaussian beams for optics its are discussed in the following.

1.2 Gaussian beam optics

A Gaussian beam, as described by Equation (1.17), is a paraxial wave which propagates in z -direction. Its complex amplitude $A(\vec{r})$ only varies slowly with z and solves the paraxial Helmholtz equation (1.15).

In order to fully characterize a plane wave or spherical wave with a given wavelength λ , only the (complex) amplitude and a second parameter are needed, which is the propagation direction for a plane wave and the point of origin of the source for the spherical wave. For Gaussian beams, however, the amplitude and two parameters are needed. In the following, beam parameters which characterize Gaussian beams are discussed.

1.2.1 Beam parameters

As seen in Equation (1.17), a Gaussian beam is fully described by its amplitude, its wavelength and propagation direction, i.e., the wave vector \vec{k} , and the Gaussian beam parameter q .

The Gaussian beam parameter is a complex quantity and therefore has two components. As such, a combination of two linked, real and physical parameters characterize the Gaussian beam. The Gaussian beam parameter can be written in two ways. These are

$$q(z) = z + i z_R, \quad (1.18)$$

and

$$\frac{1}{q(z)} = \frac{1}{R(z)} - i \frac{\lambda}{\pi W^2(z)}. \quad (1.19)$$

Equation (1.19) describes the beam in terms of beam width $W(z)$ and radius of curvature $R(z)$ of the wavefronts. The location where the beam width is minimal is called beam waist. For freely propagating beams only one beam waist exists. Equation (1.18), which describes the same beam as Equation (1.19), contains information about the distance from the beam waist ($\Re\{q\} = z$) and the focus length ($2\Im\{q\} = 2z_R$) of the beam.

As these two sets are interpretations of the same beam, the parameters used to describe the beam are connected. The beam width at a distance z from the beam waist for a given Rayleigh length z_R can be written as

$$W(z) = W_0 \sqrt{1 + \left(\frac{z}{z_R}\right)^2} \quad (1.20)$$

with the waist size

$$W_0 = \sqrt{\frac{\lambda z_R}{\pi}}. \quad (1.21)$$

The radius of curvature of the wavefront for the same beam is given by

$$R(z) = z \left(1 + \left(\frac{z_R}{z} \right)^2 \right). \quad (1.22)$$

The beam width and the wavefront curvature near a beam waist are shown in Figure 1.1. At the position of the beam waist ($z = 0$) the beam diameter ($d = 2W_0$) is minimal and the beam looks like a plane wave, i.e., the radius of curvature $R(0) \rightarrow \infty$. At $z = z_R$ the beam width is increased by a factor of $\sqrt{2}$ and the radius of curvature is minimal.

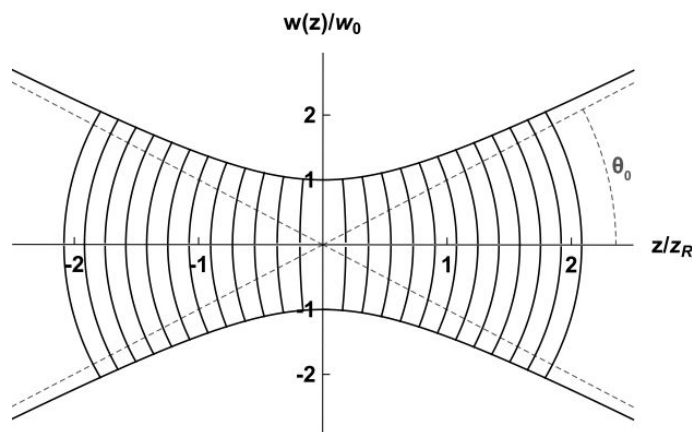


Figure 1.1: A Gaussian beam with width w_0 , beam divergence θ_0 and Rayleigh range z_R . Additionally the wavefronts are shown. At $z = 0$, the beam width is minimal ($W(0) = w_0$) and the wavefront is that of a plane wave, i.e., the radius of curvature is infinite ($R(0) \rightarrow \infty$). At $z = z_R$ the beam width has increased to $W(z_R) = \sqrt{2}w_0$ and the radius of curvature $R(z_R)$ is minimal.

When looking at the beam width of a Gaussian beam in the far field, i.e., $z \gg z_R$, the beam divergence is given by

$$\theta_0 = \frac{W(z)}{z} \approx \frac{W_0}{z_R} = \frac{\lambda}{\pi W_0}. \quad (1.23)$$

This equation is the result of neglecting the first part in Equation (1.20) combined with the use of small-angle approximations.

When comparing a Gaussian beam with a spherical wave in the far field they look almost identical. The phase of the Gaussian beam, however, is delayed by $\frac{\pi}{2}$. This

phase delay is called the Guoy phase which can be written as

$$\zeta(z) = \arctan\left(\frac{z}{z_R}\right). \quad (1.24)$$

Due to this fact, the phase of a Gaussian beam is shifted by an amount of π when coming from the far field and going through a beam waist to the far field again. The physical origin of the Gouy phase shift is the uncertainty principle [5].

1.2.2 Beam propagation

In classical ray optics it is possible to describe a beam as a vector and the influence of optical components as matrices. For propagation, reflection and diffraction the matrices can be given [2, 3]. As any linear system can be seen as a combination of these effects, the complete system can be described by a ray transfer matrix. This matrix is typically written in the form of

$$T = \begin{pmatrix} A & B \\ C & D \end{pmatrix} \quad (1.25)$$

and is also called ABCD matrix.

The matrix formalism developed for ray optics is also suitable for Gaussian beams. All rules which apply to the ray transfer matrices in ray optics are also valid for Gaussian beams. A system described by a ray transfer matrix has an input plane perpendicular to the optical axis of the system and an output plane which is also perpendicular to the optical axis. A Gaussian beam with a q-parameter q_1 at the input is projected onto the output by the ray transfer matrix. At the output the q-parameter q_2 is given by

$$q_2 = \frac{Aq_1 + B}{Cq_1 + D}. \quad (1.26)$$

Here A , B , C and D are the components of the ray transfer matrix as mentioned in Equation (1.25).

The whole matrix formalism is very useful when dealing with laser propagation or resonator design [2, 3].

1.3 Real laser beams

When using real lasers, the beam profile and beam properties of the laser are typically not perfect. The Gaussian beam described by Equation (1.17) is just one special solution of the paraxial Helmholtz equation. In fact it is only the lowest order of a whole class of solutions and is only valid for a beam with a Gaussian intensity distribution. For other intensity distributions other solutions of the paraxial

Helmholtz equation are needed. Various other sets of solutions exist, which can be used to model a real laser beam.

A complete and orthogonal set can be used to fully describe an arbitrary laser beam as a superposition of solutions from this set. The choice of the set typically depends on the symmetry of the laser beam. Typically used sets are Hermite-Gaussian beams for rectangular symmetries, Laguerre-Gaussian beams for cylindrical symmetries and Ince-Gaussian beams for elliptical symmetries. In daily use Hermite-Gaussian beams are typically used because in laser resonators many components depend on rectangular coordinates, e.g. Brewster windows, thin film polarizers or anti-reflective coatings with different properties for s- and p-polarization.

The description of the Gaussian beam parameter q as given by Equation (1.18) is only valid for the perfect Gaussian beam. Higher-order solutions, also called higher-order Gaussian modes, have different propagation properties. The divergence of the perfect Gaussian mode, for example, is smallest compared to higher-order modes with the same beam waist. Therefore, the relationships given by Equations (1.19)-(1.24) cannot be applied directly to beams containing higher-order Gaussian modes.

1.3.1 The \mathcal{M}^2 concept

In order to solve this problem the \mathcal{M}^2 concept [3, 6] was developed. One of the main problems in formulating this method is the definition of the beam width. For Gaussian beam profiles there are many ways to define its width. Some of the most common definitions are the full-width half-maximum (abbreviated FWHM), the $\frac{1}{e}$ - or $\frac{1}{e^2}$ -width and the diameter containing 86% of the beam energy (called ‘D86’).

For irregular beam profiles, on the other hand, these definitions are problematic. Some beams may have multiple minima and irregular maxima. This leads to very different values of the beam width, depending on the used definition of the width. Another problem is that throughout the course of propagation the beam width is not always strictly monotonically increasing with propagation distance for all width-definitions, as described by Equation (1.20) for Gaussian beams.

One definition, however, behaves correctly and is closest to a universal description of a beam width. This is the variance of the beam based on second-order beam moments [7–9]. The use of second-order beam moments to determine the various beam parameters and its value on characterizing beam propagation is quite extensive. For this reason only a short summary is given here. A more detailed discussion on second-order beam moments for further reading is given in Appendix A.

The variance of the beam profile in x -direction is given by

$$\sigma_x^2 = \frac{\iint (x - \langle x \rangle)^2 I(x, y) dx dy}{\iint I(x, y) dx dy}, \quad (1.27)$$

where $I(x, y)$ is the intensity distribution and $\langle x \rangle$ is the first-order beam moment which gives the center of gravity of the beam. The variance in y -direction can be calculated accordingly.

Along the same lines the beam divergence θ_0 can be calculated from second-order beam moments as beam variance in spatial frequencies [7].

In order to compare an arbitrary beam with a perfect Gaussian beam, the beam parameter product, short BPP, can be used. The beam parameter product relates the near-field properties of the beam to its far-field properties and is given by

$$\text{BPP} = W_0 \theta_0. \quad (1.28)$$

For a Gaussian beam the beam parameter product is minimal and has the value $\text{BPP} = \frac{\lambda}{\pi}$.

From the beam parameter product the more convenient parameter \mathcal{M}^2 , also called beam propagation factor, can be derived. This is done by comparing the beam parameter product of an arbitrary (read: real) laser beam with the beam parameter product of a perfect Gaussian beam. The beam propagation factor is then defined as

$$\mathcal{M}^2 = \frac{\text{BPP of real beam}}{\text{BPP of Gaussian beam}} = \frac{\pi W_{\mathcal{M}^2} \theta_{\mathcal{M}^2}}{\lambda}, \quad (1.29)$$

where $W_{\mathcal{M}^2}$ and $\theta_{\mathcal{M}^2}$ are the near-field and far-field properties of the real beam.

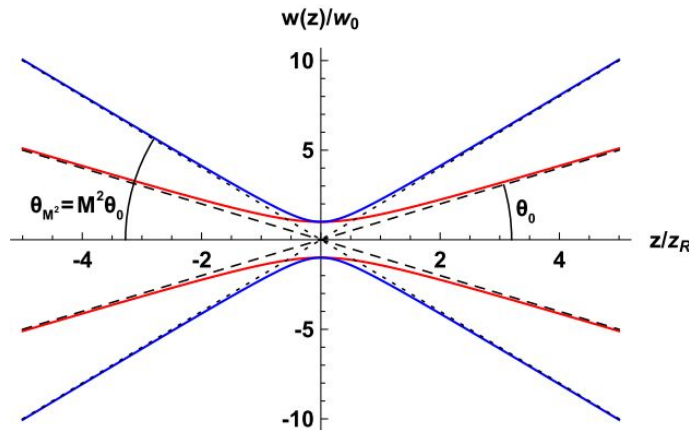


Figure 1.2: Influence of \mathcal{M}^2 on beam width and divergence. A multi-mode beam (blue) with the same beam waist w_0 as a perfect Gaussian beam (red) diverges \mathcal{M}^2 times faster than the Gaussian beam.

As can be seen from Equation (1.29), the real beam diverges \mathcal{M}^2 times faster than a Gaussian beam with the same beam waist. Another interpretation could be that

a real laser beam creates a \mathcal{M}^2 times larger beam waist than a Gaussian beam with the same divergence. Because of this simple relation the \mathcal{M}^2 -parameter is sometimes also called times-diffraction-limit or TDL. This behavior is shown in Figure 1.2.

With the help of the beam propagation factor it is possible to modify the beam parameters of a Gaussian beam given by Equations (1.19)-(1.24). This leads to more general expressions of the equations which are also valid for beams containing higher-order modes.

The beam width given by Equation (1.20), for example, modifies to

$$W(z) = W_0 \sqrt{1 + \left(\mathcal{M}^2 \frac{z}{z_R} \right)^2}. \quad (1.30)$$

It is also possible to define a generalized q -parameter

$$q(z) = z + i \frac{z_R}{\mathcal{M}^2} \quad (1.31)$$

which contains all information of the real laser beam. This way, it is possible to use the ABCD-matrix formalism to calculate the beam propagation of real laser beams [3].

The \mathcal{M}^2 concept as quality indicator?

Sometimes the \mathcal{M}^2 concept is used to characterize the quality of laser beams [10, 11]. Most of the time it is correct to use the \mathcal{M}^2 concept as quality indicator.

When doing so, one has to keep in mind that the \mathcal{M}^2 concept is based on using the beam width and divergence obtained by the second-order moments. As these are only the variance in space and angular-spread, the exact intensity distribution at a certain point of interest along the propagation axis is not available. Thus the term ‘quality’ only refers to the overall propagation characteristics.

For certain applications, however, the peak intensity of a laser is important. In this case it is possible that the peak intensity exceeds the calculated intensity when using the \mathcal{M}^2 parameter. As such, the whole \mathcal{M}^2 concept must be used with caution for these experiments.

A short excursion into creating beams with interesting properties shows that carelessly looking only at the beam profile, either in the near- or far-field, and not taking propagation into account can be dangerous. In the following an example of such a beam is given.

“Non-Gaussian” Gaussian beams

It is possible to create a beam with a nearly perfect Gaussian beam profile which does not contain any contribution from the TEM_{00} mode [6]. These types of beams might be called “non-Gaussian” Gaussian beams. Figure 1.3 shows such a beam with a near-perfect Gaussian beam profile with absolutely no TEM_{00} part.

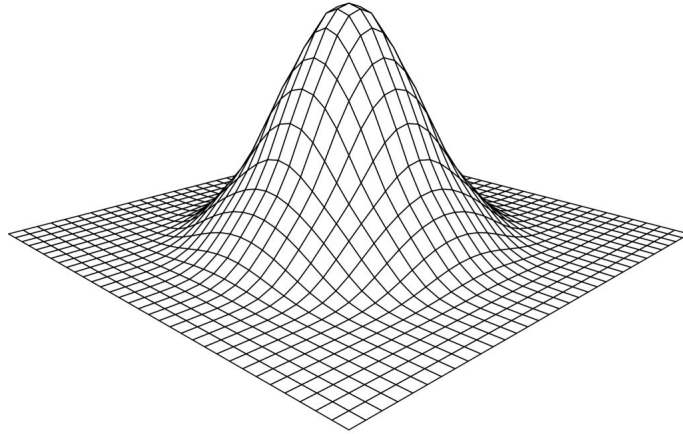


Figure 1.3: A “non-Gaussian” Gaussian beam. The beam profile looks like a perfect Gaussian beam. However, absolutely no contribution of the TEM_{00} mode is present. This example is created by an incoherent superposition of five higher-order Laguerre-Gaussian TEM modes (44% TEM_{01} , 17% TEM_{10} , 19% TEM_{11} , 11% TEM_{20} and 6% TEM_{21}). From [6].

This particular example of a “non-Gaussian” Gaussian beam is created by an incoherent superposition of five higher-order Laguerre-Gaussian TEM modes. It contains 44% TEM_{01} , 17% TEM_{10} , 19% TEM_{11} , 11% TEM_{20} and 6% TEM_{21} . It retains its beam profile during propagation, but it diverges faster than a true Gaussian TEM_{00} beam. This different propagation behavior is characterized by a beam propagation factor of $\mathcal{M}^2 \approx 3.1$.

Chapter 2

Wavefronts – Definition, characterization and measurement

As discussed in Chapter 1 it is possible to use Gaussian beams to describe the propagation of light through media and optical elements. Propagating from a beam waist to the far field, the beam can be described as a plane wave at the beam-waist, as a paraxial wave in the intermediate domain and as a spherical wave in the far field. These three regions of propagation always assume that the beam has a perfect wavefront with specific curvature, as needed by the approximation [2].

In general laser beams used in experiments are not perfect. Usually the beam profile is only near-Gaussian and the wavefront has some distortions [3]. These distortions can originate from the source itself or from aberrations introduced by optical elements used to guide the beam. In this chapter the influence of these distortions on beam propagation and how to characterize them are discussed. A more detailed discussion of aberrations can be found in [1].

2.1 The concept of wavefronts

2.1.1 The wavefront

For coherent radiation the wavefronts are defined as the surfaces of constant phase of the electric field [1, 12]. For ease of use it is convenient to define $\varphi(\vec{r}) = 2\pi m$ with m as an integer number. The wavefront can then be written as

$$w(x, y) = \frac{\lambda}{2\pi} \varphi(x, y). \quad (2.1)$$

For each point of the wavefront the surface normal of the wavefront is parallel to the Poynting vector \vec{S} at that point. This way the wavefront is directly connected to beam propagation as shown in Figure 2.1.

Using geometrical optics one can easily describe how a perfect plane wave is focused by a perfect aberration free lens. In front of the lens the wavefront is plane.

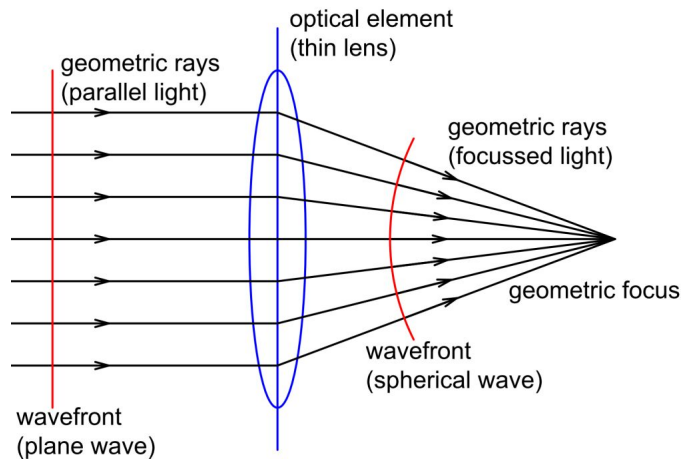


Figure 2.1: A thin lens (blue) alters the wavefront (red) of an incident beam. The geometrical rays (black) are also shown to demonstrate the connection of wave- and ray-optics

After propagation through the lens the beam converges onto a single point, the focus. One can easily see that the perfect lens changes the plane wave to a spherical wave. This change can be described in terms of a modification of the wavefront.

As mentioned before, real laser beams typically do not have perfect wavefronts. The difference between the real wavefront and a perfect wavefront is the wave aberration.

2.1.2 Wavefront aberrations

As mentioned in Chapter 1, in the simple case of Gaussian optics only paraxial rays are considered. While staying in the domain of geometrical optics one can describe the departure of the path of light from the Gaussian optics as geometrical aberrations.

The effect of an aberrated beam is shown in Figure 2.2. An aberration-free focused beam produces an image in the Gaussian image plane. This beam has the Gaussian reference sphere as wavefront, and the point Q_1^* is imaged onto point P_1^* . When comparing the reference beam to an aberrated beam, three aberrations can be defined.

The wave aberration Φ of a wavefront $w(x, y)$ is defined as

$$\Phi = \overrightarrow{Q_1 Q_1^*}. \quad (2.2)$$

The wave aberration measures as to which extent the wavefront $w(x, y)$ differs from the reference wavefront $s(x, y)$.

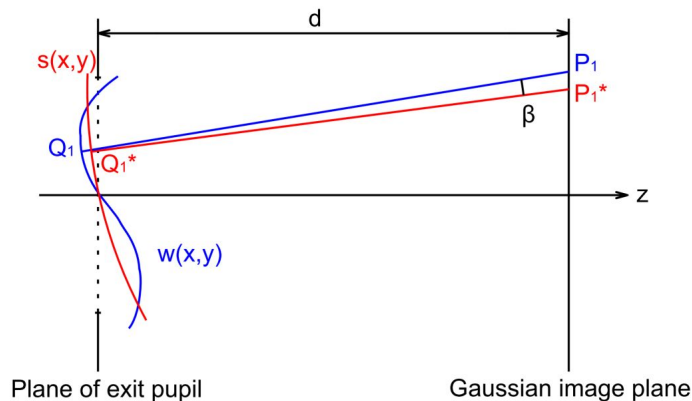


Figure 2.2: Influence of aberrations on beam propagation. The wavefront $w(x, y)$ shows aberrations with respect to the Gaussian sphere of reference $s(x, y)$. The wave aberration $\overrightarrow{Q_1 Q_1^*}$ leads to a ray aberration $\overrightarrow{P_1 P_1^*}$ in the Gaussian image plane [1]. The angle β between the two rays $\overrightarrow{Q_1 P_1}$ and $\overrightarrow{Q_1^* P_1^*}$ is called the angular shift. After [1].

The wave aberration Φ leads directly to a ray aberration δ [13] which is given by

$$\delta = \overrightarrow{P_1 P_1^*}. \quad (2.3)$$

The ray aberration measures how far a spot is shifted in the Gaussian image plane due to the wave aberration.

At last, the ray aberration can also be interpreted as angular shift β when combined with the distance d . The angular shift is defined as the angle

$$\beta = \angle \left(\overrightarrow{Q_1 P_1}, \overrightarrow{Q_1^* P_1^*} \right) \quad (2.4)$$

with β as angle between the aberrated ray and the reference ray.

In order to characterize the wavefront and its aberrations from the Gaussian reference sphere it is convenient to expand the wave aberration Φ or the complete wavefront $w(x, y)$ into modes. Typically, each mode describes an effect of the aberration or wavefront on propagation. An expansion of the complete wavefront leads to

$$w(x, y) = \sum_{k=1}^K c_k P_k. \quad (2.5)$$

To fully describe wavefronts of beams in this modal way one needs a set of basis functions P_k with the coefficients c_k [14]. These functions only need to be linearly independent, but not necessarily orthogonal. For different beam geometries one should use appropriate sets of functions. For rectangular geometries, one can use for

example Legendre, Hermite or Chebyshev polynomials. For circular beams Zernike polynomials usually are used, because they contain the Primary Seidel aberrations [1].

2.2 The Zernike polynomials

As the fundamentals of the Zernike polynomials are quite complex, only the equations needed here are given. For a more complete discussion of the Zernike polynomials see Appendix B.

In order to characterize the wavefront of circular beams it is typically expanded into the real Zernike polynomials. Equation (2.5) gives then

$$w(x, y) = \sum_{k=0}^{\infty} c_k Z_k \quad (2.6)$$

where c_k are the Zernike coefficients and Z_k are the Zernike polynomials with linear numbering shown in Table B.1. By definition (see Appendix B) the Zernike polynomials are functions with two parameters. In polar coordinates they are

$$Z_n^m(\rho, \theta) = \begin{cases} a_n R_n^m(\rho) \cos(m\theta) & \text{for } m \geq 0 \\ a_n R_n^m(\rho) \sin(m\theta) & \text{for } m < 0 \end{cases} \quad (2.7)$$

Here n is the radial order and m the angular dependence. The factors a_n are normalization constants and $R_n^m(\rho)$ are the radial Zernike polynomials which can be written as

$$R_n^m(\rho) = \sum_{s=0}^{\frac{n-m}{2}} (-1)^s \frac{(n-s)!}{s! \left(\frac{n+m}{2} - s\right)! \left(\frac{n-m}{2} - s\right)!} \rho^{(n-2s)}. \quad (2.8)$$

With this representation the normalization is usually chosen as $a_n = 1$ (as opposed to [14]) and results in

$$R_n^m(1) = 1, \quad (2.9)$$

for all possible m and n .

For explicit expressions of the Zernike polynomials in Cartesian coordinates (up to a radial order of $n = 6$) see Table B.1. These Zernike polynomials are typically used to quantify the wavefront aberrations present in experiments from data obtained by a Shack–Hartmann sensor.

2.3 The Shack–Hartmann sensor

The Shack–Hartmann sensor is based on the effects of the wavefront on beam propagation. It is widely used in diverse application areas. In ophthalmology, for example, it is used as a diagnostic tool [15] as well as a calibration tool [16].

With a Shack–Hartmann sensor it is possible to quantify different forms of ametropia. For some forms of refractive eye surgery it is necessary to focus a laser onto an exact spot inside the eye. This can be achieved by quantitative measurements of the aberrations induced by the eye with a Shack–Hartmann sensor. This information is then programmed into the surgical laser which precompensates the aberrations.

2.3.1 The historic Hartmann test

The Shack–Hartmann sensor is based on the principle of the Hartmann test developed 1900 by Johannes Hartmann [17]. The test is very simple and is still used today in astronomy for large telescopes. The basic setup of the Hartmann test is shown in Figure 2.3.

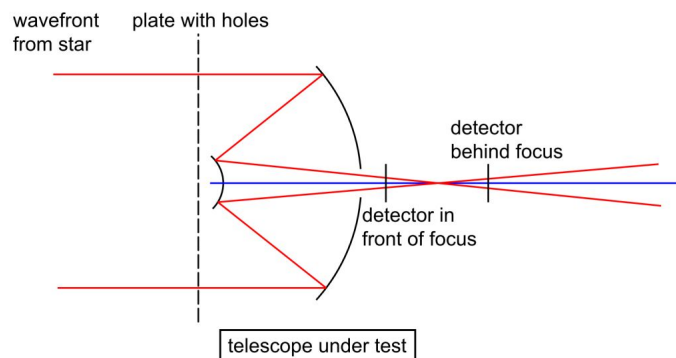


Figure 2.3: Concept of the early Hartmann test as used in astronomy. The incoming light of a star passes an opaque mask with pinholes and gets focused by the telescope. The mask creates individual pencils of rays from the incoming light. The light is imaged at two positions, one in front of the focus and one behind the focus. On the detector each pencil of rays creates a spot. By connecting corresponding spots on the two images the aberrations at the focus can be retrieved.

The Hartmann test setup consists of a large opaque mask with pinholes which is installed in front of the test object. In case of Figure 2.3 the test object is a telescope. The holes in the mask are large enough so that diffraction can be neglected and the mask produces pencils of rays. These rays are then recorded behind and in front of the focus. The detected spot patterns are then evaluated, and optical aberrations can be derived [18].

The big advantage of this setup lies in its simplicity, which is the reason why it is still used today [19]. There are, however, some disadvantages which makes the test not suitable for all situations. First of all, much of the incident light is blocked by the mask. Thus, very sensitive detectors are needed, or else the light source has to be bright enough to measure the aberrations. Second, two images, behind and in front of the focus, are needed. Recording the wavefront and performing the actual measurement simultaneously is not possible. That is why fast fluctuations of the wavefront during the measurement process cannot be detected. This makes the setup only usable in special cases, e.g., for alignment purposes.

In order to improve the detection scheme applying a scanning mechanism to the mask is possible [19]. A more advanced but still quite simple variation of the Hartmann test is the Shack–Hartmann sensor which was developed in the late 1960s by Roland Shack and Ben Platt [16, 20].

2.3.2 Principle of the Shack–Hartmann sensor

The Shack–Hartmann sensor is capable of measuring the wavefront in only one step and needs only little light [16]. This allows insertion of a beam-splitter to use a small fraction of the incoming light for the wavefront detection. In this way the wavefront of the incoming beam and the actual measurement can be recorded at the same time. With adaptive optics it is even possible to correct fluctuations of the wavefront during long measurements.

In order to achieve this, the Shack–Hartmann sensor uses an array of micro-lenses instead of an opaque mask with pinholes. Figure 2.4 shows the basic setup of a Shack–Hartmann sensor.

The micro-lens array divides the incoming beam into many sub-beams. In the following the sub-beams are indexed (i, j) , or short ij . Each sub-beam ij is imaged onto the detector by the micro-lens (focal length f) according to its local wavefront. The detector is placed in the focus of the micro-lenses at distance $L_H = f$ behind the micro-lens array. The detector measures a spot pattern which depends on the distribution of the micro-lenses and the wavefront of the incident beam.

Because the micro-lens array collects all the light from the incident beam, the beam profile can be reconstructed from the intensities of the individual spots. The resolution of beam profile measurement is given by the size and distribution of the micro-lenses [18].

In order to evaluate the wavefront of the incoming beam, the position of each spot is calculated. This is done by calculating the centroid position, i.e., the center of gravity. The centroid position is identical to the first order moment of the spot ij

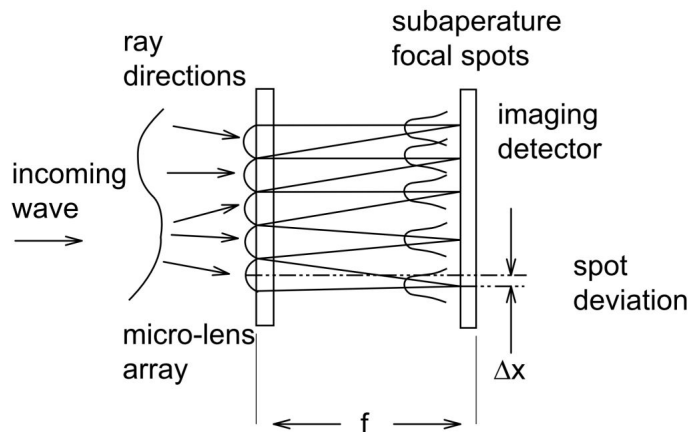


Figure 2.4: Concept of the Shack–Hartmann sensor. The incoming wave is sampled by the micro-lens array. Each micro-lens images a small part of the incoming wave onto the detector, which is placed at focal length f of the micro-lenses. The spot deviation Δx of the spot from the reference position depends on the local wavefront. After [16].

and is calculated according to

$$x_{c,ij} = \langle x_{ij} \rangle = \frac{\iint_{\text{subap},ij} x I(x, y) \, dx dy}{\iint_{\text{subap},ij} I(x, y) \, dx dy}, \quad (2.10a)$$

$$y_{c,ij} = \langle y_{ij} \rangle = \frac{\iint_{\text{subap},ij} y I(x, y) \, dx dy}{\iint_{\text{subap},ij} I(x, y) \, dx dy}. \quad (2.10b)$$

Here the integration is carried out only over that part of the detected image which belongs to the subaperture ij . This is denoted by the integration limits $\iint_{\text{subap},ij}$.

In order to determine the wavefront, the distribution and properties of the micro-lenses are needed. To obtain this information a reference spot pattern created by a beam with a well-known wavefront is recorded. For example for a plane wave the spot pattern directly reproduces the distribution of the micro-lenses and can be used as reference.

The ray aberration mentioned in Section 2.1.2 is given by the shift of the centroid positions of the measured beam compared to the centroid positions of the reference. The local angular shift β_{ij} which represents the local wavefront gradient can be

calculated from the shift of the centroid position by

$$\begin{pmatrix} \partial w / \partial x \\ \partial w / \partial y \end{pmatrix}_{ij} = \begin{pmatrix} \beta_x \\ \beta_y \end{pmatrix}_{ij} = \frac{1}{L_H} \begin{pmatrix} x_c - x_r \\ y_c - y_r \end{pmatrix}_{ij}. \quad (2.11)$$

For a modal analysis of the beam, the wavefront is expanded into polynomials as given by Equation (2.5). In order to reconstruct the wavefront the expansion coefficients c_k are needed. Instead of the local wavefront the local wavefront gradients are calculated here. In order to get the coefficients c_k anyhow the wavefront gradient can be approximated [14] by

$$\frac{\partial w}{\partial x} \Big|_{ij} = \sum_{k=0}^K c_k \frac{\partial P_k(x, y)}{\partial x} \Big|_{ij}, \quad (2.12a)$$

$$\frac{\partial w}{\partial y} \Big|_{ij} = \sum_{k=0}^K c_k \frac{\partial P_k(x, y)}{\partial y} \Big|_{ij}. \quad (2.12b)$$

In order to determine the coefficients c_k , an approach based on the method of the least squares is used [14]. This is done by taking into account the whole beam instead of just one subaperture. This way the wavefront can be reconstructed from a Shack–Hartmann measurement.

In cases where a modal approach to reconstruct the wavefront is not possible, a zonal approach can be used. Here the local wavefront gradients are numerically integrated. A more detailed description of this approach is given by [14, 21, 22].

2.3.3 The Hartmann sensor

In some regions of the electro-magnetic spectrum, especially the XUV range, it is not possible to use conventional lenses. Thus a standard Shack–Hartmann sensor cannot be used. In order to measure the wavefront of such beams the concept of the Shack–Hartmann sensor can be combined with the original approach of the opaque mask of the Hartmann test. This leads to a so called Hartmann sensor which is shown in Figure 2.5.

In principle the Hartmann sensor works just like a Shack–Hartmann sensor, and the same evaluation scheme can be used. There are, however, some fundamental differences, which are due to abandoning the use of micro-lenses, which should be discussed in the following.

First, the distance L_H between the Hartmann mask and the detector is not fundamentally fixed. The placement of the detector with respect to the mask is not important as long as the distance is known for the evaluation of the angular shift β . In practice the length L_H is determined by the detector size, the required resolution

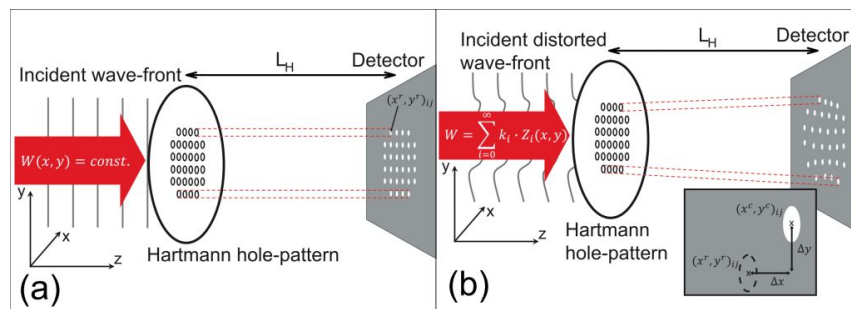


Figure 2.5: The concept of the Hartmann sensor is very similar to the concept of the Shack–Hartmann sensor (compare Figure 2.4). The incoming wave is sampled by the Hartmann hole-pattern. The light which is transmitted through a pinhole hits the detector, which is placed in the distance L_H . a) shows the definition of the reference “image” obtained by a plane wave. b) shows the detector image produced by a distorted wavefront. With the help of the spot deviations Δx and Δy (inset) the wavefront can be reconstructed. From [22].

and the expected aberrations of the beam. The whole scheme can only work if a direct mapping of each spot on the detector to its subaperture is possible. If the distance or the ray aberration is too large the sub-rays will overlap or switch places, e.g., the rays (i, j) and $(i + 1, j)$ are mapped to the apertures $(i + 1, j)$ and (i, j) , respectively.

Second, the pinholes of the Hartmann mask are quite small and diffraction at the pinholes might play a role. For typical XUV wavelengths λ and reasonable pinhole diameters d_s , i.e., within typical manufacturing accuracy, diffraction can be neglected because $d_s \gg \lambda$. For wavelengths other than XUV or for smaller pinholes diffraction must be taken into account.

Third, because of the first two arguments the distribution and spacing of the pinholes must be chosen carefully. In order to avoid overlapping of the spots on the detector the spacing of the pinholes must be large enough. This, along with the diameter of the pinholes, reduces the free aperture of the mask, so the transmission of a Hartmann mask is much lower than the transmission of a micro-lens array which does not block any light. In order to compensate for the low transmission a beam with a high photon number is needed, or else the detector must be sensitive enough to measure the spot pattern even under low light conditions.

Fourth, because the opaque Hartmann mask blocks most of the light, the intensity of the incident beam is only sampled at the locations of the pinholes. Intensity variations in the region between two adjacent pinholes cannot be detected. Therefore, a reconstruction of the beam profile is only partly possible. Calculating the beam parameters for a beam measured with a Hartmann sensor can only be valid for reasonably homogeneous beams. For beams with strong inhomogeneities the

beam profile must be recorded directly in order to calculate the beam parameters.

2.4 The wavefront and beam propagation

In order to fully characterize a beam the beam profile as well as the wavefront must be measured. With this knowledge the beam parameters and the free propagation of the beam can be calculated. With a Shack–Hartmann sensor, it is possible to measure both at the same time. A Shack-Hartmann measurement can therefore be used to completely determine the parameters of a beam [23] and to calculate its propagation properties [24].

2.4.1 Determination of beam parameters

As discussed in Section 1.3 for real beams, beam parameters corresponding to Gaussian beam optics can be defined. These parameters are determined by beam propagation. Because both the beam profile and wavefront are known from a Shack–Hartmann measurement, the beam parameters can be extracted even for general astigmatic beams [9].

The beam parameters are given by the second-order beam moments [8, 9] which are mentioned in Section 1.3 and are discussed in more detail in Appendix A.

The second-order spatial moment determines the beam width at the position of the measurement which, for the spatial coordinate x , is given by

$$2w_x = d_x = 4\sqrt{\langle x^2 \rangle}. \quad (2.13)$$

The beam width in the y -direction can be calculated the same way.

The second-order angular moment is used to determine the divergence of the beam. The divergence is given by

$$\theta_x = 4\sqrt{\langle u_x^2 \rangle}. \quad (2.14)$$

For the beam propagation factor \mathcal{M}^2 mixed second-order moments are needed, which can be calculated as

$$\mathcal{M}_x^2 = \frac{4\pi}{\lambda} \sqrt{\langle x^2 \rangle \langle u_x^2 \rangle - \langle xu_x \rangle^2}. \quad (2.15)$$

By inserting the values for $\mathcal{M}_{x,y}^2$ and divergence $\theta_{x,y}$ into Equation (1.29), it is possible to determine the beam waist w_0 .

2.4.2 Calculation of beam propagation

The beam parameters, beam waist w_0 , beam divergence θ , beam propagation factor \mathcal{M}^2 and beam twist τ can be used to characterize near-Gaussian beams. With the help of the beam profile and the wavefront, however, it is also possible to use Fourier optics [2] in order to calculate the resulting beam at any given position along the propagation axis.

For linear systems it is possible to determine the reaction of the system to arbitrary inputs (e.g., beams) with the help of harmonic analysis and thus calculate the output. For the calculation of the output $g(x, y)$ in response to the input $f(x', y')$ only the impulse response function or the system transfer function is needed. The calculation of $g(x, y)$ is done by

$$g(x, y) = \iint_{\infty} f(x', y') h(x, y, x', y') dx' dy' \quad (2.16)$$

where $h(x, y, x', y')$ is the impulse response function.

The propagation through vacuum is shift-invariant and linear. The shift-invariance means that a shift of the whole system, including the input, by a distance \vec{s} only shifts the output by the same distance. In this case the impulse response function in Equation (2.16) simplifies to

$$h(x, y, x', y') = h(x - x', y - y'). \quad (2.17)$$

Here the impulse response function only depends on the differences $x - x'$ and $y - y'$ and not on the absolute positions x and y .

Combining Equations (2.17) and (2.16) yields the convolution

$$g(x, y) = [h * f](x, y). \quad (2.18)$$

Here the convolution theorem [2] can be used to calculate the output in spatial frequencies

$$G(k_x, k_y) = H(k_x, k_y) F(k_x, k_y). \quad (2.19)$$

The function $F(k_x, k_y)$ is the Fourier transform of $f(x, y)$ and the system transfer function $H(k_x, k_y)$ is the Fourier transform of the general impulse response function $h(x, y)$.

For the propagation of the distance d of a beam through vacuum the Fresnel approximation can be used. The general impulse response function then reads

$$h(x, y) = \left(i \frac{k}{2\pi d} \right) e^{-ikd} e^{-ik \left(\frac{x^2 + y^2}{2d} \right)}. \quad (2.20)$$

The actual calculation of the output of an arbitrary linear optical system can be

accomplished either in real space or in the spatial frequency domain. The choice of system depends on whether the impulse response function or the system transfer function is available or in which system the calculation is easier.

Going back to the initial problem of calculating the intensity at a position z from the Shack–Hartmann measurement at position z_0 , the propagation can be determined using Equations (2.16) and (2.20).

The complex amplitude of the input wave at position z_0 is given by

$$f(x, y) = \sqrt{I(x', y')|_{z_0}} e^{ikw(x, y)|_{z_0}}. \quad (2.21)$$

The intensity $I(x, y)|_z = |g(x, y)|^2$ at position z can be calculated by numerical evaluation [25] of the Fresnel integral

$$I(x, y)|_z \propto \left| \iint_{-\infty}^{\infty} \sqrt{I(x', y')|_{z_0}} e^{ikw(x', y')|_{z_0}} e^{-ik \frac{(x-x')^2 + (y-y')^2}{2(z-z_0)}} dx' dy' \right|^2. \quad (2.22)$$

2.4.3 Evaluating Shack–Hartmann measurements

In order to evaluate Shack–Hartmann measurements with respect to beam parameters and propagation, integrals have to be solved. For actual measurements the detection is typically done by a CCD. As an advantage, the integrals are reduced to sums due to the discrete nature of the detection.

For the evaluation of the wavefront and the determination of the beam parameters only summation over a finite number of pixels and/or subapertures is necessary. This greatly simplifies the evaluation schemes. Implementations of the evaluation can be found in [21–23, 26, 27] and elsewhere.

In a strict mathematical sense the Zernike polynomials are only defined for continuous variables (x, y) . For evaluation purposes, however, it is still possible to quantify wavefront aberrations in terms of Zernike polynomials.

For the calculation of the beam propagation it is convenient to calculate the beam propagation in the spatial frequency domain. With the help of the Fast Fourier Transform (FFT) and the convolution theorem it is possible to reduce the necessary computing power compared to a direct numerical integration in real space considerably.

Chapter 3

Ultra-short laser pulses & nonlinear optics

Optical beams and systems are most often described using linear functions. In order to solve Maxwell's equations, for example, linear approaches are used. These solutions are then used to compose many different fields of use. Another example is the field of Gaussian beam optics and its use of transfer matrices which is based on the linear response of optical components. Another field which uses linear systems to describe different effects is the field of Fourier optics. One of these effects is described in Chapter 2 where it is used to calculate the evolution of a beam along its propagation axis.

In cases where the response of a system is no longer linear, many different effects can occur. Some of these effects are easily understandable while others are quite counterintuitive. Some nonlinear effects can already be observed using (focused) CW lasers. However, because of the nature of these effects, the intensities necessary to observe most of them are quite high.

For an optical beam the intensity of the beam is defined

$$I = \langle \vec{S} \rangle_t \text{ with the units } [I] = 1 \text{ W/cm}^2 \quad (3.1)$$

where $\langle \vec{S} \rangle_t$ denotes the average of the Poynting vector \vec{S} of the beam over a certain time interval t . In order to get to high intensities the area of the beam has to be small. The minimal achievable focal spot is determined by the wavelength of the beam used. Therefore, the highest achievable intensity for a CW laser is limited by its power and wavelength. To further increase the intensity, the peak power of the source has to be increased. This can be done by using pulsed sources. For a given (average) power, the peak power of the pulsed source, and thus the peak intensity, is much higher, because the same energy is contained inside a much smaller time interval (the pulse duration). In order to reach very high intensities, ultra-short laser pulses with a pulse duration of a few (to several ten) femtoseconds are used [28].

The properties of ultra-short laser pulses determine which nonlinear effects can be observed. In order to better understand the properties of ultra-short pulses, a short

introduction is given at the beginning of this chapter. Afterwards, some fundamental basics of nonlinear optics are discussed.

3.1 Ultra-Short Laser Pulses

Only a short introduction shall be given here. For a more thorough discussion on ultra-short laser pulses and the arising phenomena see [3, 29].

One way to describe ultra-short laser pulses is to use the time-dependent electric field. For the sake of simplicity, the spatial and polarization properties of the beam are neglected and the time-dependent electric field can be written as the scalar quantity $E(t)$. Because many mathematical calculations used to describe ultra-short laser pulses are greatly simplified when using complex quantities, it is convenient to use complex representations even when the (physically) measured quantities are real. In the following, complex quantities are denoted by a bar, for example \bar{A} .

Starting from the real time-dependent electric field, the spectral properties of the laser pulse can be obtained by using the complex Fourier transform \mathcal{FT} ,

$$\bar{E}(\omega) = \mathcal{FT}\{E(t)\}. \quad (3.2)$$

Here $\bar{E}(\omega)$ is the complex spectrum with the spectral amplitude $|\bar{E}(\omega)|$ and a spectral phase $e^{i\phi(\omega)}$.

The negative frequencies which occur in $\bar{E}(\omega)$ have no physical interpretation and can be neglected. Additionally, a complex time-dependent electric field often simplifies many equations. By taking this into account, one can define a complex field which satisfies both conditions as

$$\bar{E}^+(t) = \frac{1}{2\pi} \int_0^{\infty} \bar{E}(\omega) e^{i\omega t} d\omega. \quad (3.3)$$

This leads to a complex spectral field strength which only contains positive frequencies. It is given by

$$\bar{E}^+(\omega) = \begin{cases} \bar{E}(\omega) & \text{for } \omega \geq 0 \\ 0 & \text{for } \omega < 0 \end{cases} \quad (3.4)$$

where $\bar{E}(\omega)$ is given by Equation (3.2). The complex spectral field strength contains all information to fully describe the physical electric field.

In order to retrieve the real time-dependent electric field from the complex representations,

$$E(t) = \bar{E}^+(t) + \bar{E}^-(t) \quad (3.5)$$

can be used. Here $\bar{E}^-(t)$ can be calculated, along the same way as $\bar{E}^+(t)$, by using only negative frequencies. This can be further simplified by the identity

$$\bar{E}(\omega) = \bar{E}^*(-\omega). \quad (3.6)$$

As mentioned above, $\bar{E}^+(t)$ contains all information about the electric field. In order to describe an ultra-short laser pulse it is convenient to expand $\bar{E}^+(t)$ into

$$\bar{E}^+(t) = \frac{1}{2} \mathcal{E}(t) e^{i\varphi_0} e^{i\varphi(t)} e^{i\omega_0 t} = \frac{1}{2} \bar{\mathcal{E}}(t) e^{i\omega_0 t}. \quad (3.7)$$

Here $\bar{\mathcal{E}}(t)$ is the complex field envelope. The envelope of the real field is given by $\mathcal{E}(t)$. The parameter ω_0 is the mean frequency, also called carrier frequency, of the pulse and $\varphi(t)$ is the time-dependent phase. The constant phase φ_0 (called carrier-envelope-phase, short CEP) is only important in case of few-cycle pulses [30–32] and can be neglected most of the time.

Description of the pulse by a mean frequency ω_0 is only feasible if the spectral width $\Delta\omega$ of the whole pulse is small compared to the mean frequency ω_0 . As can be seen directly from Equation (3.7), the instantaneous frequency at a given time t can be obtained from the mean frequency ω_0 and the time-dependent phase $\varphi(t)$. It is given by

$$\omega(t) = \omega_0 + \frac{d\varphi(t)}{dt}. \quad (3.8)$$

As can be seen from Equation (3.8), the actual instantaneous frequency depends on the variation of the time-dependent phase. A linear time-dependence, for example, only leads to a constant shift in the mean frequency, whereas a quadratic time-dependence leads to a linear variation of the instantaneous frequency with time. This linear variation is called linear chirp, because in acoustics a linear variation of the frequency sounds like the chirping of a bird. In optics, a linear chirp leads to a pulse which has a different “color” at different points in time. In case of higher-order variations of the time-dependent phase, the pulse shape and color-distribution gets more complex. A more complete discussion of this can be found in [2, 29].

As mentioned above, a pulse with a linear chirp or higher-order phase variations shows a variation of the spectral distribution during the pulse duration. Because, as introduced by Equation (3.2), the time domain and the spectral domain are connected by a Fourier transform, the pulse duration and the spectral width are linked. Furthermore, it can be shown [29], that for a given bandwidth $\Delta\omega$ the shortest pulse (pulse duration τ_p) occurs when no chirp is present. These pulses are then called bandwidth limited. Here the pulse duration τ_p is defined as the full width at half of the maximum (FWHM) of the intensity distribution $|\bar{\mathcal{E}}(t)|^2$. Along the same lines, the spectral width $\Delta\omega$ is defined as the full width at half of the maximum (FWHM) of the spectral intensity $|\bar{\mathcal{E}}(\omega)|^2$.

When using the above definitions, the pulse duration τ_p and the spectral width $\Delta\omega$ are connected by the time-bandwidth product

$$\tau_p \Delta\omega \geq 2\pi c_b, \quad (3.9)$$

where c_b is a constant of the order of 1. The exact value of c_b depends on the pulse profile. For a pulse with a Gaussian time-dependence, for example, the value is $c_b = 0.441$. For other pulse shapes such as sech^2 or Lorentz profiles see Table 1.1 in [29]. The equality holds true if the pulses are unchirped. Such pulses are then called bandwidth-limited.

3.2 Basics of Nonlinear Optics

As mentioned in the introduction of this chapter, very short pulses are used to achieve high intensities. These short pulse durations can be achieved when using bandwidth limited pulses with a broad spectrum. With the help of such pulses it is possible to explore the field of nonlinear optics. Here only a short introduction, necessary for this work, is given. For further discussion see [2, 29, 33, 34].

Inside a medium an electric field E leads to a polarization P . This polarization acts as an additional source and modifies the resulting electric field. Thus the propagation of a wave inside a medium (described by its electric field) is given by the general wave equation

$$\nabla^2 E - \frac{1}{c_0^2} \frac{\partial^2 E}{\partial t^2} = \mu_0 \frac{\partial^2 P}{\partial t^2}. \quad (3.10)$$

In case of a linear medium the polarization depends linearly on the electric field E and can be written as $P = \epsilon_0 \chi^{(1)} E$. Here $\chi^{(1)}$ is the linear susceptibility, which is often written just as χ . When dealing with very low intensities this description is adequate. In the case of ultra-short laser pulses, the intensities often reach a regime where nonlinear contributions cannot be neglected. In this case the polarization must be written as

$$P = P_L + P_{NL} = \epsilon_0 \chi^{(1)} E + P_{NL}, \quad (3.11)$$

with the nonlinear polarization P_{NL} .

For easier treatment, the nonlinear polarization can be expanded into a power series. Thus, P_{NL} can be written as

$$P_{NL} = \epsilon_0 \chi^{(2)} E^2 + \epsilon_0 \chi^{(3)} E^3 + \epsilon_0 \chi^{(4)} E^4 + \dots, \quad (3.12)$$

with $\chi^{(n)}$ being the nonlinear optical susceptibility of n th order. Note, that this is the notation used in [29]. It differs slightly from the notation used in [2, 33, 34].

In general, nonlinear effects require an appropriate medium. The speed of light inside a medium is discussed in Section 1.1.2. It is given by Equation (1.4) as

$$c = \frac{c_0}{n}. \quad (3.13)$$

The speed of light in vacuum can also be written as

$$c_0 = \frac{1}{\sqrt{\epsilon_0 \mu_0}}, \quad (3.14)$$

and the index of refraction relates to the susceptibility as

$$n = \sqrt{1 + \chi}. \quad (3.15)$$

Using Equations (3.12)-(3.15), the polarization, given by Equation (3.11), can be inserted into the general wave equation, given by Equation (3.10). This leads to the nonlinear wave equation

$$\nabla^2 E - \frac{1}{c^2} \frac{\partial^2 E}{\partial t^2} = \mu_0 \frac{\partial^2 P_{\text{NL}}}{\partial t^2}. \quad (3.16)$$

The nonlinear wave equation (3.16) cannot easily be solved directly. To obtain solutions, an iterative approach is typically used. Generally, the nonlinear parts of the polarization are much smaller than the linear part. Consequently, only the linear part of the polarization is used to calculate the initial electric field. In a second step, the initial electric field is used to calculate the nonlinear parts of the polarization. This approach is in fact the Born approximation [2, 34], known from scattering theory.

With the help of the Born approximation it is possible to calculate many different nonlinear effects. As a full description of all nonlinear effects is beyond the scope of this work, only the effects which are important for this work are discussed. For a more complete discussion of the effects see [2, 29, 34] and others.

3.2.1 Kerr effect

One nonlinear effect which should be discussed here is the Kerr effect. It can be shown [2] that in media where a contribution of the $\chi^{(3)}$ is present, the index of refraction linearly depends on the intensity and thus can be written as

$$n = n_0 + n_2 I. \quad (3.17)$$

Here n_0 is the linear index of refraction and n_2 is the second order nonlinear index of refraction. It is given by

$$n_2 = \frac{3\eta}{\epsilon_0 n_0} \chi^{(3)}, \quad (3.18)$$

where η is the wave impedance and n_0 is the linear index of refraction of the medium.

The wave impedance given by

$$\eta = \sqrt{\frac{\epsilon}{\mu}}, \quad (3.19)$$

relates the electric field to the magnetic field of a wave inside a medium. It is typically given in units of ohms. For nonmagnetic materials ($\mu = \mu_0$) it can be simplified to

$$\eta = \frac{\eta_0}{n}, \quad (3.20)$$

where n is the index of refraction of the medium and η_0 the impedance of free space. The impedance of free space is a constant given by

$$\eta_0 = \sqrt{\frac{\mu_0}{\epsilon_0}} \approx 120\pi \Omega. \quad (3.21)$$

Together with a spatial or temporal variation of the intensity, the Kerr effect can lead to interesting nonlinear effects [2]. Two of these effects, the self-phase modulation (SPM) and the self-focusing play a major role in filamentation and are discussed in more detail in Chapter 4.

Chapter 4

Filamentation of ultra-short laser pulses

For certain experiments with pulsed laser sources it is necessary to achieve very high intensities. An intensity increase can either be achieved by increasing the pulse power or by decreasing the beam size. Decreasing the beam size, however, is limited. The achievable beam size is often limited by experimental boundaries and has an absolute minimum at the diffraction limit. Thus, increasing the beam power is sometimes the only option to increase the intensity. For a given laser system it is not easily possible to increase the pulse energy beyond a certain point. In order to achieve higher intensities the pulse duration has to be reduced.

In Section 3.1 it is described how the pulse duration and the spectral bandwidth of a laser pulse are linked. In order to achieve a temporal compression of the laser pulse, an initially bandwidth-limited pulse has to be spectrally broadened. This can be achieved by using the effect of self-phase modulation. For efficient and homogeneous spectral broadening via self-phase modulation, the laser beam has to be small over a long distance. In order to achieve this, the laser beam has to be guided.

This guiding can happen inside a so-called filament [35], where the beam is trapped over a distance significantly longer than its Rayleigh length. The effect of beam-trapping is described in [29, 36]. In this chapter only the effects leading to the major contributions to filamentation are described. For full reviews on the properties of filamentation see [37, 38].

4.1 Fundamentals of filamentation

4.1.1 Self-phase modulation

As mentioned in Section 3.2.1 the Kerr effect, as a time-dependent third-order non-linearity, can lead to the so called self-phase modulation. However, higher-order nonlinearities can also contribute to self-phase modulation. For the intensities present

during the experiments described in this work, these higher-order contributions are small compared to the Kerr-effect and are therefore neglected.

An ultra-short laser pulse can be described as a time-dependent electric field (see Section 3.1). Together with the intensity-dependent index of refraction, introduced by the Kerr effect, this leads to an index of refraction which is time-dependent.

When a laser pulse propagates through an optical medium of length L the phase after the propagation [2] is given by

$$\varphi = -n k_0 L. \quad (4.1)$$

Due to the Kerr effect the phase $\varphi(t)$ is now time-dependent. In Section 3.1 it is explained that the instantaneous frequency of a laser pulse is given by its time-dependent phase. Using Equations (3.8), (3.17) and (4.1) together with a time-dependent intensity $I(t)$ the instantaneous frequency can be written as

$$\omega(t) = \omega_0 - n_2 \frac{dI(t)}{dt} k_0 L. \quad (4.2)$$

Here ω_0 is the carrier frequency of the pulse, k_0 the wave vector of the pulse and L the length of the nonlinear medium with the nonlinear index of refraction n_2 .

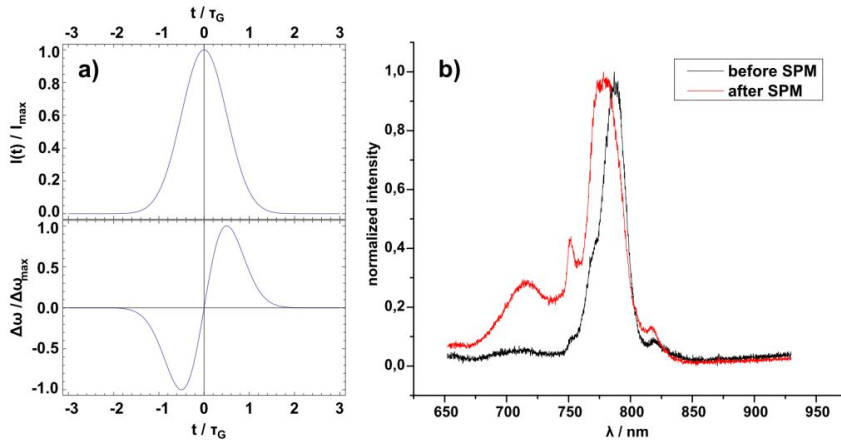


Figure 4.1: The effect of self-phase modulation. a) Intensity profile and corresponding frequency shift. b) Experimental spectrum of a laser pulse before (black) and after (red) self-phase modulation in a filament.

As can be seen from Equation (4.2) the frequency decreases, corresponding to a blue-shift, during an increase of the intensity. At a later time, the frequency increases, i.e., gets red-shifted, due to an intensity decrease. This means that for a given laser pulse, the pulse front, or leading edge, gets blue-shifted, whereas the pulse back, or trailing edge of the pulse, gets red-shifted. If the laser pulse is initially bandwidth-limited, no spectral chirp is present. For such pulses, it can be easily understood

that self-phase modulation leads to the generation of new frequency components during the course of the pulse.

New frequency components are continuously generated along the propagation through the nonlinear medium. Thus they can interfere with corresponding frequencies already present in the pulse or with frequencies generated at later or earlier times. Due to this interference, the exact shape of the spectrum at the end of the self-phase modulation strongly depends on the propagation properties of the beam inside the medium.

In Figure 4.1 the effect of self-phase modulation is shown. A laser pulse with a Gaussian pulse shape leads to the time-dependent frequency shift $\Delta\omega(t)$ shown in Figure 4.1a). Additionally, the spectrum of a laser pulse before and after undergoing self-phase modulation inside a filament is shown in Figure 4.1b). When comparing the spectrum of the pulse before and after the filament, the spectral broadening due to the generation of new frequencies during self-phase modulation can be seen. Additionally a blue-shift of the main part of the beam is visible. This blue-shift is caused mainly by the weak plasma which is present inside the filament.

As has been shown in this section, it is possible to use self-phase modulation to spectrally broaden an existing laser pulse. That way it is possible to further shorten the laser pulse.

4.1.2 Self-focusing

Another consequence of the Kerr effect is self-focusing, and as such it is closely related to self-phase modulation. Self-phase modulation is based on a time-dependent variation of intensity, whereas self-focusing is caused by a spatial variation of intensity. As for self-phase modulation, the contributions of higher-order nonlinearities are neglected here. For a more detailed discussion of self-focusing see [29, 37, 38].

From Section 3.2.1, the intensity-dependent change of the refractive index is known to be

$$\Delta n_{\text{Kerr}}(I) = n_2 I. \quad (4.3)$$

Assuming a Gaussian beam profile

$$I(x, y) = I_0 e^{-2\frac{x^2+y^2}{w^2}}, \quad (4.4)$$

it can be easily shown [2] that a thin medium of length L with a nonlinear index of refraction n_2 acts as a lens. Its focal length is approximately

$$f_{\text{sf}} = \frac{w^2}{2 n_2 I_0 L}. \quad (4.5)$$

Here, self-focusing effects which already occur during the propagation through the medium are ignored. Additionally, it is assumed that the intensity varies only spatially and is constant over time.

For a real laser beam, in order to show self-focusing, the always present diffraction has to be overcome. It can be shown that this can happen if the power (not the intensity) of the beam exceeds a certain critical power P_{cr} . In order to calculate the critical power, different models can be used [29]. All these approaches lead to a critical power of the form

$$P_{\text{cr}} = a \frac{\lambda_0^2}{n_0 n_2}, \quad (4.6)$$

where a depends on the model and is of the order of 0.1 [29, 37].

Once the power of the beam exceeds the critical power, the beam collapses to a point after the self-focusing distance z_{sf} . The calculation of propagation through a nonlinear medium is extremely difficult. For the self-focusing distance only a semi-empirical formula, derived from numerical calculations [29, 37], can be found. Starting from a beam waist, a beam with the Rayleigh length z_{R} will collapse at

$$z_{\text{sf}} = \frac{0.183 z_{\text{R}}}{\sqrt{\left(\sqrt{\frac{P}{P_{\text{cr}}}} - 0.852\right)^2 - 0.0219}}. \quad (4.7)$$

4.1.3 Plasma defocusing

Another aspect present in filaments are effects which arise from a plasma [39, 40]. Self-focusing or external focusing leads to an increased intensity of the laser beam. Once the intensity is high enough, a weakly ionized plasma is created. This plasma then gives rise to additional effects which change the index of refraction inside the filament. Here, only a simple model is introduced. For further discussions see [29, 37, 38].

The plasma which is generated by the beam can oscillate resonantly at the so called plasma frequency

$$\omega_{\text{p}} = \sqrt{\frac{e^2 N_{\text{e}}}{\epsilon_0 m_{\text{e}}}}. \quad (4.8)$$

Here, N_{e} denotes the density of the free electrons, e is the unit charge and m_{e} is the electron mass. For frequencies $\omega < \omega_{\text{p}}$ the plasma is opaque. The free electron density at which it becomes opaque for a given frequency ω is called critical density

$$N_{\text{c}}(\omega) = \frac{\epsilon_0 m_{\text{e}} \omega^2}{e^2}. \quad (4.9)$$

Away from resonances or direct transitions of bound electrons into the continuum, the ionization originates from multi-photon processes [29] and N_{e} shows a (nonlinear) intensity-dependence.

The resonance of the plasma also leads to an additional contribution to the index of refraction. This also plays a huge role in the phase-matching of high-order harmonics and is discussed further in Section 5.2.2. The contribution of the plasma to the index of refraction is given by

$$n = \sqrt{1 - \left(\frac{\omega_p}{\omega}\right)^2} = \sqrt{1 - \left(\frac{N_e}{N_c(\omega)}\right)}. \quad (4.10)$$

For weakly ionized plasmas ($N_e \ll N_c$), as they occur inside a filament, the change of the index of refraction of the medium simplifies to

$$\Delta n_{\text{plasma}}(I) = -\frac{N_e(I)}{N_c} \quad (4.11)$$

As one can see, the change of the refractive index is negative. In Section 4.1.2 it is described that an intensity-dependent change of index of refraction acts like a lens. In case of the Kerr effect, it produces a positive contribution to the index of refraction and leads to a focusing effect. For the laser-induced plasma, the contribution is negative and it can be shown that this leads to an additional defocusing of a beam.

4.2 Filamentation of ultra-short laser pulses

During the interaction between a strong laser pulse and a nonlinear medium, many effects can occur. Above, two processes which influence the spatial properties of a laser beam are described. In Figure 4.2 these effects are visualized. On the left,

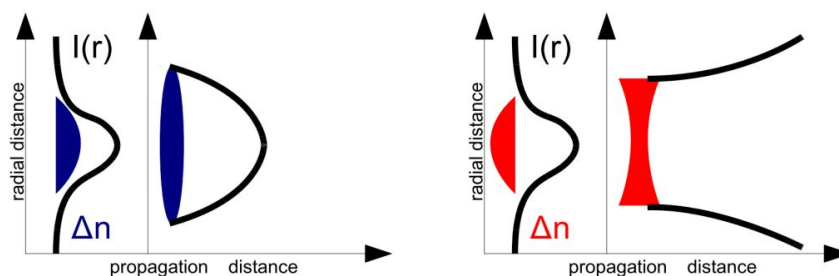


Figure 4.2: The effects which lead to filamentation are visualized here. The Kerr effect (left) causes an intensity-dependent change of the index of refraction. For higher intensities, the index of refraction increases. This leads to self-focusing of the beam. The plasma (right) which is generated by the laser shows the opposite effect. For higher intensities, the index of refraction decreases. This acts like a defocusing lens, causing the beam to diverge. From [38].

the impact of the Kerr effect is shown. It leads to the self-focusing of the beam, as

described in Section 4.1.2. On the right, the influence of the plasma on the beam is shown. In Section 4.1.3 it is discussed that the plasma causes additional diffraction which leads to a defocusing effect.

It is evident that these effects compete with each other. Under certain circumstances it might happen that the strength of both effects alternates. At the beginning the beam begins to collapse, due to self-focusing. This leads to an increased plasma, which causes the beam to diverge. The plasma is reduced again, until the self-focusing dominates once more. When this alternation happens over a long distance, the beam becomes trapped and travels nearly diffraction free. This effect is called filamentation.

The processes mentioned here only take the spatial intensity distribution into account. When dealing with the filamentation of ultra-short laser pulses, the time-dependent intensity variation cannot be neglected. As a result, time-dependent effects are always present inside a filament created by ultra-short laser pulses. In the case of self-phase modulation this is a highly desirable effect, as described in Section 4.1.1. Additionally, some simplifications were made throughout this chapter. For many of the aspects described here, other spatial and time-dependent effects, e.g., the presence of a background reservoir surrounding the filament [41–43], also play a role. This leads to the fact that the filamentation of ultra-short laser pulses is a highly complex process [37, 38, 44–48].

Inside a filament the beam has a small beam diameter and is trapped over a long distance. Thus, the length over which the intensity is high enough for a nonlinear interaction is long. As mentioned at the beginning of this chapter this is a necessary condition for efficient and homogeneous self-phase modulation. A filament provides this without the need of external guiding, e.g., by a hollow-core fiber as it is used in [49]. Thus it is a well suited tool to achieve spectral broadening.

Chapter 5

High-order harmonic generation

The generation of high-order harmonic radiation of an ultra-short laser pulse is one of the most discussed nonlinear effects. It was first seen experimentally 1977 by Burnett et al. [50] using a 2 ns CO₂ laser on solid Al targets. Further studies into the field of high-order harmonics were conducted in the 1980s [51–53]. In these studies the plateau region typical for high-order harmonic generation was already discovered. In Figure 5.1 the typical regimes encountered in high-order harmonic

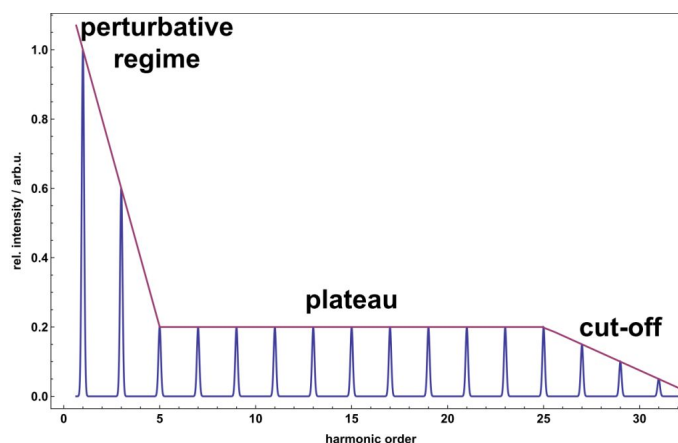


Figure 5.1: The different regimes of high-order harmonic generation. The steep decline in the perturbative regime can be explained by perturbation theory. In the plateau regime intensity of the harmonic lines is nearly constant. In the cut-off region the intensity decreases again.

generation are shown. The step decline in the perturbative regime can be explained by perturbation theory. In the following plateau regime the intensity of the harmonic lines is nearly constant, whereas in the cut-off region the intensity decreases again. However, at the time of its findings the occurrence of the high-order harmonics or the plateau could not be explained.

Later, in 1993, a theoretical model was found by Corkum [54] and Kulander et al. [55] which describes the spectral properties very well. The model used a semi-classical approach which splits the process of high-order harmonic generation into three individual steps. Therefore, the model is often called three-step-model. A fully

quantum-mechanical description [56] was found in 1994 which confirmed many of the assumptions made in the three-step-model. Since then many interesting phenomena and applications have arisen. For example, the field of attosecond physics [57, 58], x-ray microscopy [59, 60], lensless imaging [61] or XUV interferometry [62] to name just a few.

In the following only an introduction to the wide field of high-order harmonic generation can be given. For a more complete discussion see reviews [30, 63]. In order to understand the process of high-order harmonic generation, it is advisable to first examine the response of a single atom to a strong laser field.

5.1 Single Atom Response

A quasi-classical model to describe the process of high-order harmonic generation was developed separately by Corkum [54] and Kulander et al. [55] in 1993. The results of the so-called three-step-model were reproduced shortly after by Lewenstein et al. [56] using a fully quantum-mechanical approach. Later it was extended to elliptically polarized laser fields [64]. It is very interesting to notice that the extremely nonlinear process of high-order harmonic generation can be described with high accuracy by a simple and quasi-classical model.

5.1.1 The Three Step model

The quasi-classical model by Corkum and Kulander is also called three-step-model, because it can be split into three different steps which can be treated separately. These three steps are shown in Figure 5.2.

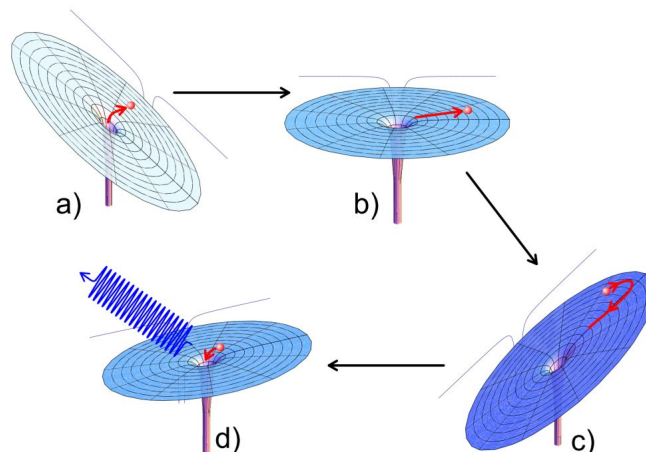


Figure 5.2: The three-step-model. a) Step 1: Ionization. b) and c) Step 2: Quasi-free propagation. d) Step 3: Recombination and photon emission.

The first step is the ionization of an atom, thus creating an electron which can be treated as free in the following. The second step is the classical motion of the electron in the oscillating laser field. During the motion in the laser field the free electron can return to its origin and can recombine with its parent ion, which is the last step. These three steps are discussed separately in the following.

Step 1: Ionization

The ionization comes from the interaction of the electric field of the laser pulse with the atomic potential of the atom.

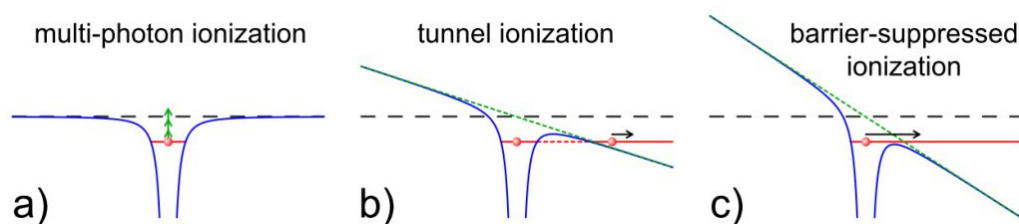


Figure 5.3: The three possible ionization scenarios are (a) multi-photon ionization, (b) tunnel ionization and (c) barrier-suppressed ionization. The black, dashed line marks the vacuum level, the blue line is the effective atomic potential, the red line is the energy level of the bound electron and the green line (arrows in (a)), depicts the influence of the laser field.

In Figure 5.3(a) the disturbance of the atomic potential by the laser field is only weak. Thus, multi-photon ionization is the dominant ionization mechanism. In Figure 5.3(b) the strength of the laser field is of the order of the atomic potential. This way the atomic potential is significantly modified. If the frequency of the oscillation of the laser field is low enough, the created potential wall can be treated as static and for the valence electrons tunnel ionization is possible. In Figure 5.3(c) the laser field is even stronger compared to Figure 5.3(b), and the barrier for the valence electrons is suppressed. This way the electrons are “ripped” from the atom. This scenario is therefore called barrier-suppressed ionization.

The process of tunnel ionization was studied in detail 1965 by Keldysh [65], and many aspects of it can be found in the literature. One significant find was that the oscillations of the laser field must be slow enough to allow significant tunnel ionization [66]. For this the timescale of the laser field oscillation T_{laser} must be longer than the timescale τ_{tunnel} on which tunneling takes place, i.e. $T_{\text{laser}} \gg \tau_{\text{tunnel}}$. If this condition is met, the laser field can be treated as static during the ionization process. For higher frequencies of the laser field, i.e., shorter wavelengths, the tunneling process is less efficient, and consequently high-order harmonic generation is less efficient. Following this line of thought, the most renowned part of Keldysh’s work was the definition of a parameter to determine boundary conditions for tunnel ionization. This parameter is now called Keldysh parameter. It can be given

as

$$\gamma = \sqrt{\frac{I_P}{2U_P}}, \quad (5.1)$$

where I_P is the ionization potential of the material used and U_P is the so called ponderomotive potential or ponderomotive force.

The ponderomotive potential is in fact the average kinetic energy an electron can pick up in an oscillating electric field. It is given by

$$U_P = \overline{E}_{\text{kin}} = \frac{e^2 E_0^2}{4m_e \omega^2}. \quad (5.2)$$

On average an electron in an oscillating field stays more or less at the same place and only performs a quivering motion. Because of this, U_P is sometimes called *quiver energy* of the electron due to the oscillating laser field.

With the help of the Keldysh parameter defined by Equation (5.1) it is possible to distinguish between the domination of multi-photon ionization and tunnel ionization. For $\gamma > 1$ the ionization potential is dominant and the atom is ionized mainly by multi-photon ionization. For $\gamma < 1$ the electric field is strong enough to create a potential barrier for the electrons and tunnel ionization is the dominant ionization pathway. In the range $\gamma \approx 1$ both contributions are of the same order of magnitude and the transition from multi-photon ionization to tunnel ionization can be observed [67].

As high-order harmonic generation is most efficient when tunnel ionization is possible, so called ionization saturation must be considered. When the leading edge of a laser pulse is too long and intense, multi-photon ionization is efficient and all atoms are ionized this way. At the peak intensity, where tunnel ionization would be dominant, no neutral atoms are left and high-order harmonic generation is not possible. To avoid ionization saturation the laser pulses must be short enough so that the rise in intensity at the pulse front is fast and enough neutral atoms are still present during the time of peak intensity.

In order to allow for the treatment of the electron after the ionization process as free electron, the place of “birth” of the electron outside the atom must be away far enough so that the atomic potential is small compared to the accelerating laser field. This limits the intensities to regimes where tunnel ionization is dominant.

Step 2: Propagation

After the electron has left the atom it can be treated as a free particle in an oscillating laser field. This can be done by using a classical approach.

Because tunnel ionization typically happens only when the electric field of the laser pulse is strongest, the electron is accelerated away from its parent ion immediately after it is created. After some time the sign of the electric field changes due to its

oscillation and the electron is slowed down to a stop. After the electron is slowed down the movement direction is reversed and it is accelerated back to its origin where it can recombine with its parent ion.

The amplitude $a_0 = \frac{E_0 e}{m\omega^2}$ of this motion is sometimes referred to as ponderomotive radius. Note that the maximum distance an electron can travel away from its parent ion is $\frac{\lambda}{4}$ for electrons traveling close to the speed of light. This relativistic movement only happens for very high intensities and must be treated differently [28]. The intensities needed for relativistic motion are greater than 10^{16} W/cm² and were not used in the experiments described here. As such, relativistic motion is not within the scope of this work.

Step 3: Recombination

When the electron travels back to its origin it gains kinetic energy from the laser field. Eventually it can recombine with its parent ion. Typically the electron recombines into the ground state and emits its excess energy in form of a photon with the energy

$$\hbar \omega_n = E_{\text{kin}} + I_P. \quad (5.3)$$

When using the classical treatment for the propagation it is possible to calculate the maximum energy an electron can obtain. It can be shown [68] that the kinetic energy depends on the time of “birth” of the electron (expressed as phase ϕ) relative to the maximum of the electric field oscillation. Calculations show that electrons created at a phase $\phi \approx 18^\circ$ obtain the maximum kinetic energy of $3.17U_P$ at the moment of recombination. This leads to a maximum photon energy of

$$\hbar \omega_c = 3.17 U_P + I_P. \quad (5.4)$$

This maximum energy is also called cut-off energy because it can be expected that the high-order harmonic spectrum is cut off at this energy.

Already one year before the invention of the three-step-model the cut-off law was obtained empirically [69]. As such, it is remarkable to note that the simple, classical treatment of the free electron leads to the same cut-off law.

5.1.2 Quantum-mechanical model

Another approach to describe the process of high-order harmonic generation is to use a quantum-mechanical model. As high-order harmonic generation is a nonlinear process, the source of the emitted radiation is the nonlinear dipole oscillation of the system. In order to calculate the nonlinear response of the system, the time-dependent dipole moment of the system in the special case of high-order harmonic radiation has to be obtained.

Derivation of the time-dependent dipole moment

The time-dependent Schrödinger equation in atomic units reads

$$i \frac{\partial}{\partial t} |\psi(\vec{r}, t)\rangle = \left(-\frac{1}{2} \nabla^2 + V(\vec{r}) + \vec{r} \vec{E}(t) \right) |\psi(\vec{r}, t)\rangle. \quad (5.5)$$

As was mentioned, in order to quantum-mechanically analyze high-order harmonic generation, the time-dependent dipole moment is needed. It is obtained by

$$\vec{\mu}(t) = \langle \psi(\vec{r}, t) | \vec{r} | \psi(\vec{r}, t) \rangle. \quad (5.6)$$

From the dipole moment the high-order harmonic spectrum can be obtained by its Fourier transform.

Following Lewenstein et al. [56], some assumptions regarding the process of high-order harmonic generation are made.

1. Only one electron contributes to high-harmonic generation. This is often referred to as “single-active electron approximation”.
2. Contributions to the evolution of the system of other states than the ground state $|0\rangle$ are neglected.
3. Depletion of the ground state does not take place, i.e., $U_P < U_{\text{sat}}$.
4. In the continuum the electron can be treated as a free particle, and the influence of the atomic potential on the evolution is neglected.

Using these assumptions, the time-dependent wave function $|\psi(\vec{r}, t)\rangle$ can be written as

$$|\psi(\vec{r}, t)\rangle = e^{iI_P t} \left(a(t) |0\rangle + \int b(\vec{v}, t) |\vec{v}\rangle d^2\vec{v} \right). \quad (5.7)$$

Here $a(t) \approx 1$ is the ground-state amplitude. The continuum states have the corresponding amplitudes $b(\vec{v}, t)$, where \vec{v} denotes the kinetic momentum.

For convenience, a new parameter

$$\vec{p} = \vec{v} + \vec{A}(t), \quad (5.8)$$

corresponding to a canonical momentum, is introduced. Here $\vec{A}(t)$ is the vector potential of the laser field $\vec{E}(t)$.

Using Equations (5.7) and (5.8), and assuming $a(t) = 1$ in the following, the time-dependent dipole moment is now obtained by

$$\vec{\mu}(t) = i \int_0^t \int \vec{E}(t) \times \vec{d}^* (\vec{p} - \vec{A}(t)) \times e^{-iS(\vec{p}, t, t')} \times \vec{d} (\vec{p} - \vec{A}(t')) d^3\vec{p} dt' + \text{c.c.} \quad (5.9)$$

The parameter $S(\vec{p}, t, t')$ is called quasi-classical action [56]. It represents the phase change an electron experiences as it propagates through vacuum and is therefore also called atomic dipole phase. The quasi-classical action can be calculated as

$$S(\vec{p}, t, t') = \int_{t'}^t \left(\frac{1}{2} (\vec{p} - \vec{A}(t''))^2 + I_P \right) dt''. \quad (5.10)$$

In Equation (5.9) \vec{d} is the dipole matrix element for a bound-free transition and its complex conjugate \vec{d}^* is the dipole matrix element for a free-bound transition. They are expressions for the probability that such a transition happens. They are given by

$$\vec{d}(\vec{v}) = \langle \vec{v} | \vec{r} | 0 \rangle, \quad (5.11a)$$

$$\vec{d}^*(\vec{v}) = \langle 0 | \vec{r} | \vec{v} \rangle. \quad (5.11b)$$

Analysis of the time-dependent dipole moment

With the help of the parameters given by Equations (5.10) and (5.11) it is possible to find a more intuitive interpretation of Equation (5.9). The first part of the equation is the external field which drives the process. The other three parts under the integral can be linked to the three steps found in the quasi-classical three-step model. Each part corresponds to one step.

- $\vec{d}(\vec{p} - \vec{A}(t'))$ – Step 1 – Ionization from ground-state at time t' .
- $e^{-iS(\vec{p}, t, t')}$ – Step 2 – Propagation in laser-field during time $t - t'$.
- $\vec{d}^*(\vec{p} - \vec{A}(t))$ – Step 3 – Recombination into ground state at time t .

In order to examine the properties of the time-dependent dipole moment it is not necessary to calculate the integral for all possible \vec{p} directly. Because the calculation is restricted to high-order harmonic generation it is safe to assume that changes in the dipole matrix elements are dominated by the quasi-classical action [56]. Thus, the major contributions to the integral come from the stationary points of the quasi-classical action. The quasi-classical action, on the other hand, corresponds to the difference of the positions of the electron at the times t and t' . Thus, the stationary points are given by

$$\nabla_{\vec{p}} S(\vec{p}, t, t') = \vec{x}(t) - \vec{x}(t') = 0. \quad (5.12)$$

As such, the stationary points are given by the fact that the electron which was “born” at moment t' returns to its origin at time t . In order to contribute to the high-order harmonic generation, it is necessary that the origin lies close to the parent ion so that recombination can occur.

With the help of the stationary points of the quasi-classical action, it is possible to calculate the dipole moment. As mentioned before, the Fourier transform of the time-dependent dipole moment yields the high-order harmonic spectrum. The spectrum retrieved from the fully quantum-mechanical treatment shows the same behavior as the spectrum created by the quasi-classical three-step model. The

quantum-mechanical spectrum clearly shows a perturbative regime, a plateau region and a cut-off region. By examining the spectrum and its different regions some interesting results can be retrieved.

At first let's take a close look at the plateau region. As mentioned above, the quasi-classical action is the phase change, called atomic dipole phase ϕ_{at} , an electron experiences as it propagates through vacuum. So an electron obtains the atomic dipole phase $\phi_{\text{at}} = S(\vec{p}, t, t')$. For the plateau region it can be shown that a given photon energy contains multiple contributions. It means that electrons with different trajectories (leading to different phases ϕ_{at}) have the same kinetic energy when they recombine. These different trajectories, called quantum paths, interfere to create the high-order harmonic spectrum. With the help of a quasi-classical model it can be shown that, for the plateau region, two different quantum paths contribute to the spectrum.

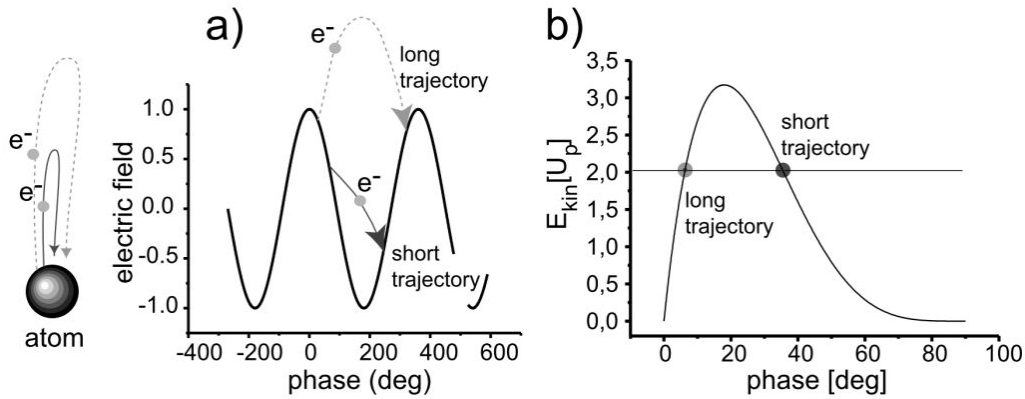


Figure 5.4: Illustration of the two different quantum paths. a) For a given kinetic energy gain one trajectory has the ionization event occur earlier and the recombination event occur later than for the second trajectory. b) The gain of kinetic energy plotted against the ionization time, given in terms of phase of the electric field. The maximum kinetic energy gain of $E_{\text{kin}} \approx 3.17 U_P$ corresponds to ionization events occurring at a phase of the electric field of $\varphi \approx 18^\circ$. From [68].

Figure 5.4 shows these two quantum paths. For a given kinetic energy gain one trajectory has the ionization event occur earlier and the recombination event occur later than for the second trajectory. This is shown in Figure 5.4a). Consequently, the propagation time in the vacuum is significantly longer than for the other trajectory. Because of this, one trajectory is called long quantum path and the other one is called short quantum path. In Figure 5.4b) the gain of kinetic energy is plotted against the ionization time, given in terms of phase of the electric field. For a given kinetic energy the contributions of the two quantum paths are visible. For the maximum kinetic energy gain of $E_{\text{kin}} \approx 3.17 U_P$, corresponding to an ionization event occurring at a phase of the electric field of $\varphi \approx 18^\circ$, only one trajectory exists.

By examining the cut-off region a cut-off law very similar to the one obtained by the three-step model can be found. In fact only a minor correction of the classical cut-off law is needed. The cut-off law found by the full quantum-mechanical treatment is

$$\hbar \omega_c = 3.17 U_P + F\left(\frac{I_P}{U_P}\right) I_P. \quad (5.13)$$

The function $F\left(\frac{I_P}{U_P}\right)$ is the correction term, due to quantum-mechanical effects. Its value is of the order of 1. For a very weak ionization potential ($I_P \ll U_P$) the function has a value of $F(0) = 1.32$. As the variable $\frac{I_P}{U_P}$ rises the function decreases slowly [56]. For example, for $I_P = \frac{1}{3}U_P$ the value of the function is $F(3) = 1.25$.

The shift of the cut-off law compared to the three-step-model can be explained by the approximations used in the quasi-classical treatment. It is assumed that the electron tunnels out of the atomic potential at $x = 0$. As it tunnels out, the electron, in fact, is “born” at a small distance x_0 away from the atom. Due to this, the electron has to travel longer in the laser field until it can recombine at $x = 0$. When this correction is regarded in the quasi-classical model, the same correction factor as for $F(0)$ is obtained. The correct behavior for other values of $\frac{I_P}{U_P}$ is more complex and is discussed extensively in [56].

5.1.3 Spectral properties of high-order harmonic generation

The quite simple quasi-classical three-step-model and the quantum-mechanical treatment show remarkable similarities. Especially the cut-off law fits extremely well to the experimental results [70, 71]. One big difference, however, was not mentioned before. The measurements conducted, showed the generation of discrete harmonics, which appear only for odd multiples

$$\omega_{\text{HHG}} = (2n+1) \omega_0 \quad (5.14)$$

of the fundamental frequency ω_0 .

The theoretical treatments described in this chapter, on the other hand, generate a continuous spectrum. In order to resolve this conflict, the properties of the generating laser pulse have to be taken into account. Both the three-step-model and the quantum-mechanical model only use a single atom and describe the atomic response to the laser-field for one ionization event. This means, they only model the generation process for one electron from ionization to recombination.

In the experiments where discrete lines are observed, however, multi-cycle laser pulses are used to generate high-order harmonics from a gas-jet or inside a gas-cell or a hollow-core fiber. As such, many atoms, which can be treated individually as single atoms, are involved and the observed experimental spectrum is a macroscopic build-up of microscopic high-order harmonic generation. Now it can

be understood why the observed spectrum shows discrete lines of only odd harmonics.

Using a multi-cycle laser pulse, the generation of high-order harmonics with one specific energy happens every half-cycle of the laser pulse, and the harmonics are emitted every $\Delta t = \frac{T}{2}$. Temporal interference of many atoms along the path leads to a coherent superposition of the emitted harmonic radiation. As the temporal structure and the spectral structure are connected through the Fourier transform, the periodic emission leads to a discrete line spectrum with spacing $\Delta\omega = \frac{2\pi}{\Delta t} = 2\omega_{\text{Laser}}$ where only odd harmonics are generated.

In some systems the symmetry regarding the direction of the electric field vector might be broken, e.g., by shaping the temporal properties of the electric field [72–74]. In these systems, high-order harmonics with one specific energy are only generated every whole cycle of the electric field. In this case, even and odd harmonics are generated.

5.1.4 Summary

In this section the single atom response to a strong external laser field was discussed to describe the generation of high-order harmonics. It was shown that the simple, quasi-classical three-step-model and the full quantum-mechanical treatment of the problem yield remarkably similar results. Hence, the three-step-model is still used widely to describe the process of high-order harmonics generation.

As another fact, it was shown that, in the experiment, high-order harmonic generation is a coherent macroscopic build-up of a microscopic effect. As many single atoms contribute to the overall signal, it is necessary to ensure that contributions from all atoms along the beam path interfere constructively, to efficiently generate high-order harmonics. To examine the generation properties along the beam path, phase matching phenomena regarding high-order harmonic generation should be discussed.

5.2 Phase matching

During high-order harmonic generation, many single atoms contribute to the overall signal. This happens due to the interference of the signals created by the single atoms along the path of the fundamental laser beam which drives the high-order harmonic generation. In order to maximize the generated high-order harmonic signal, it is necessary that the signal generated by the first atom and the signal of all following atoms can interfere constructively, until the very last atom.

This constructive interference of all contributions can only happen, if the fundamental laser beam and generated high-order harmonic radiation have the same propagation properties along the beam path. Mathematically, this can be written as the

phase mismatch of the wave vectors, between the q th harmonic and the fundamental beam. For a collinear geometry it is given by

$$\Delta k = q k(\omega_0) - k(q \omega_0). \quad (5.15)$$

Here q is the order of the harmonic and ω_0 is the angular frequency of the fundamental laser beam. To ensure that all contributing partial signals interfere constructively, the phase mismatch must be

$$\Delta k \stackrel{!}{=} 0. \quad (5.16)$$

As mentioned above, the high-order harmonic generation is based on strong field effects on atoms. As such, high intensities in the vicinity of the atoms are needed and it is necessary to focus a laser beam onto a target. In the experiments conducted in this work, a gas target was used.

As the high-order harmonic generation happens inside a gas target under the influence of a laser beam, different physical effects influence the propagation properties of the fundamental beam and the high-order harmonic radiation. As such, the phase mismatch can be separated into the contributions from these effects. By neglecting minor contributions [75], the overall phase mismatch from the major contributions can be written as

$$\Delta k = \Delta k_{\text{disp.}} + \Delta k_{\text{plasma}} + \Delta k_{\text{geom.}}. \quad (5.17)$$

Here $\Delta k_{\text{disp.}}$ is the contribution of the dispersion of the used gas. As high-order harmonic generation is only one consequence of the interaction of the gas with the strong laser field, most of the generated free electrons do not recombine with their mother ions creating a plasma. This plasma contributes Δk_{plasma} to the phase mismatch. The fundamental laser beam has to be focused onto the gas target to generate high-order harmonics. Due to this, geometric effects, as described in Chapter 1, influence the phase mismatch. The contribution $\Delta k_{\text{geom.}}$ is the result of these effects.

In the following, each contributions to the phase mismatch between the fundamental laser pulse and the q th harmonic shall be discussed in more detail.

5.2.1 Neutral Dispersion

High-order harmonic generation can only take place inside a medium. The wave vector $k = n \frac{\omega}{c_0}$ depends directly on the refractive index of the medium. This way, the dispersion of the medium, given by the fact that the refractive index $n(\omega)$ is frequency dependent, contributes

$$\Delta k_{\text{disp.}} = \left(n(\omega) - n(q \omega) \right) \frac{q \omega}{c_0} \quad (5.18)$$

to the phase mismatch. Here only the difference of the refractive indices plays a role. The dispersion of a material is governed by resonances inside the medium [2].

For frequencies not too close to a resonance, Sellmeier's equation [2] can be used to calculate the refractive index.

Using a simple approximation, the refractive index of the gas roughly scales linear with the atomic density N_a [1] and can be written as

$$n(\omega) = N_a \delta(\omega), \quad (5.19)$$

where $\delta(\omega)$ is the dispersion per atom of the neutral gas.

For typical gases used in high-order harmonic generation, the index of refraction in the XUV range, i.e., the range of the generated high-order harmonic radiation, is lower than the index of refraction in the near-IR and visible regime. Thus the contribution of the dispersion of the neutral atoms to the phase mismatch is

$$\Delta k_{\text{disp.}} > 0. \quad (5.20)$$

5.2.2 Plasma Dispersion

As mentioned above, only a small fraction of the generated free electrons produces high-order harmonic radiation. The majority of the electrons do not recombine with their parent ions, creating a plasma.

The timescale of the recombination of the free electrons with the ions in a plasma is in the order of nanoseconds. The duration of the laser pulses typically used for high-order harmonic generation, on the other hand, is on the timescale of several femtoseconds (up to about 300 fs). Hence, recombination inside the plasma can be neglected during high-order harmonic generation.

As the plasma is produced even at the leading edge of the laser pulse, it can be assumed that during the high-order harmonic generation it is already present. Thus, the contribution of the dispersion to phase matching, created by the plasma has to be taken into account.

When the cloud of free electrons is excited by an external field, it can start a collective oscillation. This oscillation has a resonance frequency given by

$$\omega_p = \sqrt{\frac{e^2 N_e}{\epsilon_0 m_e}}, \quad (5.21)$$

the so called plasma frequency. Here e is the unit charge, N_e the density of the free electrons and m_e the electron mass.

The resonance created by the plasma leads to a contribution to the refractive index

$$n_{\text{plasma}}(\omega) = \sqrt{1 - \left(\frac{\omega_p}{\omega}\right)^2}. \quad (5.22)$$

For frequencies $\omega < \omega_p$, the refractive index becomes purely imaginary. This means that the plasma becomes opaque for these frequencies. The critical density at which the plasma becomes opaque for a given frequency ω can be calculated from Equation (5.21) as

$$N_c(\omega) = \frac{\epsilon_0 m_e \omega^2}{e^2}. \quad (5.23)$$

Typical conditions for high-order harmonic generation result in plasma densities $N_e \ll N_c(\omega)$ for the fundamental laser beam. Thus, the refractive index given by Equation (5.22) can be approximated by

$$n_{\text{plasma}}(\omega) \approx 1 - \frac{1}{2} \left(\frac{\omega_p}{\omega} \right)^2. \quad (5.24)$$

Together with Equation (5.18), this leads to a phase mismatch of the q th harmonic of

$$\Delta k_{\text{plasma}} = -q \frac{\omega}{c_0} \frac{1}{2} \left(\frac{\omega_p}{\omega} \right)^2 = -q \frac{\omega_p^2}{2 c_0 \omega}. \quad (5.25)$$

Thus, the contribution of the plasma to the phase mismatch is

$$\Delta k_{\text{plasma}} < 0. \quad (5.26)$$

5.2.3 Geometric Effects

In Chapter 1 it was shown that a focused laser beam experiences an additional phase shift of π when going through the focus. Along the optical axis, this Guoy phase shift is given by Equation (1.24). For a region in the vicinity of a focus located at $z = 0$, i.e., $|z| \ll z_R$, the Gouy phase shift can be written as

$$\Delta\phi(z) = \arctan\left(\frac{z}{z_R}\right) \approx \frac{z}{z_R}. \quad (5.27)$$

Here z_R is the Rayleigh range, which characterizes the “length of the focus”.

The process of high-order harmonic generation is a coherent nonlinear process. Thus, the high-order harmonics inherit some of the properties of the driving laser pulse. One important parameter is the Rayleigh range. High-order harmonics in the perturbative regime and in the cut-off region have the same Rayleigh range as the driving laser pulse [76, 77]. This leads to the case that the phase shift for the fundamental laser beam and the high-order harmonics is the same. The contribution of the Guoy phase shift to the wave vector is given by

$$k(\omega) = \frac{\Delta\phi(z)}{z} = \frac{1}{z_R}, \quad (5.28)$$

which in fact only depends on the Rayleigh range. For high-order harmonics in the plateau region, however, the spatial beam profiles show distortions [77, 78]. Thus,

the beams can no longer be treated as pure Gaussian beams and the geometric phase shift is quite complex [79].

Other phase shifts stemming from nonlinear geometrical effects, e.g., nonlinear phase shift of a focused Gaussian beam due to third-order and fifth-order susceptibilities [33, 80], are possible. Since the contributions of these effects are generally much smaller than the contribution from the Guoy phase shift, they are usually neglected. For a rigorous treatment, however, they have to be taken into account.

The phase mismatch introduced by geometrical effects, in this case only the Guoy phase shift, is given by

$$\Delta k_{\text{geom.}} = q k(\omega_0) - k(q \omega_0) = \frac{q-1}{z_R}. \quad (5.29)$$

It should be noted that in the above example, the start of the interaction was assumed to be at $z = 0$. Thus, high-order harmonic generation starts exactly at the focus. By varying the position of the focus with respect to the position where the generation of high-order harmonics begins, it is possible to adjust the value of the phase mismatch introduced by the geometric effects.

For typical high-order harmonic generation schemes the contribution of the geometrical effects to the phase mismatch is

$$\Delta k_{\text{geom.}} > 0 \quad (5.30)$$

5.2.4 Summary

As mentioned above, efficient high-order harmonic generation can only take place when phase matching is ensured. Considering only the above mentioned effects, perfect phase matching implies

$$\Delta k = \underbrace{q \frac{\Delta n \omega}{c_0}}_{\Delta k_{\text{disp.}} > 0} - \underbrace{q \frac{\omega_p^2}{2 c_0 \omega}}_{\Delta k_{\text{plasma}} < 0} + \underbrace{\frac{q-1}{z_R}}_{\Delta k_{\text{geom.}} > 0} \stackrel{!}{=} 0. \quad (5.31)$$

It is obvious that the different contributions to the phase mismatch need to be balanced.

In Equation (5.31) it can be seen that phase matching occurs if the contribution of the plasma to the phase mismatch cancels out the contributions of the dispersion of the neutral gas and the phase mismatch due to geometric effects. For a better identification of the external control parameters it is convenient to rewrite Equation (5.31) using the relations mentioned above. This leads then to

$$\Delta k = N_a \frac{q \omega \Delta \delta}{c_0} - N_e \frac{q e^2}{2 \epsilon_0 m_e c_0 \omega} + \frac{q-1}{z_R}. \quad (5.32)$$

In this form it is transparent that by varying the density of the neutral atoms N_a and electron density N_e of the plasma it should be possible to ensure phase matching.

The density of the neutral atoms and the electron density of the plasma is connected by the ionization rate. Thus, by varying the gas pressure and the intensity at the laser focus it is possible to control phase matching.

Part II

Experiments

Chapter 6

The experimental setup

In order to generate high-order harmonic radiation from ultra-short laser pulses in the lab, a modular vacuum setup was built [81]. It consists of several vacuum chambers which are mounted on a rail system for easy configuration. The setup for the generation of high-order harmonics after temporal compression of the laser pulse by an optimized filament is shown in Figure 6.1. The setup consists of a commercial

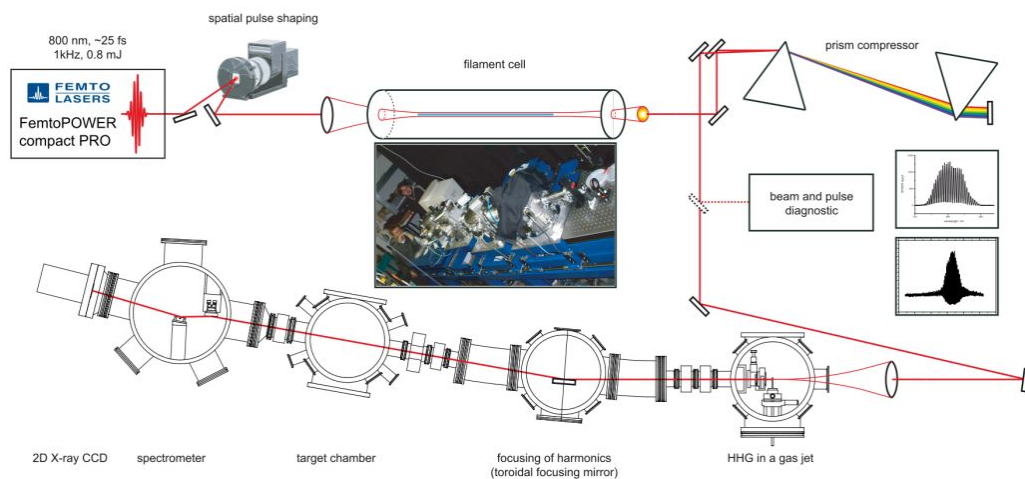


Figure 6.1: Overview of the experimental setup. The setup consists of five major sections. The first section is the FemtoPOWER compact PRO amplifier system. The second part is the spatial light modulator for beam shaping. The third part is a temporal compression setup, consisting of a gas cell for self-phase modulation inside a filament and a prism compressor. The fourth section contains different beam and pulse diagnostic tools. The last part contains the high-order harmonic generation setup.

femtosecond laser system, a spatial light modulator, a setup to further shorten the laser pulses and the vacuum system for the high-order harmonic generation. The optimization is done using a genetic algorithm which controls the spatial light modulator. In the following, each part is shortly described.

6.1 Laser system

The laser system used during this work is a commercially available FemtoLASERS FemtoPOWER compact PRO. It is a femtosecond amplifier system based on a multi-pass CPA amplification scheme [29, 82]. In Figure 6.2 the principle of the laser system is shown. A Ti:sapphire oscillator, pumped by a green Nd:YVO₄ cw-laser,

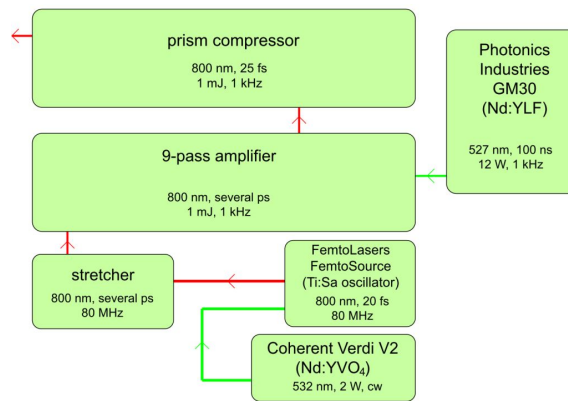


Figure 6.2: The FemtoPOWER compact PRO femtosecond amplifier system. The FemtoSOURCE Ti:sapphire oscillator delivers weak femtosecond pulses. The pulses are stretched to several picoseconds in the stretcher, using chirped mirrors. The stretched pulses can then be safely amplified in another Ti:sapphire crystal. During the nine passes in the amplifier stage, the repetition rate is reduced by a Pockels cell. Afterwards the pulses are recompressed by a prism compressor. The green lasers are needed for pumping the Ti:sapphire crystals.

delivers “weak” femtosecond laser pulses with a repetition rate of 80 MHz. In the next step, the pulses are stretched to several picoseconds using chirped mirrors. This is done to reduce the peak intensity of the laser pulses in order to avoid damage of the amplifier crystal. The amplification of the laser pulses takes place in a multi-pass amplifier stage. There, a second Ti:sapphire crystal, pumped by a Q-switched green Nd:YLF laser, is used as gain medium. The laser pulses are amplified during nine passes through the gain medium. After the fourth pass, one out of 80000 laser pulses is selected, effectively reducing the repetition rate of the amplifier system to 1 kHz. The pulse selection is done using a Pockels cell between crossed polarizers as pulse picker. After the amplification the laser pulses are recompressed by a prism compressor.

The FemtoPOWER compact PRO used during this work can deliver laser pulses with a pulse energy of up to 1 mJ and a pulse duration of about 30 fs (FWHM).

6.2 Spatial Light Modulator

In order to control the wavefront of the laser pulses a spatial light modulator (SLM) is used. The SLM can modify the phase of the laser beam in two dimensions and it is possible to fully control the wavefront of the beam. Two different SLMs were used during this work. Both SLMs were supplied by Hamamatsu Photonics.

6.2.1 The PPM-SLM

The Hamamatsu PPM-SLM X8267, shown in Figure 6.3, works in reflection and has an addressable resolution of 768×768 pixels. Only a short description of the PPM-SLM is given here. For more details on the properties of the PPM-SLM X8267 see [26, 49, 83]. The phase is controlled by a computer. The green level of the VGA



Figure 6.3: Hamamatsu PPM-SLM X8267 [84].

output of a conventional graphics adapter serves as modulation signal. For the X8267 a green level of 255 represents a phase shift of roughly 2π . The exact phase shift depends on the wavelength of the readout light.

The working principle of the PPM-SLM is quite sophisticated. A laser diode images a conventional XGA-LCD onto the back of the modulation area. The actual modulation is done by liquid crystals. The orientation of the liquid crystals defines the phase modulation and depends on the amount of light which hits the back of the modulation area.

Because the imaging of the LCD on the active area is slightly out of focus, the pixels appear a little blurry. This is done deliberately, because this way it is possible to create an output image which shows no pixel structure. The main advantage of this is the greatly reduced diffraction noise, which normally occurs due to pixelation. On the downside, this reduces the effectiveness of sharp phase jumps, which are needed for desired modulation depths greater than 2π .

6.2.2 The LCOS-SLM

Some major disadvantages of the PPM-SLM are the limited damage threshold, which is less than the maximal achievable intensity of the amplifier system, and the problem of phase modulation by readout light [49, 83]. In order to be able to use the full pulse energy of the amplifier system, the LCOS-SLM X10468-02, shown in Figure 6.4, was used. The LCOS-SLM has a resolution of 800×600 pixels. Similarly



Figure 6.4: Hamamatsu LCOS-SLM X10468-02 [85].

to the PPM-SLM it can be controlled by a conventional graphics adapter. As the LCOS-SLM is the successor of the PPM-SLM, it uses a modern DVI connector. The LCOS-SLM uses the gray level as signal and a phase modulation of approximately 2π , again depending on the wavelength, is achieved for a white output image of the computer.

The actual modulation is also done by liquid crystals. In contrast to the PPM-SLM the orientation of the liquid crystals is controlled by a CMOS backplane. On the one hand, this leads to some pixelation effects, on the other hand, the readout light does not produce any phase modulation itself. Additionally, the CMOS backplane is more robust and has a much higher damage threshold.

Because both SLMs use a conventional graphics adapter the software created for the PPM-SLM also works for the LCOS-SLM. Only the use of a black/white color table instead of a black/green color table must be ensured.

6.2.3 Closed-loop optimization

For nonlinear effects, the influence of the spectral or spatial phase is also nonlinear. In most cases, for a given nonlinear effect, the phase which leads to the desired result cannot be calculated analytically. Hence, finding a suitable phase profile poses an optimization problem [86]. Many optimization methods are available to search for good solutions of the problem [86]. These optimization methods are mostly closed-loop optimizations. These closed-loop algorithms use the result of one iteration

as parameter in the next iteration. Many of these methods, for example particle swarm optimization, simulated annealing or evolutionary algorithms, are inspired by nature.

In this work a genetic algorithm, which is a particular implementation of an evolutionary algorithm, was used. The use of genetic algorithms for the optimization of laser pulses in order to control quantum mechanical systems was first described by Judson and Rabitz [87]. The genetic algorithm used in this work is very similar to the one given by Judson and Rabitz and is described in more detail in Appendix C.

6.3 Temporal compression

As mentioned in Section 3.1, the pulse duration and the spectral bandwidth of a laser pulse are linked. With the help of the so called time-bandwidth product, given by Equation (3.9), it is possible to calculate the minimum pulse duration for a given spectral bandwidth. Thus, in order to temporally compress a laser pulse it has to be spectrally broadened.

In a first step, the nearly bandwidth limited laser pulse from the amplifier system is spectrally broadened by the nonlinear effect of self-phase modulation. The effect of self-phase modulation is discussed in more detail in Section 4.1.1. For efficient and homogeneous spectral broadening by self-phase modulation, the laser beam has to be small over quite a long distance. In order to achieve this, the laser beam has to be guided.

One possible way to guide the laser is the use of a gas-filled hollow-core fiber. This was done during previous projects and was studied in detail in [26, 49, 68, 83]. Another approach to achieve a long interaction region with a small cross-section, is to use the self-guiding of the laser beam by filamentation. The effect of filamentation is the interplay between Kerr self-focusing and plasma diffraction and is discussed in Chapter 4.

A filament can be created simply in air. Due to pressure variations and air movement in the lab, filamentation becomes unstable and the self-phase modulation fluctuates strongly. In order to stabilize the self-phase modulation, a gas cell with a controlled environment is used. This gas cell is about 1.6 m long and can be filled with argon gas at an adjustable pressure between 1 mbar and 2 bar.

Due to spectral broadening, the pulse is no longer bandwidth-limited after self-phase modulation and the chirp has to be compensated. This is done using a pair of prisms, forming a prism compressor. A full discussion of the properties of a prism compressor can be found in [29].

At the exit of the temporal compression setup, the pulse is now significantly shorter than at the beginning. Due to the optical elements used, some energy loss occurs. In terms of intensity, the energy loss is more than compensated by the shorter pulse duration.

In the experimental setup used in this work the transmission of the temporal compression setup is about 70%. The pulse duration, however, is shortened by a factor of about 2. This leads to an intensity increase of roughly 40%.

6.4 Beam and pulse diagnostics

In order to characterize the beam and pulse parameters, several diagnostic tools are available. In the following, these tools are shortly described.

For beam diagnostics a near-infrared sensitive CCD is used. Typical commercially available CCD cameras use an infrared filter to reproduce the color sensitivity of the eye. This filter is needed because in the near-infrared the CCD is still sensitive to light whereas the eye cannot detect light in this region. Without the infrared filter the color of the images produced by CCDs would appear strange. With the filter in place, the color impression of the pictures seems much more natural to the human eye. Because the filters are typically built to filter out light at wavelengths longer than 800 nm, they are not suitable to analyze the beam profile of a Ti:sapphire laser. Some difficulties concerning the use of standard CCDs for beam characterization are described in Chapter 7. In order to avoid some of the difficulties, a machine vision camera without any spectral filtering is used. In first experiments a Sony XC-ST50CE CCD was used. In later experiments this camera was replaced by a DALSA Genie M1024 CCD camera.

In order to characterize the pulse, two different tools are available. The first is an interferometric autocorrelator and the second is a SPIDER setup.

The interferometric autocorrelator was built using a Michelson interferometer and a two-photon photodiode as detector [88]. With the help of the autocorrelator it is possible to directly measure the pulse duration. In later experiments a commercially available autocorrelator, capable of measuring pulse durations shorter than 10 fs was used. This autocorrelator, the FemtoLASERS FemtoMETER [89], provides a faster and easier readout of the signal.

The autocorrelator, however, is only suitable for measuring the pulse duration. In order to fully characterize the pulse the phase has to be determined. This can be achieved using techniques other than an autocorrelator. Among others, e.g., the frequency-resolved optical gating or FROG [29, 90], the spectral-phase interferometry for direct electric-field reconstruction, shortly called SPIDER [91], is suitable to fully characterize the pulse. In this work, a SPIDER setup was available for pulse characterization. The properties of this specific SPIDER setup are discussed in [26, 49, 68].

6.5 High-order harmonic generation

In order to generate high-order harmonics, a vacuum setup is available. In principle, different generation geometries are possible. Some examples are, the generation in a gas jet, a capillary or in water droplets. For an overview see [68] and elsewhere.

In this work, the generation of the high-order harmonics was realized in a gas-filled nickel tube. The setup is shown in Figure 6.5. The gas is contained in a small nickel

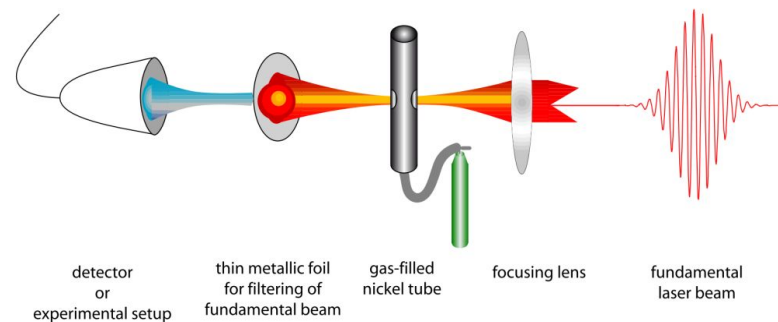


Figure 6.5: High-order harmonic generation inside a gas-filled nickel tube. The laser is focused into a gas-filled nickel tube to generate high-order harmonics. Before the experiment the tube is completely sealed and the laser then drills holes, only as large as needed, into the front and the back of the tube. After the high-order harmonic generation, a thin metal foil is used to filter the fundamental laser light out of the beam. The high-order harmonics are then detected with a XUV sensitive detector.

tube. Before the experiments the tube is completely sealed. The laser then drills holes into the front and the back of the tube. These holes are only as small as the beam diameter and only little gas can flow from these holes into the vacuum. This way only the interaction region contains a significant amount of gas. With respect to focusing and phase-matching conditions, this configuration is identical to the gas jet. The main difference is the greatly reduced background pressure in the vacuum chamber, compared to a free flowing continuous gas jet.

As the wavelength of the generated high-order harmonic radiation is in the XUV range, vacuum conditions are necessary for propagation. Therefore, all of the following components are placed in vacuum chambers. Each chamber is mounted on rails for fast and easy movement and configuration. The typical setup of the chambers is shown in Figure 6.6. From right to left the chambers serve the following purpose:

The first chamber is the generation chamber and contains the nickel tube. It is connected to the following chamber only by a small hole through which the light passes. This allows for differential pumping and greatly reduces the background pressure in the following vacuum chambers.

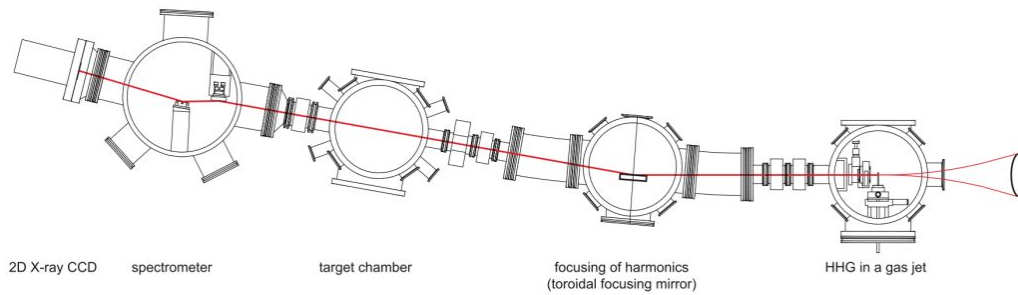


Figure 6.6: The vacuum setup. The vacuum chambers for high-order harmonic generation and for the experiments are mounted on rails for fast and easy movement and configuration. The first chamber, called generation chamber, contains the nickel tube for the high-order harmonic generation. The second chamber contains a toroidal mirror for focusing the high-order harmonics into the experimental chamber. The experimental chamber has many connectors to accommodate different experiments. The last chamber contains a grazing incidence spectrometer which was specifically designed for this setup [88]. It images the focal spot of the high-order harmonics in the experimental chamber onto the detector.

The second chamber contains a toroidal mirror for focusing the high-order harmonics. The toroidal mirror has a gold-coating and is used in grazing incidence. The focusing geometry is designed in such a way that the image of source of the high-order harmonic radiation, i.e., the focal spot of the fundamental laser inside the nickel tube, is created at the center of the adjacent experimental chamber. The magnification is chosen to be 1. Due to the angle, which is introduced by the mirror, this and the following chambers are not aligned in a straight line. In order to compensate for the bending, the focusing chamber is connected to its neighbors by bellows.

The third chamber is the experimental chamber. The chamber has many connectors to accommodate different experiments. Connecting an electron time-of-flight spectrometer, which is available from another team in the work group [92], is also possible.

The last chamber contains a grazing incidence spectrometer. It was specifically designed for this setup [88], as it images the focal spot of the high-order harmonics in the experimental chamber onto the detector. The detector, in this case, is a back-illuminated X-ray CCD (Andor DO420BN [93]). The spectrometer was later replaced by a commercially available McPherson 248/310G grazing incidence spectrometer. It is described in detail in Appendix D.

In order to filter the fundamental laser light from the beam, several thin metallic foils can be used. They are placed inside special valves in front of and behind the focusing chamber.

Chapter 7

Spatial optimization of filaments

In order to compress ultra-short laser pulses in the time domain the spectrum has to be spectrally broadened (see Chapter 3). This can be done using the nonlinear effect of self-phase modulation. For self-phase modulation to be efficient the laser beam has to be guided. Typically, the guiding of the beam is achieved by a hollow-core fiber [94]. As interaction medium for the self-phase modulation, the hollow-core fiber is filled with a noble gas at variable pressure to control the spectral broadening. This way, laser pulses with a pulse duration of only a few optical cycles [95, 96] can be achieved. This technique is well studied and widely used. It has, however, some limitations and disadvantages which should be discussed in the following.

First, the energy of the input pulse is limited to a few mJ pulse energy. This limit stems from the fact that the pulse has to be efficiently coupled into the hollow-core fiber. Therefore, the beam width at the entrance of the fiber has to be matched to the size of the channel inside the hollow-core fiber. Due to the intensities involved, even for a well matched beam size the glass at the entrance of the hollow-core fiber starts melting. This leads to a degradation of the fiber entrance so that the fiber has to be replaced regularly. For pulse energies exceeding a certain limit this effect is too fast and prevents the laser beam to be coupled efficiently into the hollow-core fiber.

Another disadvantage of hollow-core fibers is their transmission characteristic. Even small irregularities inside the hollow-core fiber lead to scattering losses. These losses lead to a transmittance of about 75 % under optimal conditions. Under typical experimental conditions a transmittance of about 50 % to 60 % can be achieved. Additionally, the laser beam can excite different transversal modes inside the fiber. Which modes are excited depends strongly on the properties of the beam at the entrance and even small changes in the beam profile, the exact beam position and the beam pointing strongly influence the propagation inside the fiber [83]. These effects make an external beam stabilization necessary or otherwise reduce the usability of temporal compression by hollow-core fiber setups.

Another way for efficient spectral broadening of laser pulses is the use of the self-guiding effect of filamentation of ultra-short laser pulses. The basics effects leading to filamentation and some of the properties of a filament are described in Chapter 4.

From previous works (e.g., [97]) the occurrence of multi-filamentation is well known. Multi-filamentation occurs if the laser power strongly exceeds the critical power for self-focusing [98]. Some of the studies show that multi-filamentation can be influenced by controlling laser parameters like beam width [99], astigmatism [100] or ellipticity [101].

In order to see if filamentation can be used to replace a hollow-core fiber the transmission properties of the filament were checked first. In a second step, the laser beam was spatially shaped prior to filamentation in order to optimize the properties of the beam [102]. This optimization was done using the closed-loop optimization scheme given in Section 6.2.3.

7.1 Experimental setup

The experimental setup used to investigate the properties of filamentation is described in detail in Chapter 6. Here only a short summary is given. The setup is

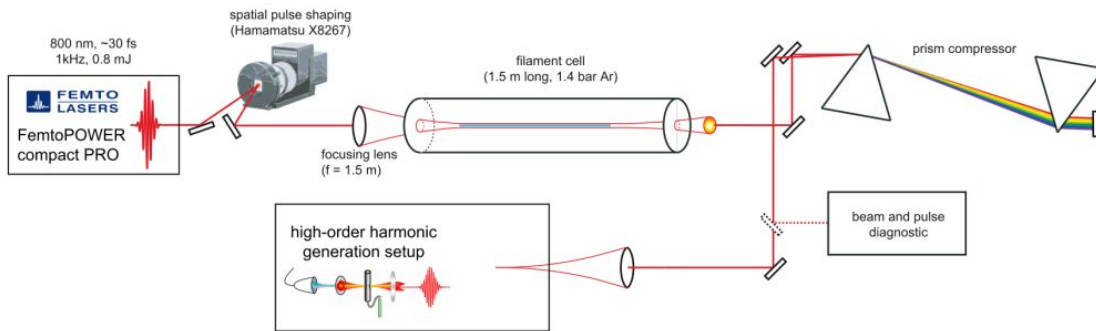


Figure 7.1: Experimental setup for the investigation of the properties of filamentation. For a detailed description see Chapter 6.

shown in Figure 7.1. The multi-pass amplifier delivers laser pulses with a duration of about 30 fs which are directed onto the Hamamatsu X8267 spatial light modulator. There, the wavefront of the laser pulses is shaped as described in Section 6.2.1. Afterwards, the spatially modulated beam is focused into the filament cell using a lens with a focal length of $f = 1.5$ m. The filament cell itself is filled with argon gas at a pressure of 1.4 bar. The entry and exit windows of the gas cell are thin (5 mm) fused silica windows used in normal incidence. After the filament cell a small lens is used to collimate the beam. The collimated laser beam is temporally recompressed using a prism compressor. This way, laser pulses with a pulse duration of about 13 fs, measured with the SPIDER technique, are achieved. In the last step, the shortened laser pulses are used to create XUV radiation using the process of high-order harmonic generation. This is done inside the vacuum chambers of the high-order harmonic generation setup.

In order to investigate the properties of filamentation different beam and pulse diagnostics are available. For beam diagnostics an infrared sensitive CCD camera (Sony XC-ST50CE) is present. For pulse diagnostics an interferometric autocorrelator and a SPIDER setup can be used.

7.2 Spatial beam properties after filamentation

After filamentation was successfully observed, the influence of laser intensity and gas pressure were investigated [26]. This way, the experimental parameters for stable filamentation were determined. Using a lens of focal length $f = 1.5$ m and a gas pressure of 1.4 bar inside the filament cell, a filament with a length of about 15 cm was created. Figure 7.2 shows a picture of the actual filament inside the gas cell.

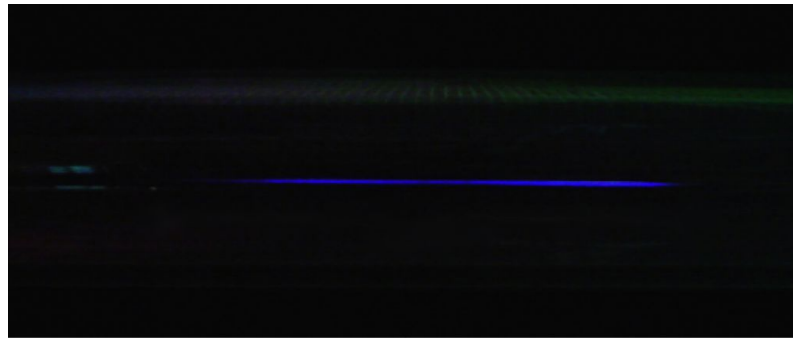


Figure 7.2: Picture of the actual filament inside the gas cell. The filament itself is about 15 cm long.

7.2.1 Beam profile

In the next step, the beam profile after the filament was investigated. When using the naked eye to examine the beam profile, only the visible parts of the spectrum can be seen. In Figure 7.3a) the image of the beam profile as seen with the naked eye is shown. The central part of the beam appears nearly white, whereas the outer part is blue. This blue part comes from conical emission [103] which is present during filamentation.

The image was taken with a standard digital camera for photography. These cameras are typically based on CCDs and use an infrared filter for correct color reproduction. Typical CCDs are sensitive to near-infrared light which the human eye cannot detect and images taken without an infrared filter would have a strange color representation. The filters used in photographic digital cameras typically filter out light with wavelengths longer than 800 nm. Thus, the image taken with the digital camera does not show a realistic beam profile.

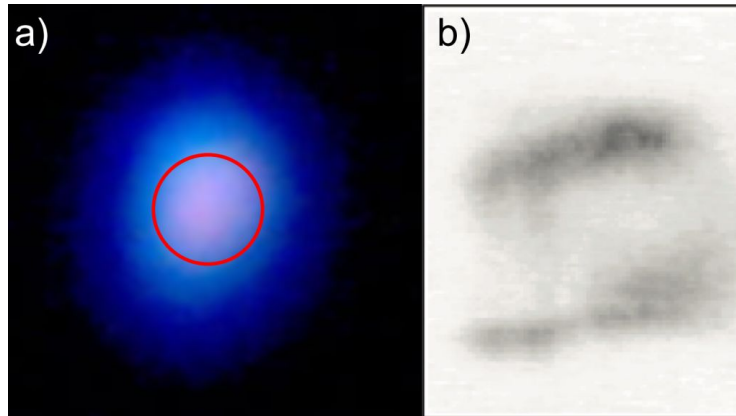


Figure 7.3: Beam profile after filamentation. Images taken with a) a photographic digital camera (VIS) and b) a near-IR sensitive CCD. The red circle in a) approximately marks the region which is shown in b).

In order to measure the beam profile correctly, a machine vision CCD without infrared filter (Sony XC-ST50CE) was used. Because the central part of the beam contains mainly light in the near-infrared it is much more dominant than the outer part and the laser beam had to be attenuated. This way, the outer (blue) part was not detected by the machine vision CCD. In Figure 7.3b) the unfiltered beam profile is shown. The central part, marked by the red circle in the visible image, is magnified to show more details of the beam profile.

As can be seen, the beam profile in the infrared does not resemble the beam profile as seen with the naked eye. The visible beam profile appears to be quite regular, whereas the near-infrared part clearly shows distortions of the central part. Because of these beam distortions, the focusability of such a beam is reduced. In cases where tight focusing is necessary, e.g., for high-order harmonic generation, such a beam profile is not optimal.

7.2.2 Spatial chirp

In this work, filamentation serves as a tool for sustained self-phase modulation of the laser pulse, as described in Chapter 4. To allow for efficient temporal compression of the laser pulse, the spectral broadening should be homogeneous over the whole beam. In order to evaluate the homogeneity of the spectral broadening the spectrum at different parts of the beam was recorded. In the following, differences of the spectrum at different parts of the beam are called spatial chirp. This, however, does not correspond to the effect of spatial chirp in ultrafast optics [104], e.g., created in prism compressors.

In Figure 7.4a) the approximate positions of the recorded spectra are shown. The spectrum at the center of the beam, labeled position 5, was taken as reference spec-

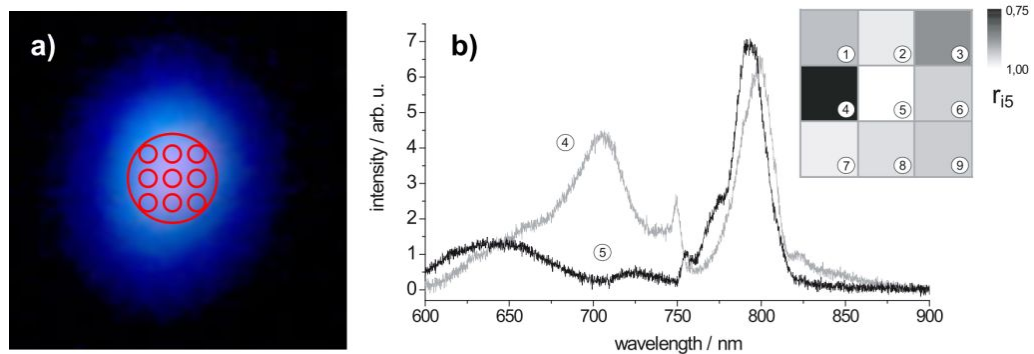


Figure 7.4: Evaluation of the spatial chirp at different positions in the beam. a) Approximate positions of the measured spectra. b) Spectra taken at two different positions in the beam. The inset shows the values of the correlations between the spectrum at position i and the reference spectrum at position 5.

trum. For easier comparison of different beam parts, the correlation

$$r_{i5} = \frac{\int I_i(\lambda) I_5(\lambda) d\lambda}{\sqrt{\int I_i(\lambda)^2 d\lambda \int I_5(\lambda)^2 d\lambda}}, \quad (7.1)$$

of the spectral intensity $I_i(\lambda)$ at position i with respect to the reference was calculated.

In Figure 7.4b) the spectra at positions 4 and 5 are shown. These positions were selected because they yield the lowest correlation of $r_{45} = 0.77$. The data shown here is actually the reference data taken after the optimization which is described in the next section. The spectra recorded before the optimization, however, are very similar with respect to shape and relative intensity. As can be seen, the spectra differ substantially, which reduces the efficiency of the temporal compression. Additionally, the correlation for each position is shown in the inset at the top right. The average correlation of the spectra was $\langle r_{i5} \rangle_i = 0.92$.

These inhomogeneities are limiting factors for filamentation as a tool for self-phase modulation. As many experiments require defined pulse profiles, the beam has to be homogenized using apertures [105]. This reduces the overall transmittance and limits the intensity throughput.

7.3 Spatial optimization of filaments

In order to be able to use filamentation for self-phase modulation, the beam and pulse structures have to be optimized. In a similar setup, Pfeifer et al. [106] improved the pointing stability with the help of a fixed circular phase mask by using a SLM

similar to the one used in this work. In the setup used for this work the Hamamatsu X8267 SLM and a genetic algorithm for spatial shaping were already incorporated in previous experiments. This way, the setup could be easily modified to use a closed-loop optimization in order to improve filamentation. For this optimization the genetic algorithm was modified to use tiltable planes. This parameterization is described in Appendix C.

The symmetry of the spatial beam profile after filamentation was used as fitness function for the genetic algorithm. In order to evaluate the symmetry, the centroid of the beam was set as center of the evaluation. Afterwards, the image was split into four quadrants with an equal number of pixels. In a last step, the integrated intensities of each quadrant were compared. The signal from each quadrant should be equal for a symmetric beam. A reasonably symmetric beam shows only small differences in these signals, leading to a high fitness. An asymmetric beam, however, produces larger differences and thus has a lower fitness value.

In first experiments, the optimization always resulted in beams which showed no filamentation. The cause for this was found to be the symmetric input beam. Without filamentation, the beam stays symmetric and produces a higher fitness than a beam which undergoes filamentation. In order to avoid this effect an indicator for filamentation had to be included in the fitness function. Every time significant self-phase modulation occurred, a small part of the blue spectrum clipped at the edge of the end mirror of the prism compressor. The intensity of this blue part, which is only present because of self-phase modulation, was used as an indicator for filamentation. With the help of this indicator, the beam could be optimized without sacrificing filamentation.

In order to quantify the improvements, the effects of the optimization on the beam profile and the spatial chirp were investigated.

7.3.1 Effects on beam profile

The fitness function of the genetic algorithm is mainly defined by the symmetry of the beam. Therefore, the influence of the optimization on the beam profile is immediately evident.

The beam profile before the optimization is shown in Figure 7.5a). It clearly exhibits an asymmetry and the energy is distributed over two distinct areas. This might be a sign of multi-filamentation.

Using this beam as initial condition, the genetic algorithm with tiltable planes, as described in Appendix C, was used to optimize the beam. The optimization started using only one plane. During the course of the optimization, the number of planes was successively increased to 32×32 planes. Overall, 700 generations were tested, of which the last 300 generations already had the final number of 32×32 planes. The whole optimization took about two hours.

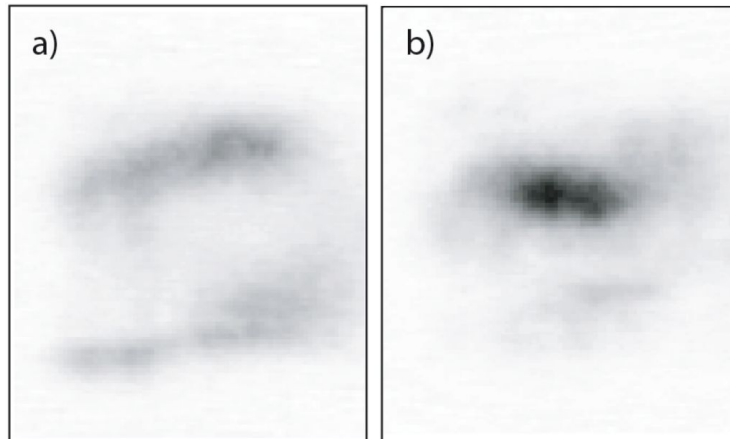


Figure 7.5: Beam profile a) before and b) after optimization taken with a near-infrared sensitive CCD.

After the optimization the beam profile was much more symmetric, as shown in Figure 7.5b). The distortions present in the initial beam were drastically reduced and a nearly Gaussian beam profile could be achieved. The position and the length of the filament inside the filament cell were also altered. The onset of filamentation moved about 2 cm nearer to the lens and the length of the filament increased by about 4 cm. Additionally, the divergence of the beam decreased for the optimized beam, leading to a higher intensity at the position of the camera.

7.3.2 Effects on spatial chirp

After the optimization was completed, the spectral properties of the beam were investigated. Especially the spatial chirp was examined in detail.

As described in Section 7.2.2, the spectrum at nine different positions in the beam was measured. For each position, spectra of the optimized beam and of the reference beam were recorded to allow for a comparison between those.

In Figure 7.6 the spectra at positions 4 and 5 in the beam are shown. Before optimization, the spectra, shown in Figure 7.6a), exhibit significant differences. After the optimization, however, the differences in both spectra are dramatically reduced, as shown in Figure 7.6b).

In order to quantify the differences between the spectra the same correlation function as described in Section 7.2.2 was used. The values of the correlation function are given by the insets in Figure 7.6. Note that the color scaling of the insets differs between Figure 7.6a) and Figure 7.6b). The average correlation of the spectra increased from $\langle r_{i5} \rangle_i = 0.92$ before the optimization to $\langle r_{i5} \rangle_i = 0.992$ after the optimization.

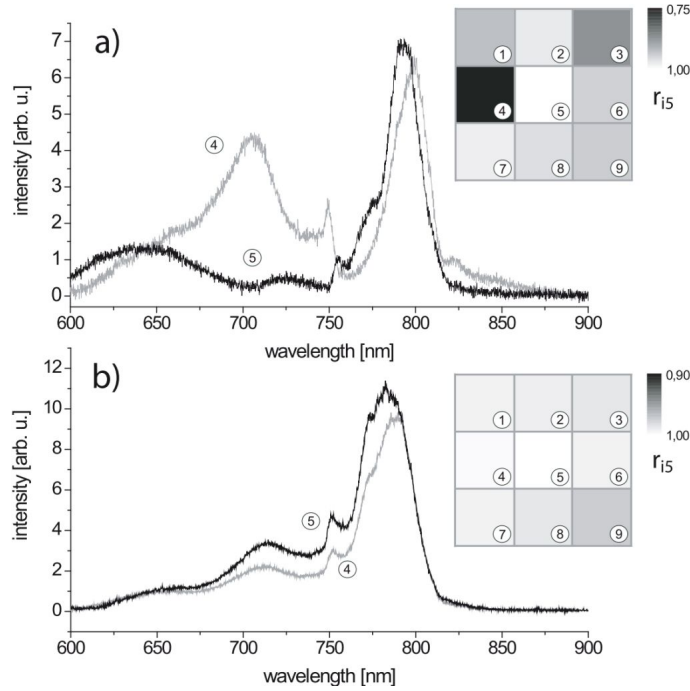


Figure 7.6: Spectra taken at two different positions in the beam a) before and b) after optimization. The insets show the values of the correlations between the spectrum at position i and the reference spectrum at position 5. For further details see Section 7.2.2. Note the different color scaling of the insets between a) and b).

With this measurement it could be shown that the beam optimization also reduced the spatial chirp after filamentation. This finding is remarkable because the definition of the fitness function described above does not contain any information about spatial chirp. In order to determine the fitness value only the symmetry of the beam and the width of the spectral broadening, which has only a small contribution coefficient, were considered.

7.3.3 Calculation of the beam profile

As mentioned in Chapter 2, it is possible to calculate the beam profile at any position if the wavefront and the intensity profile at one position are known. From the specifications [107] and previous measurements [26, 108] the beam quality of the amplifier system is known.

For the amplifier system the beam quality is quantified as $\mathcal{M}^2 \approx 1.2$ and the beam profile at the exit is nearly Gaussian. Hence, it is safe to assume a flat wavefront and a Gaussian profile of the collimated beam at the position of the SLM. The optimal phase-mask, found by the genetic algorithm, thus corresponds to the wavefront of the beam directly behind the SLM. Additionally, the properties of the

lens and the distances between the components are known. With these parameters the beam at a position shortly before the onset of filamentation was calculated.

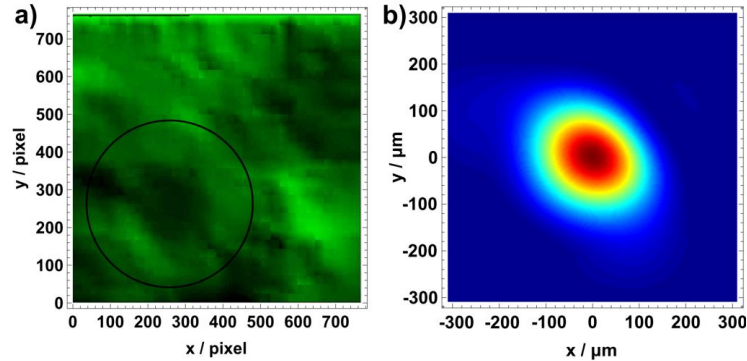


Figure 7.7: a) Phase mask at the SLM after optimization. The black circle marks the position and the size of the beam. b) Calculated beam profile of the optimal beam shortly before the onset of filamentation. The beam profile was calculated from the phase-mask assuming a collimated Gaussian beam at the SLM.

The calculation was done using Equation (2.22). The influence of the gas inside the filament cell was neglected. The intensities which occur up to this point allow for such a simplification. In order to calculate the propagation beyond this point, Kerr self-lensing and plasma effects must be taken into account.

In Figure 7.7a) the optimal phase-mask is shown. Additionally, a black circle marks the location of the Gaussian beam. The calculated beam profile shortly before the onset of the filament is shown in Figure 7.7b). It can be clearly seen that the beam profile at this point is significantly distorted.

7.4 Optimization of high-order harmonic generation after filamentation

The high-order harmonic generation, described in Chapter 5, strongly depends on the pulse duration. Therefore, it is reasonable to evaluate the influence of the temporal compression after filamentation on the high-order harmonic generation. This was done by using the high-order harmonic generation setup described in Chapter 6.

It could be shown that the compressed pulses were able to efficiently generate high-order harmonics. As the SLM was still present in this setup, another optimization run was conducted. This time the overall high-order harmonic yield was used as

fitness. As mentioned earlier the spatial optimization influenced the spectral broadening and the beam profile. This way a laser pulse with optimal parameters for high-order harmonic generation was created.

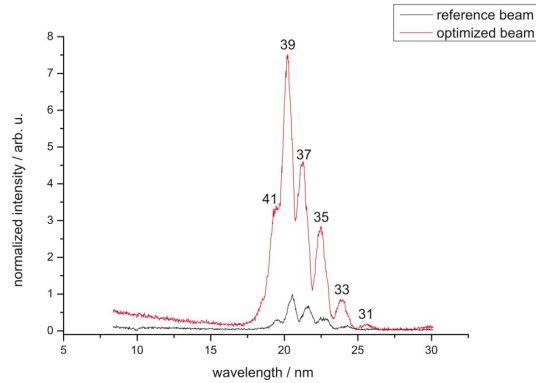


Figure 7.8: High-order harmonic spectrum after filamentation.

As can be seen in Figure 7.8, the shaped laser beam (red curve) is much better suited to create high-order harmonics than the reference pulse (black curve). The 39th harmonic, e.g., increased by a factor of about 8.

The optimization resulted in a very complex phase-mask. This phase-mask led to a complex beam profile but showed quite homogeneous spectral broadening. Thus, information about which factor led to the increased high-order harmonic yield cannot be easily retrieved. Further studies are needed to better understand how the beam profile of the fundamental laser beam influences the high-order harmonic generation.

7.5 Conclusion

Here it could be demonstrated that filamentation can be used for compression of an ultra-short laser pulse in the time domain. It was shown that initially the laser beam after filamentation shows some unwanted properties. With the help of a closed-loop optimization scheme it was possible, however, to improve important beam characteristics. This way, the spatial chirp and the distortions of the beam profile, present in the unoptimized beam, could be significantly reduced. The optimization scheme which realized these improvements was based on a genetic algorithm. These optimizations exhibited some interesting results. It could be shown that the spatial chirp is reduced automatically when the optimization goal is set to create a symmetric beam profile. Temporal recompression of this laser beam resulted in a laser pulse with a duration of about 13 fs. A down-chirp of the laser pulse after filamentation or even self-compression as mentioned in [105, 109–111] were not observed. Additionally, it could be shown that it is possible to create a laser pulse which is tailored specifically to improve the generation of high-order harmonics.

Chapter 8

Measuring the wavefront of high-order harmonics

As stated in the introduction many experiments rely on brilliant XUV sources. In order to decide which XUV source is suitable for a given experiment, comparing the characteristics of different sources is necessary. One such characteristic is the number of photons which the source emits. As different sources can have different emission characteristics it is not always enough to compare only the number of emitted photons.

Another quantity, which allows for easy comparison of different sources, is the brilliance or spectral brightness. It takes into account not only the photon flux, but also the size of the source and its emission characteristics. The brilliance is defined as

$$B = \frac{N_{\text{photon}}}{\Delta t \Delta \Omega \Delta A \frac{\Delta \omega}{\omega}}. \quad (8.1)$$

Here N_{photon} is the number of photons of a certain energy interval, measured by $\frac{\Delta \omega}{\omega}$, which are emitted by the source of the size ΔA into the solid angle $\Delta \Omega$ during the time interval Δt . For pulsed sources it is often reasonable to specify the peak brilliance B_{peak} , which takes into account that photons are emitted only during the pulse duration $\Delta t = \tau$. In Chapter 1 the beam parameter product, given by Equation (1.28), connects the waist size to the divergence angle of a beam. The product of the source area and the solid angle, which corresponds to the beam parameter product of a real beam, is minimal for diffraction limited beams, i.e., $\mathcal{M}^2 = 1$. Thus, diffraction limited beams have, by definition, the highest brilliance for a given spot size.

Much work has been done to optimize the spectral shape [112, 113], the photon flux [114] or the temporal properties [115] of high-order harmonic radiation. Reviews of much of this previous work are given by [116, 117] and elsewhere. Another approach for optimizing the brilliance is the control of the wavefront of high-order harmonics [118–120]. Hence it seems necessary to measure the wavefront of high-order harmonics in order to examine how the brilliance of the source can be maximized.

8.1 Experimental setup

The complete experimental setup is discussed in Chapter 6. Only the experimental characteristics which are different from those described there are given here. The

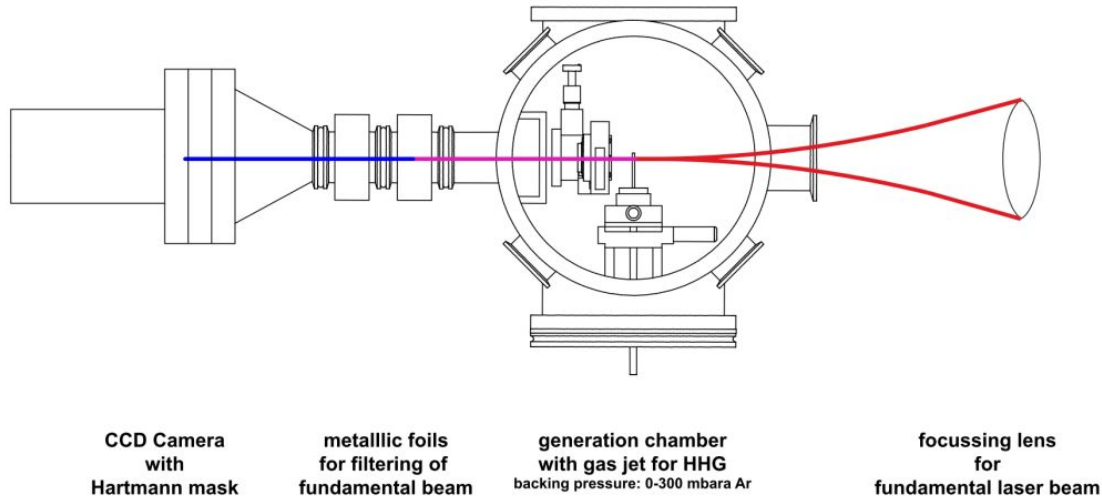


Figure 8.1: Experimental setup for measuring the wavefronts of high-order harmonics. The laser pulse is focused into the nickel tube by a fused silica lens ($f = 300$ mm, $f/\# = 15$). For spectral filtering a thin aluminum foil (thickness $0.2 \mu\text{m}$) is used. The X-ray CCD with the Hartmann mask is installed directly behind the generation chamber.

setup for the wavefront measurements is shown in Figure 8.1. It consists mainly of the generation chamber, into which the laser is focused, and the Hartmann sensor which was installed directly behind the generation chamber. For spectral filtering a thin aluminum foil (thickness $0.2 \mu\text{m}$), placed between the generation chamber and the Hartmann sensor, was used.

Similar to [121], the Hartmann sensor is composed of a Hartmann mask which is placed at a distance of 50 mm in front of the Andor DO420-BN X-ray CCD. The Hartmann mask, shown in Figure 8.2, was custom-made by LUMERA LASER. It has an array of 50×50 holes, laser drilled into a molybdenum plate. Each hole has a diameter of $40 \mu\text{m}$. The holes are spaced $140 \mu\text{m}$ apart. Since it is necessary to illuminate at least four adjacent pixels on the detector to compute the centroid position of each spot precisely, the pixel size of the detector defines the lower limit for the hole size. In this case it was given by the pixel size of the X-ray CCD, which is $26 \times 26 \mu\text{m}^2$. Larger holes are not useful, as though they would increase the precision of the centroid positions, the total number of holes illuminated by the high-order harmonic beam (beam diameter $d = 1$ mm foot-to-foot) is more important for accurate reconstruction of the wavefront. Thus, the parameters of the hole array are the best compromise for the given setup.

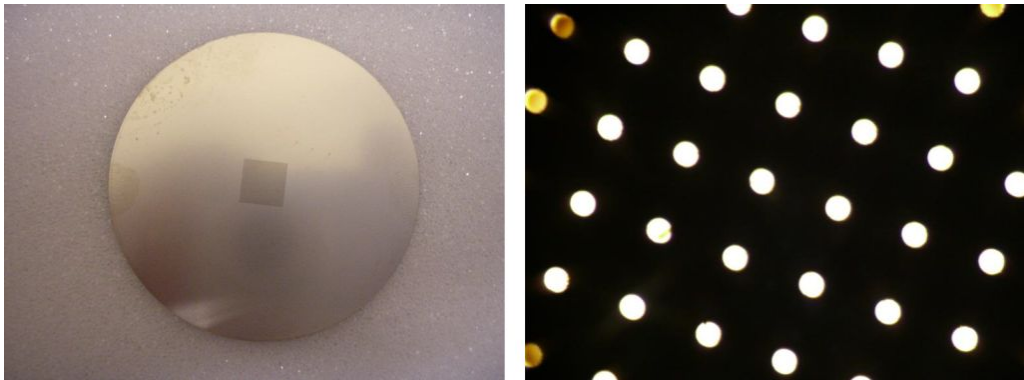


Figure 8.2: The Hartmann mask was custom-made by LUMERA LASER. It has an array of 50×50 holes, laser drilled into a molybdenum plate. Each hole has a diameter of $40 \mu\text{m}$. The holes are spaced $140 \mu\text{m}$ apart.

The Hartmann sensor was calibrated using the expanded beam of an He-Ne laser. A flat wavefront across the whole Hartmann mask could be ensured this way. Because the hole diameter of the mask was not designed to be used with a He-Ne laser each hole exhibited strong diffraction patterns. This greatly reduced the intensity of the laser beam which reached the detector. Nevertheless it was possible to evaluate the centroid of the image of each hole. This way a reference pattern could be defined.

8.2 The measurement

The wavefront measurements were done using laser pulses with a pulse energy of $500 \mu\text{J}$ and a pulse duration of about 40 fs . For focusing, a fused silica lens ($f = 300 \text{ mm}$, $f/\# = 15$), mounted on a translation stage, was used. Thus, the focal position inside the vacuum chamber could be changed along the propagation axis. In the following, this is called z -position with positive z values meaning a focal position in front of the nickel tube and $z = 0 \text{ mm}$ meaning the focal spot is at the position of the nickel tube. Due to self-focusing of the laser beam in air, it is hard to set this up exactly for vacuum conditions. Additionally, there is no easy way to determine the exact focal position during the experiment and the z -position in these measurements is only a rough estimate given with the naked eye.

The laser pulses were focused into a nickel tube with an inner diameter of about 2 mm . The holes created in the nickel tube had a diameter of $40 \mu\text{m}$ to $60 \mu\text{m}$. Thus, a peak intensity in the region of about $2 \times 10^{15} \text{ W/cm}^2$ was achieved.

After the drilling of the holes, the nickel tube was filled with argon gas as interaction medium. Because of the small holes, the gas-filled region was limited to the vicinity of the tube and the interaction length between the laser and the gas was about 2 mm . The backing pressure of the argon gas was adjustable between 0 mbar and

300 mbar. The pressure was controlled by an electronic valve with an accuracy of $\pm 1\%$ of the selected value. This led to a background pressure in the generation chamber ranging from 5×10^{-3} mbar to 8×10^{-2} mbar.

Because of small pointing instabilities of the laser, the hole diameter increased during the measurements. These instabilities did not affect the high-order harmonic generation directly. Due to the larger holes, the background pressure in the chamber increased. At background pressures higher than 0.1 mbar, reabsorption in both the interaction medium and the chamber became significant and reduced the measured signal to very low levels preventing the extraction of meaningful data. The gas pressure at the end of the measurement was limited to approximately 200 mbar by this effect.

Prior to the wavefront measurements, the spectrum of high-order harmonics generated with comparable laser pulse parameters, was recorded. A typical spectrum is shown in Figure 8.3. Experience from previous experiments shows that the overall

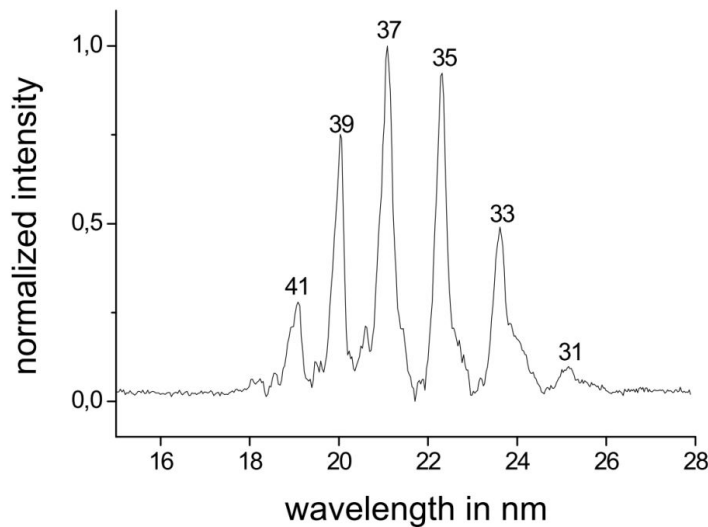


Figure 8.3: Typical high-order harmonic spectrum with a gas pressure of about 100 mbar argon gas and pulse energies of $500 \mu\text{J}$ at a pulse duration of 40 fs, detected behind an aluminum filter.

shape of the harmonics, i.e., the number and relative intensities of the harmonics, does not change much in the pressure range and z -position range used for the wavefront measurements. It can be safely assumed, that the spectrum of the detected high-order harmonic beam is more or less the same and only the beam profile and the photon flux change.

After the spectrum was recorded, the Hartmann setup was used for the wavefront measurements. An example of a measured Hartmann signal is shown in Figure 8.4. It was obtained using an exposure time of 1 s. All data was recorded using

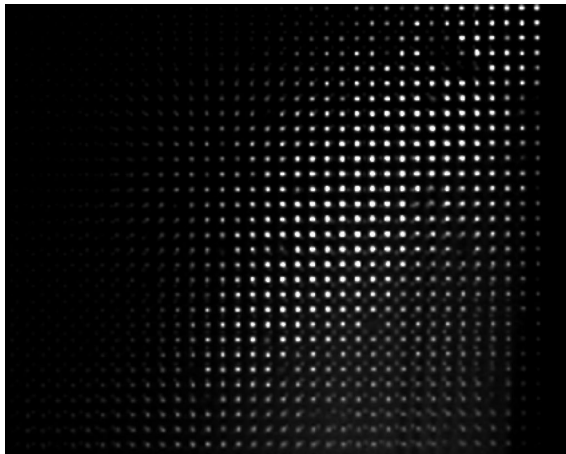


Figure 8.4: Example of a wavefront measurement with high-order harmonics. For some holes the transmission is reduced due to dust remaining inside the hole. From this image the wavefront and the beam profile of the high-order harmonics can be reconstructed.

the same exposure time and the data represents an average over approximately 1000 pulses. Changing the exposure time slightly had no significant effect on the evaluated wavefronts. Thus, it is safe to assume that the wavefronts do not change much over consecutive pulses.

In a first experiment, the measurement and evaluation of the wavefront of high-order harmonics could be demonstrated successfully. Additionally, the influence of the gas pressure and the z -position on the wavefront was studied. In a first step, the counts detected by the camera were optimized. This was done for gas pressure and z -position.

After the optimal configuration was found, the influence of the gas pressure was investigated first. This was done by scanning over the whole pressure range at a fixed focal position of $z = 1.5$ mm. In the next step, the z -position at a fixed gas pressure of 120 mbar was scanned, by moving the focus in front of the nickel tube.

As a last step, a spatial light modulator was used to modify the wavefront of the fundamental laser beam prior to focusing. For this spatial shaping the Hamamatsu X8267 PPM-SLM was used, as it was still present in the beam line from the experiments described in Chapter 7. The wavefronts which were imprinted onto the beam were parameterized using Zernike polynomials and included tilt, divergence, astigmatism, trefoil and comatic aberration. With the Hartmann mask in place the beam profile and wavefront of the high-order harmonics generated by the spatially shaped laser beam were investigated.

8.3 Experimental results

The evaluation of the recorded Hartmann spot patterns was done using the software described in [21, 22]. The evaluated wavefronts were characterized using Zernike polynomials (see Chapter 2 and Appendix B). It was observed that the reconstructed higher-order Zernike coefficients were not reliable due to experimental noise and only lower order polynomials such as divergence (Z_4), astigmatism (Z_3, Z_5) and partly trefoil (Z_6, Z_9) and comatic aberrations (Z_7, Z_8) were considered in the experimental results.

8.3.1 Results of the pressure scan

The generation of high-order harmonics is a coherent macroscopic build-up from a microscopic effect (see Chapter 5). As such, the number of generated photons scales quadratically with the number of atoms, i.e., with the pressure in the interaction region [122]. Another aspect is the pressure dependence of the reabsorption in the medium and of the phase-matching, as described in Section 5.2. All these contributions lead to the fact that the generation of high-order harmonics has a strong pressure dependence. Additionally, it is easily understood that the beam profile and the wavefront of the fundamental laser beam also influence phase-matching. Therefore, not only the number of generated photons is pressure dependent, but also the profile of the generated XUV beam [123].

In order to quantify the intensity of the high-order harmonic beam, the counts from the camera were evaluated. Note that in the following the term “intensity” is used somewhat sloppy as a measure for the number of detected photons and is not the actual physical quantity measured in units of W/cm^2 . Additionally, the wavefronts were reconstructed to evaluate the divergence and the astigmatism of the beam.

The results of the intensity and divergence evaluation is shown in Figure 8.5. Here, the red curve represents the number of counts which were integrated over the full CCD chip. The black curve was obtained by evaluating the number of counts of the brightest pixel of the measured image. This pixel is usually near the optical axis and can serve as a fairly good indicator of the peak intensity. Additionally, the Zernike coefficient for divergence (c_4) is shown as a blue curve.

At low pressures almost no high-order harmonics are generated. Up to pressures of about 100 mbar the intensity increases roughly quadratic. This is an indicator for a coherent build-up, as explained above. At pressures between 110 mbar to 120 mbar both the peak intensity and the integrated intensity reach a maximum. At even higher pressures the XUV signal decreases again. A study of the divergence coefficient shows a corresponding behavior. At pressures where the signal has its maximum, the divergence is smallest. As a result, the brilliance has its maximum at a pressure of about 120 mbar. There, the number of photons is highest and the solid angle is lowest.

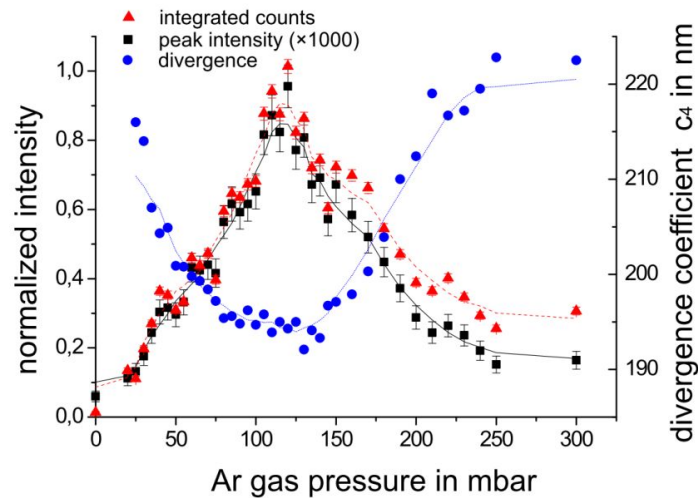


Figure 8.5: The peak intensity (black squares, solid line) and integrated intensity (red triangles, dashed line) versus gas pressure at $z = 1.5$ mm. The divergence (blue circles, dotted line) has its minimum in the same pressure range where the intensity peaks (110 mbar-130 mbar). Note that the lines should serve just as a guide and do not correspond to a model.

In order to ensure a good focusability of the high-order harmonic beam in the experimental chamber, it is important to know the astigmatism. This way, it might be possible to compensate for it. As the astigmatism can easily be retrieved from the wavefront-measurements, the influence of the gas pressure on astigmatism was studied. In Figure 8.6 both parts of the astigmatism are plotted against the pressure. For a description of these two parts see Section B.3.2. The pressure dependence of the 45° -astigmatism is given by the black curve. The red curve shows the dependence for the 90° -astigmatism. The different behavior of both parts reveals some interesting results.

The 45° -astigmatism varies only very little with gas pressure. The variation can be fitted quite well by a quadratic function. Compared to the 90° -astigmatism, however, it is nearly constant. The 90° -astigmatism shows quite a strong dependence on gas pressure. Interestingly this contribution to the astigmatism has its minimum at the same gas pressure where the intensity is highest.

8.3.2 Results of the variation of the focal position

As stated in Section 5.2.3, the geometric effects influence the phase-matching conditions of high-order harmonics. It can be easily understood that the position of the focus relative to the gas jet influences the generation of high-order harmonics.

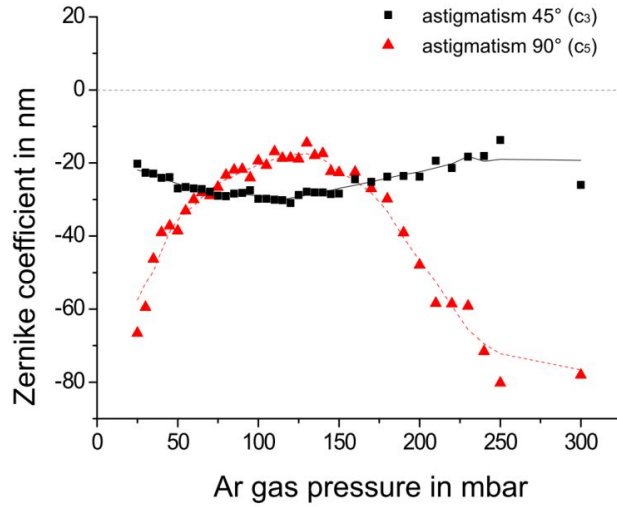


Figure 8.6: Comparison of the two contributions to astigmatism. The 45°-astigmatism (black squares, solid line) and the 90°-astigmatism (red triangles, dashed line). While the 45°-part remains nearly unchanged, the 90°-part has its minimum in the same pressure regime as the intensity (see Figure 8.5). Again, the lines do not correspond to a model and serve just as a guide.

It was even shown that it is possible to suppress the contribution of the long or short quantum path to the generation process by carefully choosing the position [124].

For easier comparison with the pressure scan, the same observables were used for the z -scan. It has to be noted, that compared to the pressure scan, much less data points are available for the z -scan. This is due to the fact that even with careful alignment the change of the z -position of the focal spot always slightly changed the x - and y -position as well. Due to these small instabilities, the holes in the nickel tube grew larger and the background pressure in the chamber increased with each change of z -position. Thus, the number of z -positions over which the effect was small enough to allow for comparison between two data points was limited. Changing the nickel tube during the experiment was not an option, because this would have changed the properties of the high-order harmonic generation.

In Figure 8.7 the integrated intensity, the peak intensity and the divergence are plotted against the z -position. Again, the red curve represents integrated intensity, the black curve the peak intensity and the blue curve the divergence. When comparing these results with the pressure scan, some similarities can be observed.

In the accessible region, integrated intensity and peak intensity behave pretty much

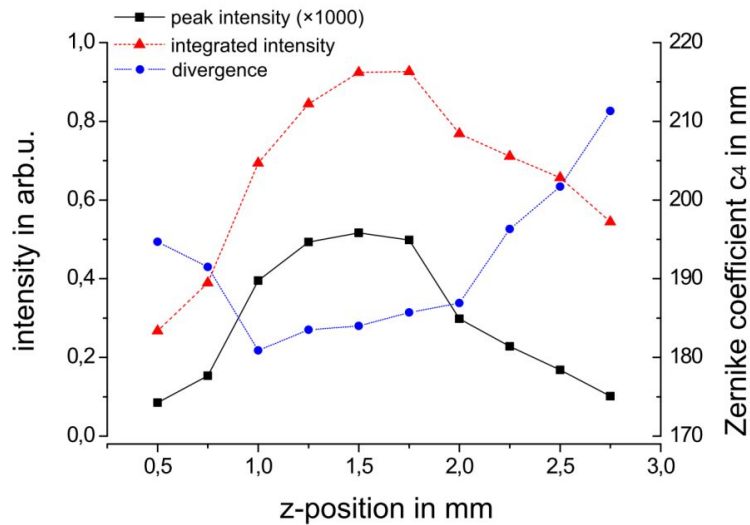


Figure 8.7: Plot of the peak intensity (black squares, solid line) and integrated intensity (red triangles, dashed line) versus z -position (at $z = 0$ mm the focus lies in the middle of the gas medium, positive z values mean the focus is in front of the nickel tube). The blue dotted graph (circles) again gives the divergence of the beam during the position scan. Similar to Figure 8.5 the divergence is lowest when the intensity of the XUV radiation is high.

the same. Only the order of magnitude of the signal differs. Again, a pronounced maximum can be found which occurs at $z = 1.5$ mm. In contrast to the pressure scan, the minimum of the divergence (around $z = 1.0$ mm) is not at the maximum of the intensity. It has to be noted that in the vicinity of the highest intensity, the divergence does not change dramatically. For regions near the gas jet and far away from it, the divergence grows while the intensity decreases. This behavior is in good agreement with [123].

Similar as for the pressure scan, the astigmatism was studied. The variation of astigmatism with z -position is shown in Figure 8.8. Between $z = 1.0$ mm and $z = 2.0$ mm the 90° -astigmatism is more or less not present. When moving closer to the gas jet or further away from it, the 90° -astigmatism becomes significant. The behavior of the 45° -astigmatism is more complex. It shows a nearly linear behavior. Around $z = 2.0$ mm the 45° -astigmatism vanishes when it changes its sign. When looking at the overall astigmatism, a minimum can be observed around $z = 2.0$ mm.

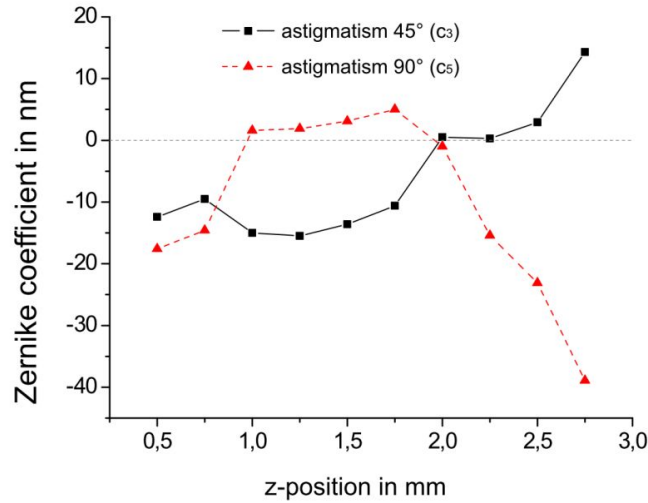


Figure 8.8: The two components of astigmatism (45°-astigmatism: black squares, solid line; 90°-astigmatism: red triangles, dashed line) are plotted versus focal position change. Both components change slightly with the focal position. Near the focal position for maximum intensity (compare Figure 8.7) the astigmatism clearly shows a plateau where the aberrations remain constant.

8.3.3 Phase masks

The results show that it is possible to generate high-order harmonics with quite a good beam quality. As the wavefront of the driving laser beam shows some minor aberrations, quantified as $\mathcal{M}^2 \approx 1.2$ [26, 108], the question arises whether the wavefront of the driving laser beam gets transferred onto the high-order harmonic beam, as suggested by [120]. This influence was studied systematically.

The wavefront of the fundamental laser beam was modified using phase masks, parameterized by Zernike polynomials. The phase masks were applied to the fundamental laser beam prior to focusing, using the Hamamatsu X8267 PPM-SLM. The modulation depth of the phase masks were adjustable to change the strength of the aberrations. For very strong aberrations the signal from the high-order harmonics decreased considerably. In some cases, however, the signal increased. This can be explained by the changed intensity in the interaction region. For the signal increase, the applied phase mask perhaps compensates some aberrations already present in the fundamental beam.

In order to systematically investigate the influence of the wavefront of the fundamental beam, different aberrations were applied. Afterwards the wavefront of the generated high-order harmonics was evaluated and compared with the applied phase

mask. Doing this, no clear correlation between the wavefront of the fundamental laser beam and the wavefront of the high-order harmonics could be found. In many cases, when using simple lower-order aberrations as phase mask, many different higher-order wavefront aberrations could be observed. Thus, no evidence for the direct transfer of the wavefront from the laser beam onto the beam of the high-order harmonics could be found. A nontrivial connection between the two wavefronts might still be possible.

8.3.4 The beam parameters of the high-order harmonic source

In order to quantify the quality of high-order harmonics as XUV source, the beam and propagation parameters of the high-order harmonic beam were calculated. As mentioned in Appendix A and Appendix B, this was done using the defocus coefficient c_4 and second-order beam moments obtained from a Hartmann measurement taken at optimal values for pressure and z -position.

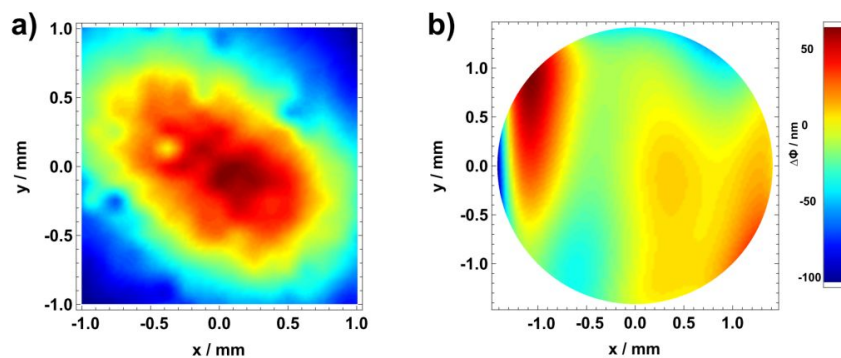


Figure 8.9: a) Beam profile and b) wave aberration of a high-order harmonic beam. High-order harmonics generated in Ar gas at optimal pressure of 120 mbar.

In Figure 8.9a) the spatial beam profile is shown. Figure 8.9b) shows the wave aberration which is in fact the reconstructed wavefront without the terms for piston, tilt and defocus. From the beam profile, the wave aberration and the defocus coefficient, the beam and propagation parameters were calculated. The high-order harmonic beam has a Rayleigh length of $z_R = 12.5 \pm 2.0$ mm. Taking the whole beam profile into account as described in Appendix A, the beam exhibits an effective beam propagation factor of

$$\mathcal{M}_{\text{eff}}^2 = 5 \pm 1.$$

This result is comparable to [125].

With the help of these parameters, the peak brilliance of the high-order harmonic beam was estimated to

$$B_{\text{peak}} = 2 \times 10^{18} \frac{\text{photons}}{\text{s sr mm}^2 0.1\% \text{BW}}.$$

8.4 Conclusion

It could be demonstrated that it is possible to measure the wavefront of XUV radiation with a simple Hartmann mask. From this simple measurement the beam and propagation parameters of the high-order harmonic beam could be retrieved. Additionally, the influence of the gas pressure and the position of the focus relative to the gas jet on the wavefront of high-order harmonics were studied.

It could be demonstrated that the best beam quality and lowest divergence coincide with the highest photon flux. Additionally it was shown that the wavefront of the fundamental laser beam is not transferred directly onto the wavefront of the high-order harmonics. Hence, by adjusting the gas pressure and focal position to maximize the detected signal, the optimal brilliance of the source is achieved.

Chapter 9

High-order harmonic generation with wavefront controlled laser pulses

The experiments described earlier and in previous works [120, 126, 127] suggest that the wavefront of the fundamental laser beam has a significant influence on the process of high-order harmonic generation. In Chapter 8 the wavefront of the high-order harmonics was measured. In addition to the wavefront measurements experiments were conducted to see if the wavefront of the driving laser beam gets transferred onto the high-order harmonic beam. The results of these experiments, described in Section 8.3.3, show no direct transfer of the wavefront. There are some indications, however, that some effects depend on the wavefront. During these experiments a non-ideal fundamental laser beam sometimes resulted in an increased high-order harmonic yield. In order to better understand the process, attempts were made to evaluate this influence of the wavefront.

As a first experiment, it was examined if a beam with a non-flat wavefront is able to generate more high-order harmonics than an undistorted laser pulse. This was done using a closed-loop optimization scheme based on a genetic algorithm. In subsequent experiments the influence of the optimization on the beam profile of the fundamental laser beam was evaluated.

These experiments were conducted after the equipment was moved to the new laboratory at the Institute for Optics and Quantum-electronics of the Friedrich-Schiller-University of Jena.

9.1 Experimental setup

Due to the move to the new laboratory, some of the components of the experimental setup, described in Chapter 6, were replaced. In Figure 9.1 the setup used for the experiments described in this Chapter is shown.

The laser pulses from the amplifier system are spatially shaped by the SLM. As mentioned in Chapter 6, the Hamamatsu PPM-SLM X8267 is replaced by the LCOS-SLM X10468-02. As both SLMs are very similar, only minor modifications to the genetic algorithm were necessary.

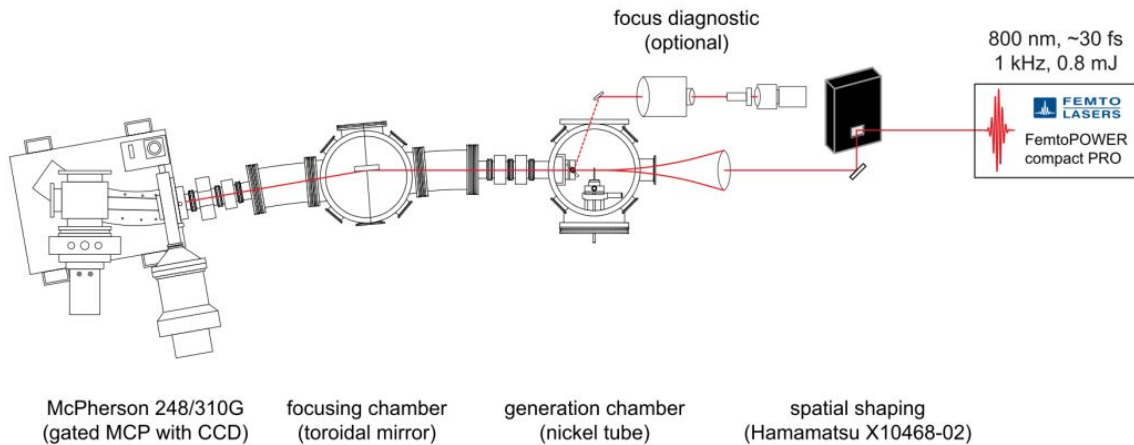


Figure 9.1: Setup for high-order harmonic generation with wavefront controlled laser pulses. The laser beam from the FemtoPOWER amplifier system is spatially shaped before it is focused into the generation chamber. The generated high-order harmonics are focused onto a McPherson 248/310G spectrometer where they are analyzed. In order to measure the beam profile of the fundamental laser beam near the focus, a long-working-distance microscope is available. The use of the focus diagnostic is optional.

The shaped beam is afterwards used to generate high-order harmonics. The generation takes place in a gas-filled nickel tube, as described in Chapter 6. The nickel tube is located inside the generation chamber. As interaction medium the noble gases argon and neon are used at varying pressures.

In order to increase the available intensity of the high-order harmonics, a toroidal mirror is used to focus the generated radiation onto the entrance slit of an XUV spectrometer. In order to filter out the remaining fundamental light from the high-order harmonic beam, thin metallic foils are used. Two different sets of foils are available during the experiments. An aluminum foil with a thickness of 200 nm is used to detect high-order harmonics in the wavelength range between 17 nm and 50 nm. For higher-order harmonics in the wavelength range between 10 nm and 20 nm, a 200 nm thick zirconium foil, supported by a mesh layer, is used. In Figure 9.2 the transmission curves of the aluminum filter (red curve) and the zirconium filter (black curve) for the XUV range are shown. The data to plot these curves is taken from [128].

The XUV spectrometer is another component which has changed compared to the setup used in Wuerzburg. The custom made spectrometer is replaced by a commercially available McPherson 248/310G spectrometer. The McPherson 248/310G spectrometer is discussed in more detail in Appendix D and in [129].

In order to evaluate the influence of the spatial shaping on the fundamental laser beam, a long-working-distance microscope was built. A pickup mirror can be moved in and out of the beam inside the vacuum directly behind the nickel tube. This way,

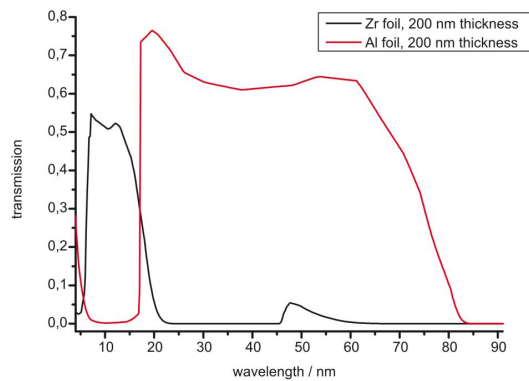


Figure 9.2: XUV transmission of the thin metallic foils used as filter. Transmission curve (red) of aluminum (thickness 200 nm). Transmission curve (black) of zirconium (thickness 200 nm). Data taken from [128].

the usage of the microscope which is placed outside the vacuum chamber is optional. A similar setup was already used to study water microdroplets as interaction medium for high-order harmonic generation [130]. The remote microscope employs a standard SLR camera objective with a focal length of $f = 200$ mm. The objective creates a real intermediate image of the interaction region at its backplane. The magnification of this intermediate image is slightly less than 1. The SLR objective was chosen because of its wide aperture and its very good imaging properties. In order to examine the beam profile at the beam waist a standard $20\times$ microscope objective is used as ocular lens. A near-infrared sensitive CCD camera (DALSA Genie M1024) serves as detector. The resolution of this microscope is about $5\ \mu\text{m}$.

9.2 The measurement

As a first step, the high-order harmonic generation was done using argon gas as interaction medium. The position of the focusing lens and the gas pressure were adjusted as already described in Chapter 8. It was found that the lens position and the gas pressure were nearly the same as in Chapter 8.

After the setup was manually adjusted for best high-order harmonic yield, several optimizations with the genetic algorithm were carried out. This was done in order to adjust the free experimental parameters of the genetic algorithm, such as mutation probability or mutation deviation mentioned in Appendix C. Similar to Villoresi et al. [127] and Yoshitomi et al. [126], the genetic algorithm was modified to influence the wavefront of the fundamental laser beam. In order to allow for a direct evaluation of the applied wavefront, the algorithm used Zernike polynomials. The Hamamatsu LCOS-SLM used in this work has a much higher resolution compared to the deformable mirrors used by Villoresi et al. and Yoshitomi et al..

Additionally, the SLM is capable of greater modulation depths. This way, the influence of strong higher-order wavefront aberrations can be studied. During this work Zernike polynomials up to the 6th radial order were used. The corresponding Zernike polynomials are shown in Table B.1 in Appendix B.

After the genetic algorithm was tested the experiments were carried out. As a first experiment the overall harmonic yield was optimized. This was done using argon gas at a backing pressure of 120 mbar. Several optimization runs were carried out.

In the next step the interaction medium was changed from argon to neon. The backing pressure of the neon gas was increased to 300 mbar to compensate for the lower ionization rate of neon compared to argon due to its higher ionization potential [131]. Generation of high-order harmonics in neon proved to be more difficult. Even with careful adjustment no harmonics could be detected. When using the optimized phase mask, found during the optimization with argon, together with neon as interaction medium, however, high-order harmonics were generated. With this phase mask as initial generation, further optimizations in neon were carried out.

In order to study the wavefront of the optimized laser beam, a commercial Shack-Hartmann was used. The Shack-Hartmann sensor was placed behind the focusing lens to directly evaluate the wavefront which influences the generation of high-order harmonics. This evaluation was done with the reference beam and a beam which was optimized for the generation of high-order harmonics in argon.

From the wavefront measurements the beam profile in the focus was calculated. The spatial resolution of this calculation is limited, however. This limit is given by the resolution of the Shack-Hartmann sensor. In order to determine how the optimized wavefront modifies the intensity distribution, the beam profile in the interaction region was measured directly. This was done using the long-working-distance microscope described above. As the laser had to be realigned between the Shack-Hartmann measurement and the beam profile measurement, the beam properties changed slightly between these conditions. Thus, the results of both measurements can only be compared with caution. Furthermore, the wavefront measurement could not be repeated during the beam profile measurements as the Shack-Hartmann sensor was no longer available.

9.3 Experimental results

In a first step the free parameters of the genetic algorithm were adapted to the experiment. The free parameters control the properties of the “reproduction ” operations described in Appendix C. During the initial experiments experience with the new setup was gained. With the free parameters given in Table 9.1 the genetic algorithm produced quite stable results. Additionally, the time needed for one optimization run could be decreased. This speed increase, however, led to an increased memory

parents ratio	clone content	cross-over content	mutation probability	mutation deviation
0.3	0.2	0.4	0.4	35

Table 9.1: The free parameters of the genetic algorithm and their respective values, as used for the optimization experiments. For a description of the free parameters see Appendix C.

usage. Due to the high memory requirements only optimizations with about 100 generations were possible. Typically, the optimizations converged within 50 generations. Thus, the limited generation size posed no problem. With these results further wavefront optimizations were conducted.

9.3.1 Optimization of high-order harmonic generation

In a first step the yield of high-order harmonic radiation generated in argon gas was optimized. In Figure 9.3 the evolution of the fitness during the optimization is shown. In total, four different types of fitness value which are characteristic for genetic algorithms are displayed.

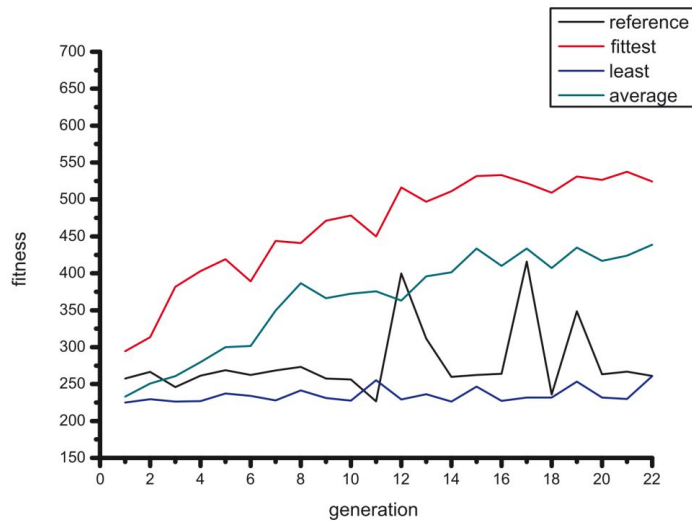


Figure 9.3: Evolution of the fitness during an optimization. The fitness function was defined such as to increase the overall high-order harmonic yield. As an interaction medium, argon gas at a pressure of 120 mbar was used.

At the beginning of each generation cycle the fitness of a beam with a flat wavefront applied is recorded. This reference, shown as black curve, is used to monitor the long term stability of the laser. With its help the data can be corrected for slow drifts of the laser parameters. The red curve shows the fitness of the best individual

and the blue curve shows the least fittest individual. Together these two determine the range of the fitness which is supported by current gene pool. Another important information is the average fitness of the generation shown as green-blue curve. It can be used to measure the overall fitness of the gene pool. It also serves as an indicator for the diversity which is described in Appendix C.

The evolution of the fitness clearly shows a significant increase over the course of optimization. Both the average fitness (green-blue) and the fitness of the best individual (red) increase steadily. The fitness of the worst individual (blue), however, remains more or less constant. This can be explained by the fact that all generations contain individuals which do not generate any high-order harmonics at all and the fitness value contains only detector noise of the spectrometer. The reference curve (black) shows some strong peaks between generations 11 and 18. These peaks are probably caused by random laser fluctuations. In order to rule out that these fluctuations prevented the algorithm from finding an optimal wavefront, all individuals of these generations were examined. Especially the fitness values of the cloned individuals between two generations were compared. The clones had very similar values between two generations. Thus it is safe to assume that the fluctuations did not disturb the genetic algorithm significantly.

In Figure 9.4 the resulting spectra of the reference (black curve) and the fittest individual (red curve) at the end of the optimization are shown. These spectra were

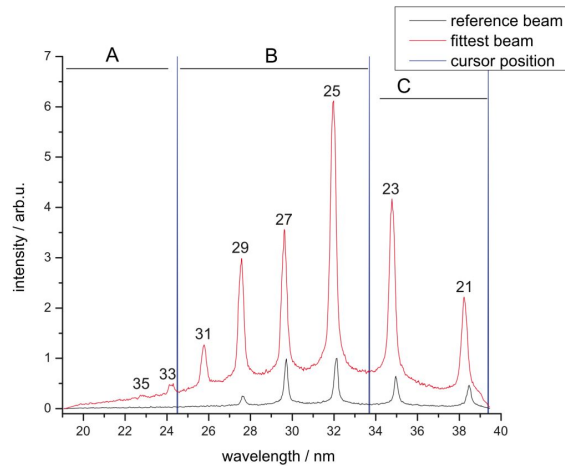


Figure 9.4: The high-order harmonic spectrum before (black curve) and after (red curve) optimization. The optimization goal was set to increase the overall high-order harmonic yield in the regions *B* and *C*. The order of each harmonic is shown on top of the harmonic line. The spectra are rescaled for a better readability while preserving the relative intensities.

also used to calculate the fitness. Three spectral regions, called *A*, *B* and *C* were defined. These three regions, marked by the blue cursors, are also shown. From

these, the fitness was calculated using the fitness function

$$F = \frac{B + C}{1000}. \quad (9.1)$$

The spectra clearly show a significant increase of the high-order harmonic yield. The 25th harmonic, for example, increased by a factor of about 6. In the cut-off region three additional lines (31st - 35th harmonic) can be seen in the optimized spectrum. The additional lines indicate an intensity increase in the interaction region, whereas the increased yield in the plateau indicate phase-matching effects [126, 127]. Further studies were conducted in order to examine the influence of the wavefront on high-order harmonic generation more closely.

9.3.2 Beam profile of the optimized laser beam

As mentioned above, further experiments were carried out to see how the optimization influenced the generation process. In order to evaluate how the optimized wavefront modifies the intensity distribution of the fundamental laser beam, the beam profile in the interaction region was determined.

Shack-Hartmann wavefront measurement of the fundamental laser beam

In a first step the beam profile and the wavefront of the fundamental laser were measured behind the focusing lens. This was done for the reference beam and the optimized beam, using a commercial Shack-Hartmann sensor. From the beam profile and the wavefront the intensity distribution at any point along the propagation axis can be calculated. As described in Section 2.4.2, this calculation is done by numerically solving the Fresnel integral given by Equation (2.22).

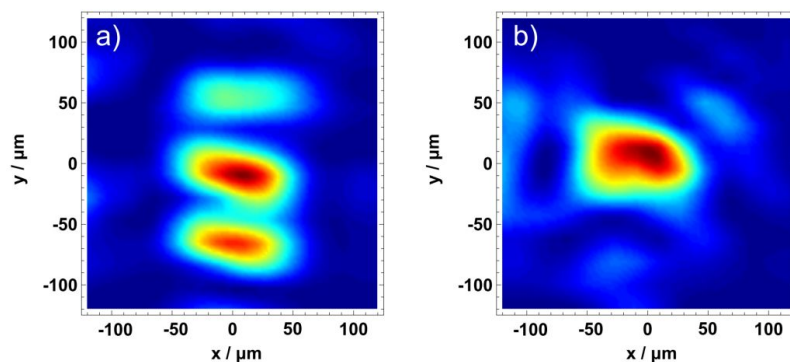


Figure 9.5: Calculated beam profile near the interaction region. Calculations for a) the reference beam and b) the optimized beam were done with data acquired by a Shack-Hartmann measurement. The spatial resolution of these calculations is about 20 μm.

In Figure 9.5a) the calculated beam profile of the reference beam is shown. The beam profile shows strong disturbances above and below the “actual” beam center. These disturbances are artifacts from the calculations. They are caused by interference fringes visible in the beam profiles retrieved from the Shack-Hartmann measurement. These interferences are caused by neutral density filters. The filters are used to attenuate the beam to avoid damage of the Shack-Hartmann sensor. As can be seen from the calculated beam profile, the actual reference beam in the center of the image is quite elongated which is caused by astigmatism present in the wavefront.

When comparing the beam profile of the optimized beam, shown in Figure 9.5b), to the beam profile of the reference beam, a larger beam diameter is apparent. This larger beam diameter indicates that the increased high-order harmonic yield, described above, is in fact not caused by an intensity increase but originates from other effects.

Direct measurement of the beam profile near the interaction region

In a second step the beam profile near the interaction region was recorded directly. This was done to confirm if the calculations of the beam profiles discussed above are correct. In order to directly measure the beam profile, the long-working-distance microscope mentioned earlier was used.

Between the Shack-Hartmann measurement and these experiments the laser system and the setup were realigned. This led to a beam which displayed less aberrations in the unshaped beam. Therefore, caution is needed when comparing the results of both measurements.

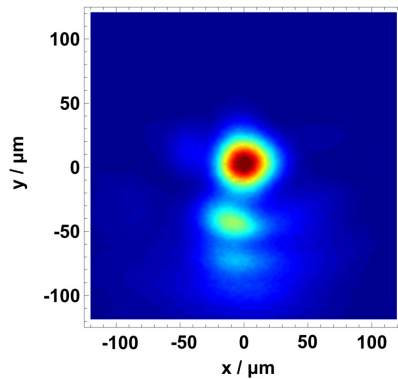


Figure 9.6: Beam profile of the reference beam at full intensity with argon gas (120 mbar backing pressure) as interaction medium. The spatial resolution of the beam profile measurement is about $5 \mu\text{m}$.

The beam profile of the reference beam is shown in Figure 9.6. As can be seen, the beam profile is nearly Gaussian and has a diameter of about $43 \mu\text{m}$. Below the actual beam profile small disturbances are visible. These disturbances are caused by

multiple reflections at two neutral density filters. These filters were placed directly in front of the microscope and were used to attenuate the beam.

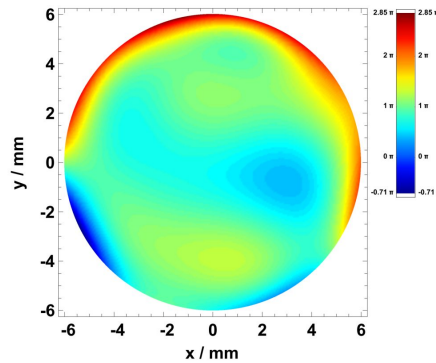


Figure 9.7: Phase-mask applied to the SLM to create the optimized laser beam. The phase-mask is dominated by large Zernike coefficients for trefoil, coma and astigmatism. In order to increase the modulation depth beyond 2π a phase wrapping technique with sharp phase jumps of 2π was used before the phase-mask was applied to the SLM.

The same measurement was also done for an optimized beam. The optimization was carried out with the same parameters used for the optimization preceding the Shack-Hartmann measurement. From the phase-mask applied to the SLM the intensity distribution near the focus was calculated. For this, the phase-mask, shown in Figure 9.7, was used as wavefront of the incident beam. Again, this was done by numerically calculating the Fresnel integral given by Equation (2.22). This way, the beam profiles of the optimized beam at different experimental conditions can be compared.

In Figure 9.8 the calculated and the measured beam profiles are compared. Figure 9.8a) shows the calculated beam profile. As can be seen, the beam profile in the interaction region is slightly distorted. The beam diameter along the longer main axis is about $46\ \mu\text{m}$. The resolution achieved by the calculation is about $10\ \mu\text{m}$ and is limited by the available computational power and the limited resolution of the SLM.

In Figure 9.8b) a measured beam profile is shown. This beam profile was recorded using an attenuated beam with an optimized wavefront. Additionally, no gas was present in the interaction region. This allows for a comparison of the measured data with the calculation. The calculated beam diameter of about $46\ \mu\text{m}$ is in good agreement with the measured beam diameter of about $48\ \mu\text{m}$. Similar to Figure 9.6, small disturbances appear below and on the left side of the actual beam profile. Again, these disturbances are caused by multiple reflections at two neutral density filters. This time, the filters were placed in front of the focusing lens. Thus, the intensity at the interaction region was very low and no nonlinear effects occurred.

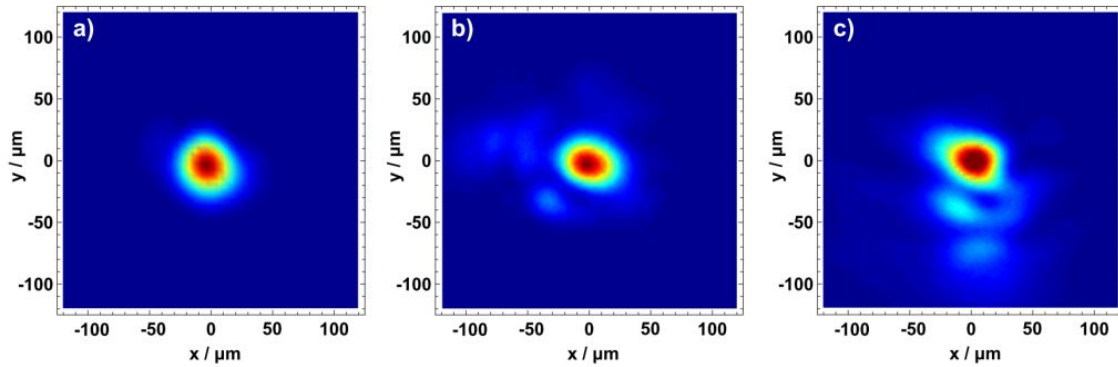


Figure 9.8: a) Beam profile of the optimized beam calculated from the SLM phase-mask assuming a Gaussian beam profile. The spatial resolution of the calculation is $10\ \mu\text{m}$. b) Beam profile of the optimized beam at low intensity (attenuation: 10^{-9} in front of focusing lens) with no interaction medium present. c) Beam profile of the optimized beam at full intensity with argon gas (120 mbar backing pressure) as interaction medium. The spatial resolution of the beam profile measurement is about $5\ \mu\text{m}$.

Figure 9.8c) shows the beam profile measured under the same experimental conditions which were used for the optimization. Under these conditions the beam diameter of about $53\ \mu\text{m}$ is slightly larger than the beam diameter at low intensities without interaction medium. Similar to Figure 9.6, attenuation of the beam occurred directly in front of the microscope using the same two neutral density filters. This way, all nonlinear effects in the interaction medium which might affect the beam profile were present.

When comparing the different beam profiles, several interesting characteristics can be noticed. The comparison of Figure 9.8a) and Figure 9.8b) shows that the beam profile at the interaction region is influenced mainly by the phase mask applied to the SLM. The calculated and the measured beam diameter agree very well. By comparing Figure 9.8b) and Figure 9.8c) the influence of nonlinear effects in the interaction medium on the beam profile can be detected. As can be seen, the nonlinear effects slightly reduce the asymmetry of the laser beam, but increase the beam diameter significantly. A comparison between Figure 9.8c) and Figure 9.6 clearly shows that the beam diameter of the beam optimized for an increased high-order harmonic yield is larger than the beam diameter of the reference beam. Additionally, the optimized beam profile has a pronounced asymmetry. Even though this optimized beam has a reduced peak intensity compared to the reference beam, the high-order harmonic yield from this beam is higher. This finding is in good agreement with [126, 127] and also confirms the results of the Shack-Hartmann measurement which show the same general behavior.

9.4 Conclusion

It has been shown that it is possible to increase the high-order harmonic yield by using wavefront-shaped laser beams. The investigation of the beam profile near the interaction region showed that the optimized beam has an asymmetric beam profile with a larger beam diameter. Thus, the optimized beam leads to a higher yield even when the peak intensity is lower compared to an unoptimized beam. This indicates that the wavefront and the beam profile of the fundamental laser beam play an important role in the efficient generation of high-order harmonic radiation.

In order to understand whether this influence is purely a phase-matching phenomenon or if other processes also play a role further studies are needed.

Chapter 10

Summary

In many experiments which are based on nonlinear optical effects, the phase of the driving laser pulse plays a crucial role. In this work, the influence of the spatial phase distribution, also called wavefront, on extremely nonlinear effects was studied. These nonlinear effects, namely filamentation of ultra-short laser pulses and high-order harmonic generation, cannot be easily described in terms of perturbation theory. Therefore, these extremely nonlinear optical processes need special theoretical models. An introduction to these models is given in order to better understand the physical background.

Filamentation of ultra-short laser pulses provides a tool to spectrally broaden the laser pulse. This spectral broadening is caused by self-phase modulation and can be used to further shorten the laser pulse. In earlier experiments a gas-filled hollow core fiber was used to achieve this broadening. In order to decide if filamentation can serve as a suitable replacement for hollow-core fibers, the properties of the laser beam after filamentation were investigated. These experiments showed that the laser beam exhibits some unwanted features after filamentation. In the next step, the wavefront of the fundamental laser beam was controlled prior to filamentation. This control was achieved by using a spatial light modulator. The spatial light modulator was combined with a genetic algorithm in order to adaptively optimize the filamentation process and to remove the unwanted features. It was shown that by removing the unwanted features, filamentation is a suitable tool to perform spectral broadening and can be used to replace a gas-filled hollow core fiber.

The second extremely nonlinear effect studied in this work is the process of high-order harmonic generation. This effect converts laser light into the extreme ultraviolet regime. The radiation generated this way shares many of the properties of the driving laser pulse and is thus a source of spatially and temporally coherent XUV radiation. A quantity which allows for easy comparison of different XUV sources is the brilliance or spectral brightness. It takes into account not only the photon flux, but also the size of the source and its emission characteristics. Much work has been done to optimize the spectral shape, the photon flux or the temporal properties of high-order harmonic radiation sources. Another approach to optimizing the

brilliance is the control of the wavefront of high-order harmonics. In order to examine how the brilliance of the source can be maximized, the wavefront of high-order harmonics was measured.

The wavefront measurement used a simple Hartmann mask combined with a back-illuminated X-ray CCD. The measured wavefronts were evaluated using Zernike polynomials. From these, the beam and propagation parameters of high-order harmonic beams could be retrieved. This way, the influence of external parameters, i.e., the gas pressure of the interaction medium and the position of the focus relative to the interaction medium, was studied. Additionally, it was examined if the wavefront of the fundamental laser beam gets transferred onto the high-order harmonic beam. In order to modify the wavefront of the driving laser beam, it was directly influenced using a spatial light modulator. Afterwards, the wavefront of high-order harmonics generated by such modified beams was measured. These studies revealed that no direct transfer of the fundamental wavefront onto the high-order harmonics takes place. Furthermore, it was shown that for high-order harmonic beams, the best beam quality and lowest divergence coincide with the highest photon flux. Thus, optimization of the high-order harmonic yield results in a beam with the best achievable brilliance.

Some results of this work as well as previous experiments suggest that the wavefront of the fundamental laser beam has a significant influence on the process of high-order harmonic generation. During experiments a non-ideal fundamental laser beam sometimes resulted in an increased high-order harmonic yield. In order to better understand the process, attempts were made to evaluate this influence of the wavefront. This was done using wavefront-controlled laser beams to generate high-order harmonics. The wavefront control used phase masks which were applied to the driving laser beam by a spatial light modulator. These phase mask were created using Zernike polynomials and were optimized by a genetic algorithm for increased high-order harmonic yield. From investigations of the beam profile near the interaction region it was shown that the optimized fundamental beam has an asymmetric beam profile with a larger beam diameter compared to the initial beam. Thus, optimization led to a higher yield even by decreasing the peak intensity of the driving laser pulse. This indicates that the wavefront and the beam profile of the fundamental laser beam play an important role in the efficient generation of high-order harmonic radiation.

Chapter 11

Zusammenfassung

Bei vielen Experimenten, die auf nichtlinearen, optischen Effekten basieren, spielt die Phase des erzeugenden Laserpulses eine tragende Rolle. In dieser Arbeit wird der Einfluss der räumlichen Phasenverteilung, auch Wellenfront genannt, auf extrem nichtlineare Effekte untersucht. Diese nichtlinearen Effekte, namentlich Filamentierung von ultrakurzen Laserpulsen und die Erzeugung von Hohen Harmonischen von Laserstrahlung, können nicht ohne weiteres mit Hilfe der Störungstheorie erklärt werden. Deshalb erfordern diese extrem nichtlinearen Effekte spezielle theoretische Modelle. Zum besseren Verständnis des physikalischen Hintergrunds werden diese Modelle kurz eingeführt.

Die Filamentierung von ultrakurzen Laserpulsen bietet ein einfach zu nutzendes Werkzeug, um Laserpulse spektral zu verbreitern. Diese spektrale Verbreiterung wird durch Selbstphasenmodulation in einem Medium hervorgerufen und kann dazu verwendet werden, Laserpulse zeitlich zu verkürzen. In früheren Experimenten wurde eine gasgefüllte Hohlleiter zur Verbreiterung verwendet. Um zu entscheiden, ob Filamentierung einen geeigneten Ersatz für die Verwendung von Hohlleitern darstellt, wurden deshalb zuerst die Strahleigenschaften des Lasers nach dem Filament vermessen. Diese Experimente zeigten einige unerwünschte Strahleigenschaften auf. Im nächsten Schritt wurde die Wellenfront des erzeugenden Laserstrahls vor dem Filament gesteuert. Diese Steuerung wurde mit Hilfe eines Raumlichtmodulators (engl. spatial light modulator) realisiert. Zur adaptiven Optimierung des Filamentierungsprozesses und zur Unterdrückung der unerwünschten Strahleigenschaften erfolgte die Ansteuerung des Raumlichtmodulators mit Hilfe eines genetischen Algorithmus. Auf diese Weise konnte gezeigt werden, dass Filamentierung durchaus ein geeignetes Werkzeug zur spektralen Verbreiterung von Laserpulsen ist und sich eignet, Hohlleitern zu ersetzen.

Der zweite nichtlineare Effekte der in dieser Arbeit untersucht wurde, ist die Hohe-Harmonischen Erzeugung. Dieser Effekt konvertiert Laserstrahlung vom nahinfraroten in den extrem ultravioletten (XUV) Bereich. Die auf diese Weise erzeugte XUV-Strahlung besitzt einige Eigenschaften des sie erzeugenden Laserpulses, und ist somit eine Quelle für räumlich und zeitlich kohärente XUV-Strahlung. Um verschiedene Strahlungsquellen im XUV Bereich zu vergleichen, wird häufig die Brillanz

verwendet. Die Brillanz beinhaltet hierbei nicht nur den Photonenfluss, sondern auch die Größe und Abstrahlcharakteristik der Quelle. Viele Arbeiten beschreiben die Optimierung von Hohen-Harmonischen Quellen in Bezug auf spektrale Verteilung, Photonenfluss oder den zeitlichen Verlauf. Ein weiterer Ansatz die Brillanz der Quelle zu optimieren ist die Steuerung der Wellenfront des Hohen-Harmonischen-Strahls. Um zu untersuchen wie die Brillanz der Quelle optimiert werden kann, wurde die Wellenfront des Hohen-Harmonischen-Strahls gemessen.

Die Wellenfront wurde mit Hilfe einer Kombination aus einer rückseitig-beleuchteten Röntgen-CCD-Kamera und einer einfachen Hartmann-Maske bestimmt. Die aufgenommenen Wellenfronten wurden anschließend mit Hilfe von Zernike-Polynomen quantifiziert und ausgewertet. Weiterhin konnten die Strahl- und Propagationsparameter des Hohen-Harmonischen-Strahls bestimmt werden. Auf diese Weise konnte der Einfluss externer Erzeugungsparameter wie Gasdruck des Erzeugungsmediums und die Position des Fokus relativ zum Erzeugungsgebiet untersucht werden. Zusätzlich wurde untersucht, ob die Wellenfront des erzeugenden Strahls auf den Hohen-Harmonischen-Strahl übertragen wird. Um die Wellenfront des Fundamentalstrahls zu steuern, wurde diese mit Hilfe eines Raumlichtmodulators verändert. Anschließend wurde die Wellenfront des Hohen-Harmonischen-Strahls untersucht, der mit solch einem veränderten Fundamentalstrahl erzeugt wurde. Diese Untersuchungen zeigten, dass kein direkter Transfer der Wellenfronten vom Fundamentalstrahl auf den Hohen-Harmonischen-Strahl stattfindet. Weiterhin konnte gezeigt werden, dass für Hohe-Harmonischen-Strahlen die beste Strahlqualität und die geringste Divergenz zusammen mit dem höchsten Photonenfluss auftritt. Daher führt eine Optimierung auf die beste Hohen-Harmonischen-Ausbeute automatisch zu einem Strahl mit höchster Brillanz.

Die Ergebnisse dieser Arbeit sowie frühere Experimente weisen auf einen deutlichen Einfluss der Wellenfront des fundamentalen Laserstrahls auf die Erzeugung von Hohen-Harmonischen hin. Bei einigen Experimenten zeigte sich, dass ein nicht-idealer fundamentaler Laserstrahl eine verbesserte Ausbeute an XUV-Strahlung zur Folge hatte. Um diesen Prozess besser zu verstehen, wurde der Einfluss der Wellenfront auf den Erzeugungsprozess näher untersucht. Diese Untersuchungen wurden mit Hilfe von Wellenfront-gesteuerten Laserpulsen zur Erzeugung von Hohen-Harmonischen durchgeführt. Die Steuerung der Wellenfront erfolgte durch Phasenmasken, die mittels eines Raumlichtmodulators auf den erzeugenden Laserstrahl aufgeprägt wurden. Diese Phasenmasken wurden mit Hilfe von Zernike-Polynomen konstruiert und durch einen genetischen Algorithmus so optimiert, dass sie die Ausbeute von XUV-Strahlung steigerten. Durch Untersuchungen des Strahlprofils des erzeugenden Strahls in der Nähe des Erzeugungsgebiets konnte gezeigt werden, dass der optimierte Fundamentalstrahl ein asymmetrisches Strahlprofil mit einem größeren Strahldurchmesser ausweist, als der ursprüngliche Strahl. Daher zeigt sich, dass die Ausbeute durch Optimierung verbessert werden kann, obwohl sich die Spitzenintensität des erzeugenden Laserpulses verringert. Dies weist auf den wichtigen Einfluss der Wellenfront und des Strahlprofils auf den Erzeugungsprozess hin.

Part III
Appendices

Appendix A

Derivation of beam parameters from second-order beam moments

In [6] it is shown that the first and second order beam moments serve as good quantities to determine beam parameters. Their special properties make them ideal for a wide area of applications. They are even used to define standard beam parameters [8, 9]. Some of the standard beam parameters and how they are derived from the first and second order beam moments are discussed in the following.

The second-order spatial moments $\langle x^2 \rangle$ and $\langle y^2 \rangle$ can be calculated from the beam profile by

$$\langle x^2 \rangle = \frac{\iint (x - \langle x \rangle)^2 I(x, y) dx dy}{\iint I(x, y) dx dy} \quad (\text{A.1})$$

and likewise for y as

$$\langle y^2 \rangle = \frac{\iint (y - \langle y \rangle)^2 I(x, y) dx dy}{\iint I(x, y) dx dy}. \quad (\text{A.2})$$

Here the integration is carried out over the whole beam. The first-order spatial moments $\langle x \rangle$ and $\langle y \rangle$ which are used are given by

$$\langle x \rangle = \frac{\iint x I(x, y) dx dy}{\iint I(x, y) dx dy}, \quad (\text{A.3a})$$

$$\langle y \rangle = \frac{\iint y I(x, y) dx dy}{\iint I(x, y) dx dy}. \quad (\text{A.3b})$$

The second-order spatial moments determine the beam widths (in x and y direction) which are given by

$$2w_{0,x} = d_x = 4\sqrt{\langle x^2 \rangle}, \quad (\text{A.4a})$$

$$2w_{0,y} = d_y = 4\sqrt{\langle y^2 \rangle}. \quad (\text{A.4b})$$

The second-order angular moments $\langle u_x^2 \rangle$ and $\langle u_y^2 \rangle$ are calculated with the help of

the local angular shift β . This leads to

$$\langle u_x^2 \rangle = \frac{\iint (\beta_x(x, y) - \langle u_x \rangle)^2 I(x, y) dx dy}{\iint I(x, y) dx dy}, \quad (\text{A.5a})$$

$$\langle u_y^2 \rangle = \frac{\iint (\beta_y(x, y) - \langle u_y \rangle)^2 I(x, y) dx dy}{\iint I(x, y) dx dy} \quad (\text{A.5b})$$

with the first-order angular moments

$$\langle u_x \rangle = \frac{\iint \beta_x(x, y) I(x, y) dx dy}{\iint I(x, y) dx dy}, \quad (\text{A.6a})$$

$$\langle u_y \rangle = \frac{\iint \beta_y(x, y) I(x, y) dx dy}{\iint I(x, y) dx dy}. \quad (\text{A.6b})$$

The second-order angular moment is used to determine the divergence of the beam. The x - and y -divergence is given by

$$\theta_x = 4\sqrt{\langle u_x^2 \rangle}, \quad (\text{A.7a})$$

$$\theta_y = 4\sqrt{\langle u_y^2 \rangle}, \quad (\text{A.7b})$$

For calculation of the beam propagation factor \mathcal{M}^2 and twist parameter τ mixed second-order moments are needed. The mixed moment of x and u_x is given by

$$\langle xu_x \rangle = \frac{\iint (x - \langle x \rangle) (\beta_x(x, y) - \langle u_x \rangle) I(x, y) dx dy}{\iint I(x, y) dx dy}. \quad (\text{A.8})$$

Other mixed moments, eg. $\langle xy \rangle$ or $\langle yu_x \rangle$, can be calculated the same way. From the mixed second-order moments, the beam propagation factor \mathcal{M}^2 can be calculated as

$$\mathcal{M}_x^2 = \frac{4\pi}{\lambda} \sqrt{\langle x^2 \rangle \langle u_x^2 \rangle - \langle xu_x \rangle^2}, \quad (\text{A.9a})$$

$$\mathcal{M}_y^2 = \frac{4\pi}{\lambda} \sqrt{\langle y^2 \rangle \langle u_y^2 \rangle - \langle yu_y \rangle^2}, \quad (\text{A.9b})$$

and the twist parameter τ is given by

$$\tau = \langle yu_x \rangle - \langle xu_y \rangle. \quad (\text{A.10})$$

For the sake of simplicity the point of origin of the coordinate system should be chosen such that the first order moments vanish. This greatly simplifies the equations.

To fully describe an arbitrary beam it is possible to combine all the beam parameters into one compact form. The so called beam matrix [9] contains all information about the beam. It is given by

$$P = \begin{pmatrix} \langle x^2 \rangle & \langle xy \rangle & \langle xu_x \rangle & \langle xu_y \rangle \\ \langle xy \rangle & \langle y^2 \rangle & \langle yu_x \rangle & \langle yu_y \rangle \\ \langle xu_x \rangle & \langle yu_x \rangle & \langle u_x^2 \rangle & \langle u_x u_y \rangle \\ \langle xu_y \rangle & \langle yu_y \rangle & \langle u_x u_y \rangle & \langle u_y^2 \rangle \end{pmatrix}. \quad (\text{A.11})$$

From the beam matrix many beam properties can be extracted directly. One beam parameter which describes the overall beam focusability is the effective beam propagation factor

$$\mathcal{M}_{\text{eff}}^2 = \frac{4\pi}{\lambda} \sqrt[4]{\det P}. \quad (\text{A.12})$$

Appendix B

Zernike Polynomials

For the treatment of wavefronts of circular beams one typically uses Zernike polynomials. The Zernike polynomials are a complete set of complex functions which are orthogonal inside the unit circle. In the following the Zernike polynomials are shortly described. For a more complete description of how the Zernike polynomials can be derived see [1].

B.1 Fundamentals of the Zernike polynomials

For coordinates (x, y) with $x = \rho \cos \theta$ and $y = \rho \sin \theta$ the wavefront can be described by a function $V(x, y)$. Because of its symmetries $V(x, y)$ can be separated into

$$V(\rho \cos \theta, \rho \sin \theta) = R(\rho) e^{il\theta}, \quad (\text{B.1})$$

where (ρ, θ) correspond to polar coordinates.

If V is a polynomial of degree n in (x, y) it follows that $R(\rho)$ is also a polynomial of degree n in ρ and furthermore contains only powers of ρ greater than or equal to $|l|$.

With this information one can express the Zernike polynomials in polar coordinates as

$$Z_n^l(\rho, \theta) = a_n R_n^l(\rho) e^{il\theta} \quad (\text{B.2})$$

where n and l are integer numbers with $n \geq |l|$ and even values for $(n - |l|)$. Here a_n is a normalization constant which is independent of l .

The *radial Zernike polynomials* $R_n^l(\rho)$ satisfy

$$\int_0^1 R_n^l(\rho) R_{n'}^l(\rho) \rho d\rho = \frac{1}{a_n a_{n'}} \delta_{nn'} \quad (\text{B.3})$$

and are therefore orthogonal.

Because $(n - |l|)$ must be even, n can only take the values $|l|, |l| + 2, |l| + 4$, and so forth. This leads to the symmetry

$$R_n^{-l}(\rho) = \beta_n^l(\rho) R_n^l(\rho) \quad (\text{B.4})$$

where $\beta_n^l(\rho)$ only depends on a_n . Because of this symmetry, a_n can be chosen such that Equation (B.2) simplifies to

$$Z_n^{\pm m}(\rho, \theta) = a_n R_n^m(\rho) e^{\pm i m \theta} \quad (\text{B.5})$$

with $m = |l|$.

Instead of using the complex polynomials given by Equation (B.5) for the description of wavefronts it is easier to use only real functions. These are given by

$$Z_n^m(\rho, \theta) = \begin{cases} a_n R_n^m(\rho) \cos(m\theta) & \text{for } m \geq 0 \\ a_n R_n^m(\rho) \sin(m\theta) & \text{for } m < 0 \end{cases}, \quad (\text{B.6})$$

which is in fact Equation (2.7) described in Chapter 2.

B.2 Explicit expression of the Zernike polynomials

For the evaluation of wavefronts, explicit expressions of the Zernike polynomials are needed. There are different expressions for the Zernike polynomials which result in slightly different sets of polynomials. These sets have slightly different properties regarding individual terms. In this work the typically used set described in [1] is applied. Other commonly used sets and their special properties can be found in [132–136].

The radial Zernike polynomials are represented by a series. The series

$$R_n^m(\rho) = \sum_{s=0}^{\frac{n-m}{2}} (-1)^s \frac{(n-s)!}{s! \left(\frac{n+m}{2} - s\right)! \left(\frac{n-m}{2} - s\right)!} \rho^{(n-2s)} \quad (\text{B.7})$$

is the usual representation. In this representation the normalization constant a_n is usually omitted. If $a_n = 1$ is used, the normalization is such that $R_n^m(\rho) = 1$ at the border of the unit circle ($\rho = 1$).

Other normalizations are also valid. Especially [14] uses a normalization given by

$$a_n = \sqrt{2(n+1)} \quad (\text{B.8})$$

which makes the Zernike polynomials orthonormal (see Equation (B.3)) and satisfies

$$\int_0^1 (a_n R_n^m(\rho)) (a_{n'} R_{n'}^m(\rho)) \rho \, d\rho = \delta_{nn'}. \quad (\text{B.9})$$

For a normalization $R_n^m(1) = 1$ the Zernike polynomials in Cartesian coordinates and their corresponding optical aberrations are given in Table B.1.

Z_k	Z_n^m	polynomial (in Cartesian coordinates)	aberration
Z_0	Z_0^0	1	piston
Z_1	Z_1^1	x	x-tilt
Z_2	Z_1^1	y	y-tilt
Z_3	Z_2^2	$2xy$	45° astigmatism
Z_4	Z_2^0	$2x^2 + 2y^2 - 1$	defocus
Z_5	Z_2^2	$-x^2 + y^2$	90° astigmatism
Z_6	Z_3^3	$-x^3 + 3xy^2$	x-trefoil
Z_7	Z_3^1	$3x^3 + 3xy^2 - 2x$	x-coma
Z_8	Z_3^1	$3x^2y + 3y^3 - 2y$	y-coma
Z_9	Z_3^3	$y^3 - 3x^2y$	y-trefoil
Z_{10}	Z_4^4	$-4x^3y + 4xy^3$	
Z_{11}	Z_4^2	$8x^3y + 8xy^3 - 6xy$	
Z_{12}	Z_4^0	$6x^4 + 12x^2y^2 + 6y^4 - 6x^2 - 6y^2 + 1$	
Z_{13}	Z_4^2	$-4x^4 + 4y^4 + 3x^2 - 3y^2$	
Z_{14}	Z_4^4	$x^4 - 6x^2y^2 + y^4$	
Z_{15}	Z_5^5	$x^5 - 10x^3y^2 + 5xy^4$	
Z_{16}	Z_5^3	$-5x^5 + 10x^3y^2 + 15xy^4 + 4x^3 - 12xy^2$	
Z_{17}	Z_5^1	$10x^5 + 20x^3y^2 + 10xy^4 - 12x^3 - 12xy^2 + 3x$	
Z_{18}	Z_5^1	$10x^4y + 20x^2y^3 + 10y^5 - 12x^2y - 12y^3 + 3y$	
Z_{19}	Z_5^3	$-15x^4y - 10x^2y^3 + 5y^5 + 12x^2y - 4y^3$	
Z_{20}	Z_5^5	$5x^4y - 10x^2y^3 + y^5$	
Z_{21}	Z_6^6	$6x^5y - 20x^3y^3 + 6xy^5$	
Z_{22}	Z_6^4	$-24x^5y + 24xy^5 + 20x^3y - 20xy^3$	
Z_{23}	Z_6^2	$30x^5y + 60x^3y^3 + 30xy^5 - 40x^3y - 40xy^3 + 12xy$	
Z_{24}	Z_6^0	$20x^6 + 60x^4y^2 + 60x^2y^4 + 20y^6 - 30x^4 - 60x^2y^2 - 30y^4 + 12x^2 + 12y^2 - 1$	
Z_{25}	Z_6^2	$-15x^6 - 15x^4y^2 + 15x^2y^4 + 15y^6 + 20x^4 - 20y^4 - 6x^2 + 6y^2$	
Z_{26}	Z_6^4	$6x^6 - 30x^4y^2 - 30x^2y^4 + 6y^6 - 5x^4 + 30x^2y^2 - 5y^4$	
Z_{27}	Z_6^6	$-x^6 + 15x^4y^2 - 15x^2y^4 + y^6$	

Table B.1: Zernike polynomials in Cartesian coordinates (normalized to $R_n^m(\rho) = 1$ for $\rho = 1$) as used in the optimization algorithm. The numbering k follows references [21, 22, 26]. For easier comparison of different numbering schemes, the order of the Zernike polynomials with the convention used here is given. The boxes group aberrations with the same radial order n .

B.3 Using and Interpreting Zernike polynomials

When using Zernike polynomials Z_k to describe wavefronts, the corresponding Zernike coefficients c_k contain important information about the beam. As some polynomials correspond to primary Seidel aberrations, the physical interpretation of the corresponding coefficients is quite simple. In the following the meaning of the coefficients of some Zernike polynomials with special properties are given.

B.3.1 The defocus coefficient c_4

The defocus coefficient c_4 of the Zernike polynomial Z_4 , shown in Figure B.1, can be used to calculate the radius of curvature of the beam. As the Zernike polynomials are

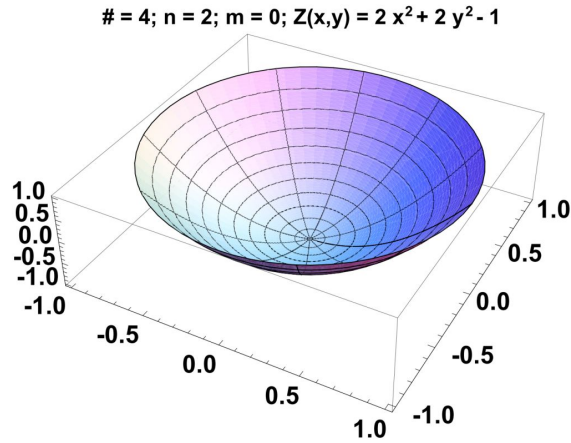


Figure B.1: Plot of the Zernike polynomial Z_4 . It corresponds to a defocus of the beam.

defined inside the unit circle, the coefficients given here are normalized accordingly. In experiments, however, the Zernike coefficients are typically given either in units of wavelength λ or in units of μm . This has to be taken into account when calculating the radius of curvature.

The wavefront of a Gaussian beam is shown in Figure B.2. For such a geometry the chord of the circle s and the height of the circular segment h can be given as

$$h = 2c_4 \text{ and } s = 2W, \quad (\text{B.10})$$

where c_4 corresponds to the defocus coefficient and W to the beam width. Using basic geometry the radius of curvature of the Gaussian beam can be calculated as

$$R = \frac{16c_4^2 + 4W^2}{16c_4}. \quad (\text{B.11})$$

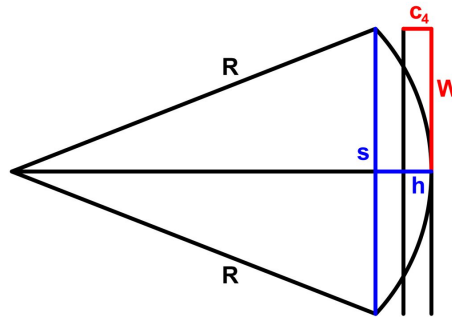


Figure B.2: The radius of curvature R of a beam, determined by beam width W and defocus coefficient c_4 .

As discussed in Chapter 1, the Gaussian beam parameter q can be calculated from the radius of curvature R and the beam width W . With the help of the Gaussian beam parameter, the distance from the beam waist and the Rayleigh length of the beam can be retrieved. Combining Equations (1.19) and (1.18) gives

$$q = \frac{\frac{1}{R}}{\frac{1}{R^2} + \frac{\lambda^2}{\pi^2 W^4}} + i \frac{\frac{\lambda}{\pi W^2}}{\frac{1}{R^2} + \frac{\lambda^2}{\pi^2 W^4}} \stackrel{!}{=} z + i z_R. \quad (\text{B.12})$$

Here, the real part of the Gaussian beam parameter $\Re\{q\}$ gives the distance z from the beam waist and the imaginary part $\Im\{q\}$ corresponds to the Rayleigh length z_R of the beam.

B.3.2 The effect of astigmatism

The Zernike polynomials Z_3 and Z_4 correspond to two orthogonal parts of beam astigmatism. Plots of both polynomials are shown in Figure B.3.

The Zernike polynomial Z_3 corresponds to a 45° astigmatism and the polynomial Z_5 corresponds to a 90° astigmatism. The effect of both parts of astigmatism on a Gaussian beam are shown in Figure B.4. As can be seen, the astigmatism leads to the effect that two beam waists occur at different positions along the propagation axis. In case of 45° astigmatism, the main axes of the beam waists are rotated by 45° with respect to the x - and y -axes. In case of 90° astigmatism, the main axes of the beam waists correspond to the x - and y -axes.

As the orientation of the x - and y -axes is determined by experimental conditions, this definition, however, is quite arbitrary. For regular beams astigmatism always leads to two perpendicularly oriented beam waists. The exact orientation of the main axes with respect to the x - and y -axes can always be described in terms of 45° and 90° astigmatism. This can be done by using a linear combination of Zernike polynomials Z_3 and Z_5 . As such, the relative strengths of the Zernike coefficients c_3 and c_5 determine the exact orientation of the main axes.

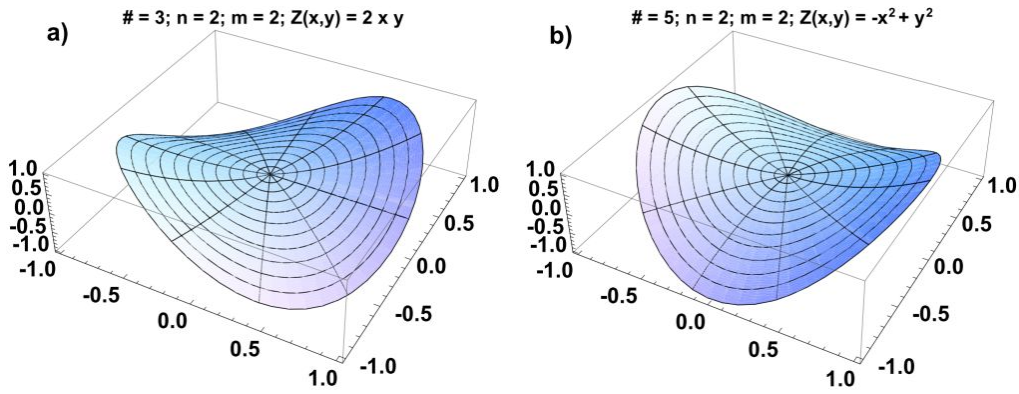


Figure B.3: a) Plot of the Zernike polynomial Z_3 corresponding to the 45° astigmatism. b) Plot of the Zernike polynomial Z_5 corresponding to the 90° astigmatism.

B.3.3 Calculating the \mathcal{M}^2 parameter

In Appendix A it is described how the \mathcal{M}^2 parameter can be retrieved from the second-order beam moments. In order to calculate the \mathcal{M}^2 parameter both the spatial beam moments and the angular beam moments are required. The spatial beam moments are calculated from the intensity profile alone. Therefore, they can be determined as part of a Shack–Hartmann measurement or from a separate beam profile measurement. The angular beam moments, however, need information about the local angular shift which is contained in the wavefront described by Zernike polynomials.

The local angular shift β originates from the local deviation of the wavefront from a spherical wave. This deviation corresponds to the wave aberration Φ which is discussed in Chapter 2. The local angular shifts along the x - and the y -axes can be calculated as

$$\beta_x = -\frac{d\Phi}{dx} \quad (\text{B.13a})$$

and

$$\beta_y = -\frac{d\Phi}{dy}, \quad (\text{B.13b})$$

where $\Phi(x, y)$ is the wave aberration. As mentioned above, the wave aberration is in fact the wavefront without the terms for piston (Z_0), tilt (Z_1, Z_2) and defocus (Z_4). From this the \mathcal{M}^2 parameter can be calculated using Equation (A.9).

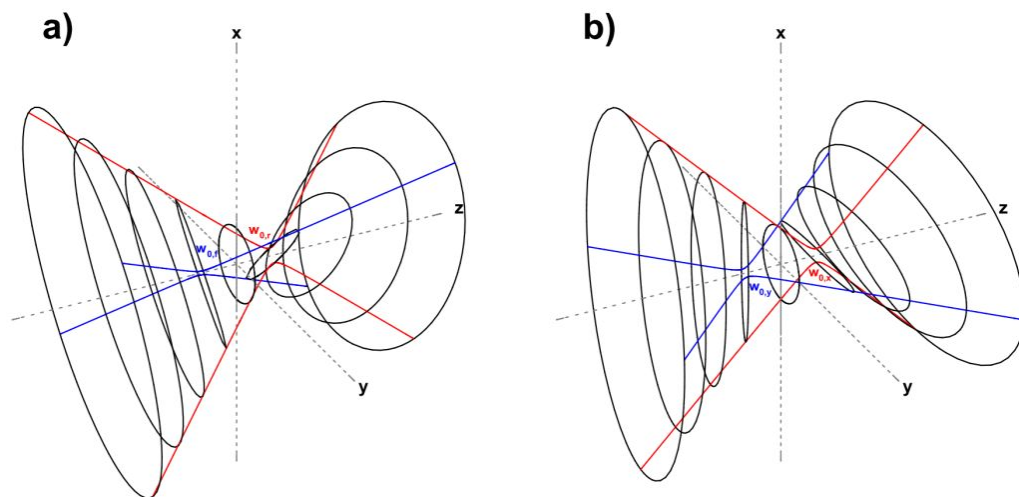


Figure B.4: Effect of the a) 45° astigmatism and the b) 90° astigmatism on a Gaussian beam.

B.3.4 Comparing Zernike coefficients

As was shortly discussed at the beginning of Section B.2, there are different sets of Zernike polynomials. Together with different possible normalizations and numbering schemes it can be difficult to compare Zernike coefficients from different resources.

In order to do a comparison of Zernike coefficients between two resources, extreme caution is necessary to ensure that the same set of Zernike polynomials was used. Additionally, before the data can be compared it has to be corrected for the use of the same normalization.

Appendix C

The genetic algorithm

The genetic algorithm is a special implementation of an evolutionary algorithm [137]. The genetic algorithm used in this work is very similar to the one given by Judson and Rabitz [87] and is also described in [26, 49] and elsewhere.

C.1 Basics

The genetic algorithm is based on the idea of “survival of the fittest”. Each iteration step, called “generation”, contains a (fixed) number of “individuals”. Each individual is described by a set of parameters. These parameters are called “genes”.

All possible gene combinations create the so called search space. In order to find the global maximum the whole search space must be accessible, i.e., all possible gene values must be present in a generation. The size of the accessible parts of the search space can be quantified by the so called diversity. There are several possible ways to define the term diversity [137]. In this work, however, the diversity was not calculated and is only mentioned for the sake of completeness.

During the course of the optimization the population can converge to a local or global maximum. For a fully converged population the diversity is minimal as all individuals are identical. Such a population is trapped inside the maximum. In this case a local maximum cannot be distinguished from the global maximum. One possible counter to this problem is the use of mutation, which is described further down, as part of the reproduction cycle. Mutation ensures that the whole search space is accessible at all times [137].

In order to optimize a physical system, each individual is applied to the system under test and the quality of the measured result is evaluated. The quality, which is calculated as a number, is called the “fitness”. After all individuals are tested only the fittest individuals of the generation are carried over to the next generation.

Based on the fittest individuals of the previous generation, the new generation is created. The way this is done is also inspired by nature. In our case, three operations

– “cloning”, “cross-over” and “mutation” – are used. The amount of clones, cross-over individuals and mutants as well as the strength of the mutation strongly depend on the problem and must be adapted accordingly.

The clones are, as the name suggests, just copies of the fittest individuals of the last generation. In case of the cross-over operation, two of the fittest individuals of the last generation are chosen randomly. These two individuals serve as “parents”. Each parent individual contributes half of its genes to form a new “child” individual. Mutation is the last operation which is used. For mutation, one of the fittest individuals of the last generation is chosen randomly. Afterwards, a small amount of the genes of this individual is changed randomly.

The properties of the “reproduction” operations are controlled by free parameters. In this work the parameters parents ratio, clone content, cross-over content, mutation probability and mutation deviation were used. The parameters parents ratio, clone content and cross-over content are given as percentage in order to be independent from the number of “individuals” present in a generation. In order to create a new generation, the clones from the previous generation are taken first. The number of clones is determined by the clone content parameter. In a second step the number of individuals which can serve as parent individuals for the cross-over and mutation operations is determined by the parents ratio. From these parents the cross-over individuals, where the number of cross-over individuals is given by the cross-over content parameter, are then calculated. In a last step the mutated individuals are calculated from the parent individuals. Each gene is mutated with a probability given by the mutation probability. In case of mutation the gene is changed using a random number. This random number is taken from the interval $[-\sigma; \sigma]$ with σ being the mutation deviation. In order to ensure a constant generation size, the number of mutant individuals is determined accordingly.

For heuristic search methods, the speed and the success of the optimization depend on the form of the problem. This means that the search space has to be parameterized in a way suitable for the genetic algorithm. In cases where this cannot be achieved other optimization methods should be used.

C.2 Parameterization

The use of the genetic algorithm for the phase optimization is based on the principle that certain pulse or beam parameters are linearly independent. In case of the spectral phase, these can be the components of the polynomial expansion of the spectral phase. For the spatial phase, the wavefront can be expanded into Zernike polynomials, as described in Chapter 2. In terms of the genetic algorithm, the expansion coefficients serve as “genes”. The laser pulse which is described by these parameters corresponds to the “individual”. In the following the parameterizations used in the scope of this work are discussed in more detail.

C.2.1 Tiltable Planes

For the spatial optimization of filaments described in Chapter 7 a high-resolution spatial light modulator (SLM) was used. The SLM has a very high number of degrees of freedom. The active area has 768×768 pixels and each pixel can be addressed with 8 bit resolution. Due to this high number of degrees of freedom the genetic algorithm would take a very large amount of time and computational power to optimize laser pulses. The easiest way to reduce the time and the computational power needed is to use a process called binning. This is done by combining multiple pixels into one larger meta-pixel. This effectively reduces the pixel resolution of the SLM.

In order to reduce the needed computational power without losing too much spatial resolution, a parameterization based on tiltable planes was used. This parameterization is an improved version of the simple binning technique [26, 49]. Similar to binning, the active area is divided into smaller areas. However, these smaller areas do not form meta-pixels where each pixel has the same value, but form planes which can be tilted. This concept is shown in Figure C.1 where it is compared to simple

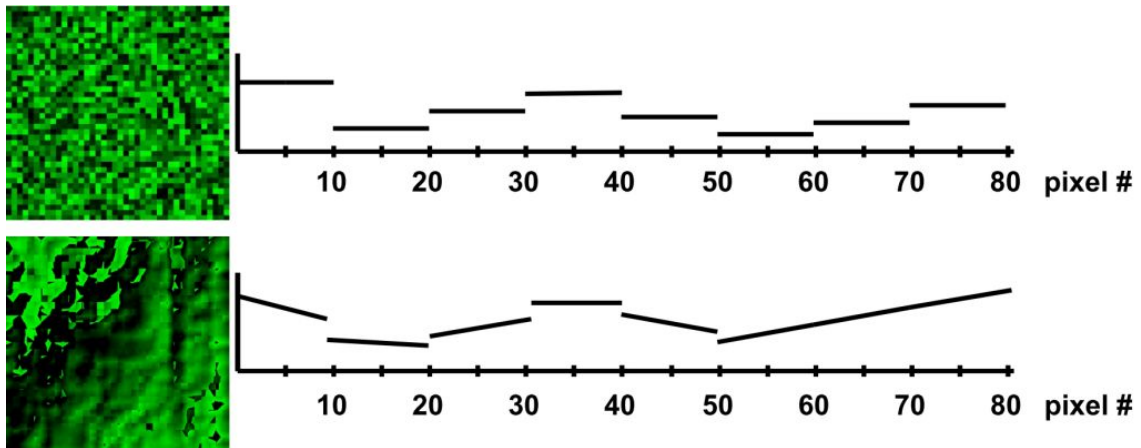


Figure C.1: Comparison between binning (top) and tiltable planes (bottom). On the left side images of optimized phase masks are shown. From [26].

binning. The binning technique is shown at the top and the tiltable planes at the bottom of the figure. On the left hand side images of optimized phase masks are shown. The phase mask created with tiltable planes shows a much smoother phase surface than the phase mask created with binning. This smoother phase distribution is better suited for laser pulses as phase jumps other than $\Delta\phi = m 2\pi$ with m being an integer number usually create unwanted diffraction patterns.

The binning technique only needs one color value to describe a meta-pixel. In order to fully describe a tiltable plane, however, three coordinates are required. In the algorithm used during this work, the color level at three corners of the plane was used. These three points fully define the plane, and the color level of all other pixels can be calculated from these. Thus, tiltable planes need three times the number

of genes compared to binning, but effectively utilize the full resolution of the SLM. Compared to standard optimizations with full resolution, tiltable planes reduce the needed computational power considerably.

C.2.2 Zernike Polynomials

Another approach which uses the high resolution of the SLM is the parameterization of the phase mask by Zernike polynomials. This was done during the high-order harmonic generation with wavefront controlled laser pulses described in Chapter 9. During this experiment the SLM was used to imprint phase masks onto the incoming laser beam. As the incident laser beam was collimated, these phase masks correspond to the wavefront of the laser beam after the SLM. In Chapter 2 it is shown that it is helpful to describe wavefronts in terms of Zernike polynomials. This is due to the fact that the expansion coefficients allow for a quantitative physical interpretation of optical aberrations present in the beam. The properties of Zernike polynomials, the way they are connected to optical aberrations and how they can be derived is described in Chapter 2 and in Appendix B.

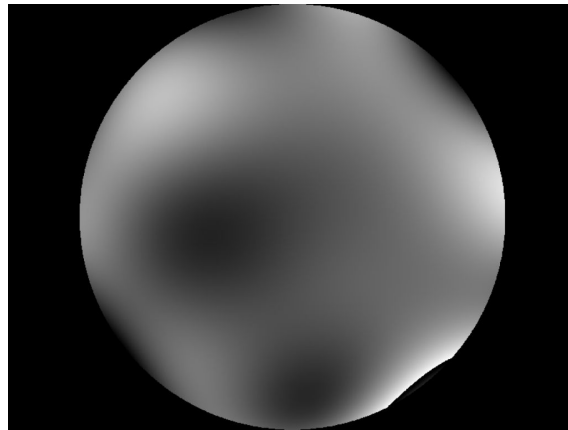


Figure C.2: Example of a phase mask created by the genetic algorithm. In this case Zernike polynomials were used to describe the phase mask. The Zernike coefficients c_0 to c_{27} serve as genes for the genetic algorithm.

An example of the phase masks which are created by the genetic algorithm is shown in Figure C.2. In this case Zernike polynomials were used to describe the phase mask. For this parameterization the Zernike coefficients c_0 to c_{27} serve as genes.

Appendix D

McPherson 248/310G

The McPherson 248/310G spectrometer is a grazing incidence spectrometer for the XUV regime. In Figure D.1 a photo of the actual spectrometer with the imaging detector is shown.

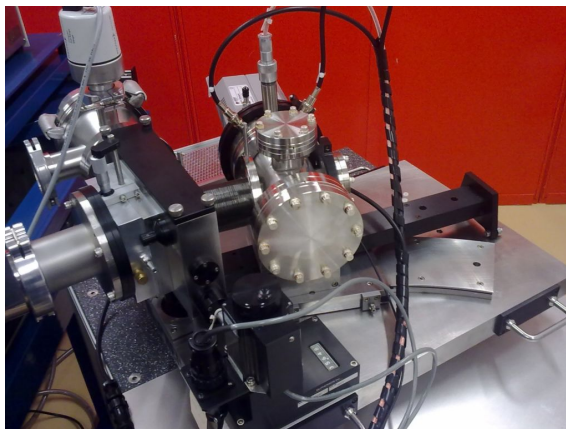


Figure D.1: The McPherson 248/310G spectrometer (with imaging detector) as used in the laboratory.

This chapter describes the basic principles of the McPherson 248/310G spectrometer as well as the detection scheme and how to evaluate the measured data. Not all details are covered here. For more technical information see [129, 138–140].

D.1 Basics

The McPherson 248/310G spectrometer is based on the Rowland circle principle, which is shown in Figure D.2. Due to this, some caution has to be taken when it is used together with an imaging detector.

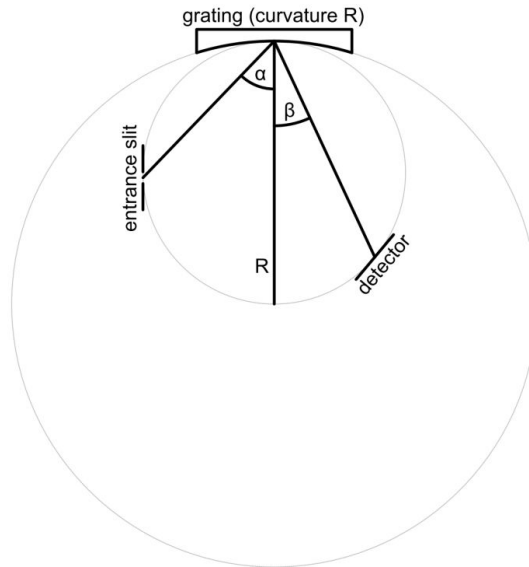


Figure D.2: The Rowland Circle. When using a (concave or cylindrical) grating with a radius of curvature R , the surface of the grating is part of a large circle. A second circle, the so called Rowland circle, can be constructed for such a setup. This smaller circle has a diameter of R and touches the larger circle at the center of the grating. When the entrance slit is placed on the Rowland circle, all diffracted wavelengths are focused onto other points of the Rowland circle.

In this geometry, the wavelength for a given angle of incidence α and a diffraction angle β (in first order) is given by

$$\lambda = \frac{1}{g} (\sin \alpha - \sin \beta), \quad (\text{D.1})$$

where g is the groove density, typically measured in $\frac{\text{lines}}{\text{mm}}$.

D.2 Detection & Spectral foreshortening

The McPherson 248/310G spectrometer is equipped with an imaging detector. Optionally, an exit slit for use as scanning spectrometer can be used.

The imaging detector consists of a single stage multi-channel plate (MCP) [141] which is coupled to a CCD detector using a fiber-optic taper with a reduction ratio of 40 : 25. The photocathode in front of the MCP is made of Cesium Iodide (CsI) to detect XUV photons. The phosphor screen behind the MCP is made of P43 [142], which has a decay time of a few ms.

The CCD used to read out the MCP is an Andor DH420-FO. It is an OEM version of the Andor iDus 420 series. No manual for the DH420-FO is available. The manual of the Andor iDus [143] has to be used instead.

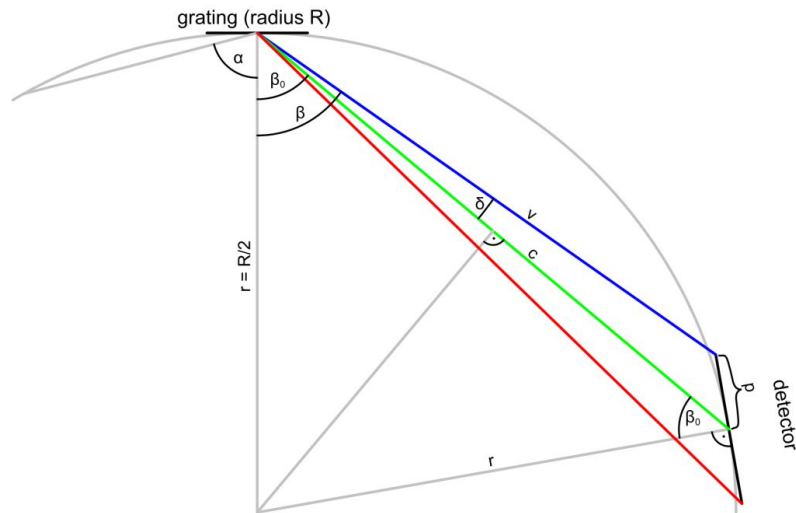


Figure D.3: The effect of spectral foreshortening. For a fixed detector position, typically only one intersection point (two at most) of the detector with the Rowland circle exist. For pixels which are not at the intersection of the detector and the Rowland circle, the length v corresponding to the diffraction angle $\beta = \beta_0 + \delta$, cannot be used directly (as effective chord length) to calculate the wavelength λ . Instead the exact angle β has to be calculated.

The detector can be mounted in two slightly different configurations. In the tangential configuration, the detector plane is the tangent to the Rowland circle. In a more general configuration, the detector is moved slightly towards the center of the Rowland circle. This way, two intersection points of the detector plane with the Rowland circle exist and the overall spectral foreshortening (see Figure D.3 and [138]) can be minimized.

For the Rowland circle geometry, the diffraction angle β_0 can be calculated by

$$\beta_0 = \arccos\left(\frac{c}{2r}\right) = \arccos\left(\frac{c}{R}\right) \quad (\text{D.2})$$

where R is the radius of curvature of the grating and c is the chord length (see Figure D.3). For pixels which are not at the intersection of the detector and the Rowland circle, the length v corresponding to the diffraction angle $\beta = \beta_0 + \delta$, cannot be used directly (as effective chord length) to calculate the wavelength λ . Instead the exact angle β has to be calculated.

D.3 Mapping detector position to wavelength

As mentioned above, the exact angle β has to be calculated for each pixel. This mapping of the pixel position on the detector to the respective wavelengths is discussed in the following.

D.3.1 Basic overview

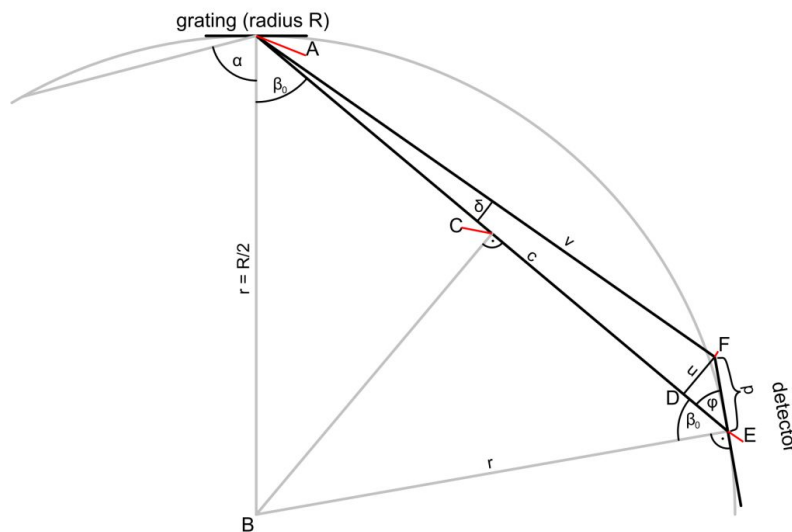


Figure D.4: Principle of an imaging Rowland circle spectrometer with all needed quantities. In the so called tangential configuration, shown here, the detector plane is the tangent to the Rowland circle at the point E . The quantities R (radius of curvature), c (chord length), p (position on detector relative to the center of the detector) and α (angle of incidence) are known from the experiment.

For a spectrometer in Rowland geometry, as shown in Figure D.4, the diameter of the Rowland circle is the radius of curvature of the grating. Therefore the identity

$$r = \frac{R}{2} \quad (\text{D.3})$$

is valid.

In the experiment the quantities R , c , p and α are known. Here, grating parameters are the groove density g (typically given in lines/mm) and the radius of curvature R of the grating. The detector parameters are the chord length c and the position p on the detector relative to the center of the detector. The angle of incidence α depends on the exact position of the entrance slit.

The grating parameters are known and the detector parameters can be retrieved from the experiment. The chord length c can be read from a mechanical counter which is mounted on the spectrometer. The counter displays the chord length in inches. The detector position p can be calculated from the image/signal. As each CCD pixel is $26\ \mu\text{m}$ wide and the fiber-optic has a reduction ratio of 40 : 25 the effective pixel size is $41.6\ \mu\text{m}$. In the default configuration the angle of incidence is $\alpha = 87^\circ$.

D.3.2 Calculating the needed angles – tangential configuration

In the following it is assumed, that the detector plane is the tangent to the Rowland circle at the point E! This is shown in Figure D.4.

The angle β_0 can be calculated from the triangle ABC . Together with the relation of r and R this can be written as

$$\cos \beta = \frac{c/2}{r} = \frac{c}{R}. \quad (\text{D.4})$$

This way, the angle β_0 is given by

$$\boxed{\beta_0 = \arccos\left(\frac{c}{R}\right)}. \quad (\text{D.5})$$

In the triangle DEF , the angle ϕ is related to the angle β_0 by

$$\phi = 90^\circ - \beta_0. \quad (\text{D.6})$$

The length u is given by

$$u = p \sin \phi = p \cos \beta_0 = \frac{pc}{R}. \quad (\text{D.7})$$

In the triangle ADF , the law of cosines can be used to calculate the length v . It is given by

$$v^2 = p^2 + c^2 - 2pc \cos \phi = p^2 + c^2 - 2pc \sin \beta_0. \quad (\text{D.8})$$

Inserting Equation (D.5) into Equation (D.8) and using the identity

$$\sin\left(\arccos\left(\frac{c}{R}\right)\right) = \sqrt{1 - \frac{c^2}{R^2}}, \quad (\text{D.9})$$

it is possible to calculate v by

$$v^2 = p^2 + c^2 - 2pc\sqrt{1 - \frac{c^2}{R^2}}. \quad (\text{D.10})$$

Here v contains only the known quantities c , p and R .

The angle δ is defined as the variation of the diffraction angle β when moving along the detector plane and away from the center of the detector. It is given by

$$\sin \delta = \frac{u}{v}. \quad (\text{D.11})$$

Using Equations (D.7) and (D.10), the angle δ is calculated as

$$\delta = \arcsin \left(\frac{pc}{R\sqrt{p^2 + c^2 - 2pc\sqrt{1 - \frac{c^2}{R^2}}}} \right) \quad (\text{D.12})$$

D.3.3 Calculating the needed angles – generalized configuration

In the more general configuration the detector is placed such that the detector plane is parallel to the tangent to the Rowland circle. This way it is possible to minimize the effect of spectral foreshortening and increase the effective resolution of the spectrometer.

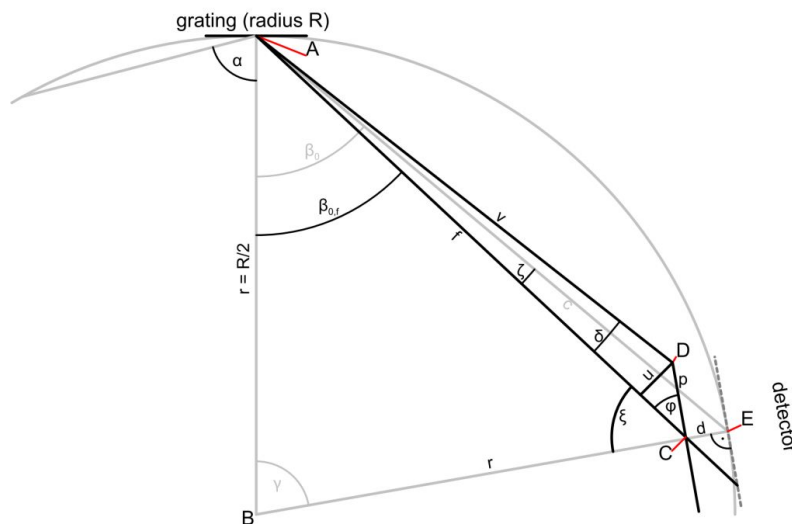


Figure D.5: Rowland circle spectrometer in generalized configuration. Here the detector plane is parallel to the tangent to the Rowland circle at the point E . The quantities R , c , p , d and α are known from the experiment.

Figure D.5 shows the more general configuration of the Rowland circle spectrometer. Compared to the tangential configuration, described in Section D.3.2, the detector is moved slightly closer (distance d) to the center of the Rowland circle. The angles needed to calculate the wavelength distribution along the detector can be calculated the same way as for the tangential configuration.

The shift of the detector by an amount d leads to a shift of the wavelength at the center of the detector. This shift corresponds to an angle ζ which can be calculated from the experimental parameters as

$$\zeta = \arccos\left(\frac{d^2 - c^2 - f^2}{2cf}\right), \quad (\text{D.13})$$

with the length f calculated in the triangle ABC as

$$f^2 = r^2 + (r - d)^2 - 2r(r - d)\cos\gamma. \quad (\text{D.14})$$

The angle γ is given by

$$\gamma = 2 \arcsin\left(\frac{c}{R}\right). \quad (\text{D.15})$$

Because the angle γ is the same for the generalized configuration and the tangential configuration, two new angles $\beta_{0,f}$ and ξ can be derived as

$$\beta_{0,f} = \beta_0 - \zeta, \quad (\text{D.16})$$

and

$$\xi = \beta_0 + \zeta. \quad (\text{D.17})$$

With the help of these angles, the angles needed to calculate the wavelength distribution can be derived. The angle δ for the generalized configuration, as for the tangential configuration, is given by

$$\sin\delta = \frac{u}{v}. \quad (\text{D.18})$$

The value of v can be calculated from the triangle ACD as

$$v^2 = p^2 + f^2 - 2pf\cos\phi \quad (\text{D.19})$$

with

$$\phi = 90^\circ - \xi. \quad (\text{D.20})$$

The value of u is given by

$$u = p\sin\phi \quad (\text{D.21})$$

Using the Equations above, the angle δ (here called δ_f to avoid confusion with the

tangential configuration) is calculated by

$$\delta_f = \arcsin\left(\frac{p \cos \xi}{\sqrt{p^2 + f^2 - 2pf \sin \xi}}\right). \quad (\text{D.22})$$

D.3.4 Calculating wavelengths

The wavelength for a given angle of incidence α and a diffraction angle β (in first order) is given by

$$\lambda = \frac{1}{g} (\sin \alpha - \sin \beta), \quad (\text{D.23})$$

where g is the groove density, typically measured in $\frac{\text{lines}}{\text{mm}}$. To calculate the wavelength at a certain position p on the detector, the corresponding angle β is needed.

For the tangential configuration the angle β is given by

$$\beta = \beta_0 + \delta = \arccos\left(\frac{c}{R}\right) + \arcsin\left(\frac{pc}{R\sqrt{p^2 + c^2 - 2pc\sqrt{1 - \frac{c^2}{R^2}}}}\right), \quad (\text{D.24})$$

where $\beta_0 = \arccos\left(\frac{c}{R}\right)$ is the angle corresponding to the center of the detector.

For the generalized configuration the angle β is given by

$$\beta = \beta_{0,f} + \delta_f = \beta_0 - \zeta + \arcsin\left(\frac{p \cos(\beta_0 + \zeta)}{\sqrt{p^2 + f^2 - 2pf \sin(\beta_0 + \zeta)}}\right). \quad (\text{D.25})$$

Here $\beta_0 = \arccos\left(\frac{c}{R}\right)$ is the angle corresponding to the center of the detector in tangential configuration and

$$\zeta = \arccos\left(\frac{d^2 - c^2 - f^2}{2cf}\right) \quad (\text{D.26})$$

with

$$f^2 = r^2 + (r - d)^2 - 2r(r - d) \cos\left(2 \arcsin\left(\frac{c}{R}\right)\right). \quad (\text{D.27})$$

D.4 The spectrometer software

The control software for the McPherson 248/310G spectrometer was designed in LabVIEW specifically for the use in the laboratory of the *Quantum-electronics group* at the “Institute of Optics and Quantum-electronics (IOQ)” at the Friedrich-Schiller

University Jena. It is based on the software used with a self-built spectrometer which used an X-ray CCD from Andor (DO420-BN).

D.4.1 The control software

The user interface of the control software mainly consists of a main window, which controls the spectrometer and grants access to several configuration dialogs.

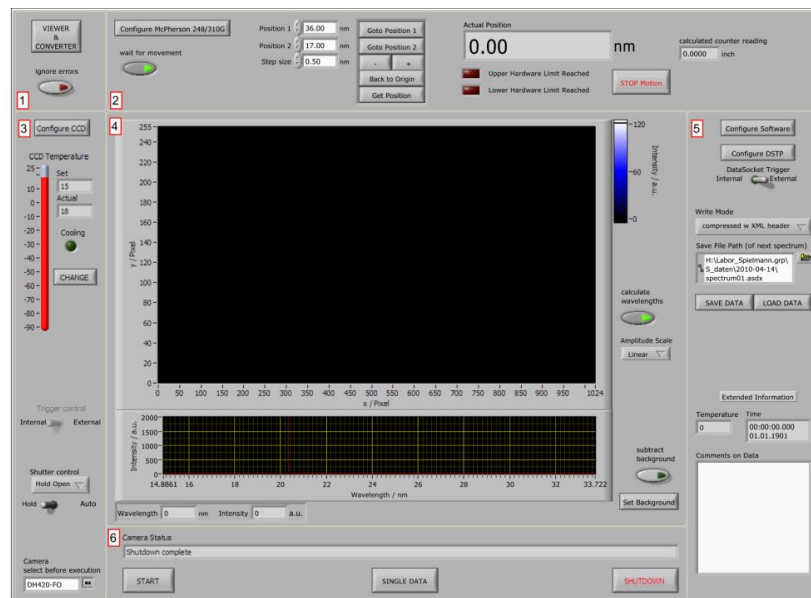


Figure D.6: User interface of the McPherson spectrometer software. The different regions are marked for better readability.

The main window, as shown in Figure D.6, consists of six regions. Each region contains controls and indicators for a specific task. Not all parameters can be accessed using the main window. For some configuration options special configuration dialogs can be opened through buttons placed in the respective region.

For full information about the control software for the McPherson 248/310G spectrometer see [129].

D.4.2 Viewer & Converter – ASDX-Viewer&Converter.vi

To view and convert data recorded with the LabVIEW software the “ASDX-Viewer & Converter” is available. It can be called from within the control software, mentioned in Section D.4.1. Alternatively it can be started directly.

In Figure D.7 the user interface of the Viewer&Converter is shown. The appearance is very similar to the spectrometer software. Like the main window of the

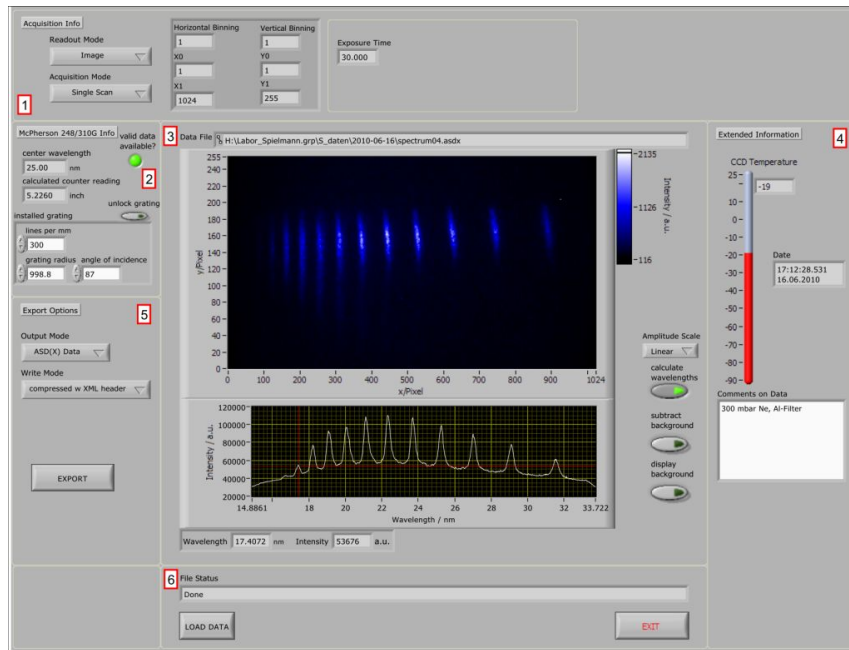


Figure D.7: User interface of the ASDX-Viewer&Converter. The regions are marked for better readability.

spectrometer software the user interface of the Viewer&Converter is divided into six regions.

A full description of usage and the capabilities of the Viewer&Converter is given in [129].

D.4.3 The ASDX-File Format

The ASDX file format, used to save measurement data to the hard disk, was created for the use with Andor-CCDs. Initially it was created as successor to the old ASD file format which was used with the old XUV spectrometer built in Wuerzburg [88]. Later it was extended to store additional data. This was necessary to save the configuration of the McPherson 248/310G spectrometer.

Similar to *OASIS Open Document Format (ODF)* and *Office Open XML (OOXML)* the ASDX file format saves the configuration in XML, alongside the raw measurement data. Actually the ASDX file is a ZIP compressed file containing the following files.

- **header.xml** Contains information about the configuration of the detector and the spectrometer.
- **AABCCDD.dat** Contains the data and the background as received from the detector.

The file name of the data file is created during the save-process. It contains the timestamp in hexadecimal form. As the file format is implemented using LabVIEW 8.2, the timestamp uses January 1, 1904 as epoch date [144].

The `header.xml` contains all the information about the configuration of the detector and the spectrometer. This information is needed to interpret the raw data saved in the corresponding data file.

For a full documentation of the file format and the structure of the XML header see [129].

Part IV
Lists and Literature

Bibliography

- [1] M. Born and E. Wolf. *Principles of Optics*. Cambridge University Press, Cambridge, 7th edition, 2009.
- [2] B. Saleh and M. Teich. *Grundlagen der Photonik*. Wiley-VCH, Weinheim, (1. dt. Aufl.) 2nd edition, 2008.
- [3] A. Siegman. *Lasers*. University Science Books, Mill Valley Calif., 1986.
- [4] Wikipedia, the free encyclopedia. *Paraxial approximation*. Published online. http://en.wikipedia.org/wiki/Paraxial_approximation. (2010-08-04, 15:02 UTC+02:00), 08 2010.
- [5] S. Feng and H. G. Winful. *Physical origin of the gouy phase shift*. *Opt. Lett.*, 26(8):485–487, 2001.
- [6] A. E. Siegman. *How to (maybe) measure laser beam quality*. In M. W. Dole (editor), *DPSS Lasers: Application and Issues*, OSA Trends in Optics and Photonics Series, volume 17, pages 184–199. Optical Society of America, Washington D.C., 1998.
- [7] A. E. Siegman. *New developments in laser resonators*. In D. A. Holmes (editor), *Optical Resonators*, volume 1224, pages 2–14. Proc. SPIE, 1990.
- [8] DIN EN ISO 11146-1. *Lasers and laser-related equipment - Test methods for laser beam widths, divergence angles and beam propagation ratios - Part 1: Stigmatic and simple astigmatic beams*. Deutsches Institut für Normung, 04 2005.
- [9] DIN EN ISO 11146-2. *Lasers and laser-related equipment - Test methods for laser beam widths, divergence angles and beam propagation ratios - Part 2: General astigmatic beams*. Deutsches Institut für Normung, 04 2005.
- [10] T. F. Johnston jr. *M² concept characterizes beam quality*. *Laser Focus World*, 5(26):173–183, 05 1990.
- [11] J. Eichler, L. Dünkel, and B. Eppich. *Die Strahlqualität von Lasern*. *Laser Technik Journal*, 1(2):63–66, 2004.
- [12] DIN EN ISO 15367-1. *Lasers and laser-related equipment - Test methods for determination of the shape of a laser beam wavefront - Part 1: Terminology and fundamental aspects*. Deutsches Institut für Normung, 02 2004.

- [13] J. Rayces. *Exact relation between wave aberration and ray aberration*. Journal of Modern Optics, 11(2):85–88, 03 1964.
- [14] DIN EN ISO 15367-2. *Lasers and laser-related equipment - Test methods for determination of the shape of a laser beam wavefront - Part 2: Shack-Hartmann sensors*. Deutsches Institut für Normung, 04 2005.
- [15] J. Liang, B. Grimm, S. Goelz, and J. F. Bille. *Objective measurement of wave aberrations of the human eye with the use of a Hartmann-Shack wave-front sensor*. J. Opt. Soc. Am. A, 11(7):1949–1957, 1994.
- [16] B. Platt and R. Shack. *History and principles of Shack-Hartmann wavefront sensing*. Journal of Refractive Surgery, 17(5):573–577, 10 2001.
- [17] J. Hartmann. *Bemerkungen über den Bau und die Justirung von Spektrographen*. Z. Instrumentenk., 20:47, 1900.
- [18] D. Malacara. *Optical shop testing*. Wiley-Interscience, Hoboken N.J., 3rd edition, 2007.
- [19] R. Díaz-Uribe, F. Granados-Agustín, and A. Cornejo-Rodríguez. *Classical hartmann test with scanning*. Opt. Express, 17(16):13959–13973, 2009.
- [20] R. Shack and B. Platt. *Production and Use of a Lenticular Hartmann Screen*. J. Opt. Soc. Am., 61(5):656, 1971.
- [21] M. Weger. *Charakterisierung der Wellenfront und Strahldivergenz von Hohen Harmonischen*. Diplomarbeit, Julius-Maximilians-Universität Würzburg, Experimentelle Physik I, Physikalisches Institut, 08 2007.
- [22] C. Kern. *Measuring low-order aberrations in High Harmonic beams with a Hartmann wave front sensor*. Diplomarbeit, Julius-Maximilians-Universität Würzburg, Experimentelle Physik I, Physikalisches Institut, 09 2008.
- [23] B. Schäfer and K. Mann. *Determination of beam parameters and coherence properties of laser radiation by use of an extended Hartmann-Shack wave-front sensor*. Applied Optics, 41(15):2809–2817, 2002.
- [24] B. Schäfer and K. Mann. *Investigation of the propagation characteristics of excimer lasers using a Hartmann-Shack sensor*. Review of Scientific Instruments, 71(7):2633–2668, 2000.
- [25] M. Kunzmann, B. Schäfer, and K. Mann. *Charakterisierung von Laserstrahlung mittels Hartmann-Shack-Wellenfrontsensor*. Photonik, 2005(1):52–55, 2005.
- [26] J. Lohbreier. *Characterization and Optimization of High-order Harmonics after Adaptive Pulse Shaping*. PhD thesis, Julius-Maximilians-Universität Würzburg, Experimentelle Physik I, Physikalisches Institut, 06 2008.

- [27] M. Schottner. *Algorithms for the application of Hartmann-Shack wavefront sensors in ophthalmology*. PhD thesis, Ruprecht-Karls-Universität Heidelberg, Kombinierte Fakultäten für Naturwissenschaften und Mathematik, 12 2002.
- [28] A. Borovsky, A. Galkin, O. Shiryayev, and T. Auguste. *Laser physics at relativistic intensities*. Springer, New York, 2003.
- [29] J. Diels and W. Rudolph. *Ultrashort laser pulse phenomena: fundamentals, techniques, and applications on a femtosecond time scale*. Academic Press, Burlington MA, 2nd edition, 2006.
- [30] T. Brabec and F. Krausz. *Intense few-cycle laser fields: Frontiers of nonlinear optics*. Reviews of Modern Physics, 72(2):545–591, 2000.
- [31] L. Xu, C. Spielmann, A. Poppe, T. Brabec, F. Krausz, and T. W. Hänsch. *Route to phase control of ultrashort light pulses*. Optics Letters, 21(24):2008, 1996.
- [32] P. Dombi, et al. *Direct measurement and analysis of the carrier-envelope phase in light pulses approaching the single-cycle regime*. New Journal of Physics, 6: 39–39, 2004.
- [33] R. Boyd. *Nonlinear optics*. Academic Press, Burlington MA, 3rd edition, 2008.
- [34] A. Yariv. *Quantum electronics*. Wiley, New York, 3rd edition, 1989.
- [35] A. Braun, G. Korn, X. Liu, D. Du, J. Squier, and G. Mourou. *Self-channeling of high-peak-power femtosecond laser pulses in air*. Optics Letters, 20(1):73, 1995.
- [36] E. Esarey, P. Sprangle, J. Krall, and A. Ting. *Self-focusing and guiding of short laser pulses in ionizing gases and plasmas*. IEEE Journal of Quantum Electronics, 33(11):1879–1914, November 1997.
- [37] L. Bergé, S. Skupin, R. Nuter, J. Kasparian, and J. Wolf. *Ultrashort filaments of light in weakly ionized, optically transparent media*. Reports on Progress in Physics, 70(10):1633–1713, 2007.
- [38] A. Couairon and A. Mysyrowicz. *Femtosecond filamentation in transparent media*. Physics Reports, 441(2-4):47–189, 2007.
- [39] S. Rae. *Ionization-induced defocusing of intense laser pulses in high-pressure gases*. Optics Communications, 97(1-2):25–28, 1993.
- [40] Y. Li and R. Fedosejevs. *Ionization-induced blue shift of KrF laser pulses in an underdense plasma*. Physical Review E, 54(2):2166–2169, 1996.
- [41] S. Skupin, L. Bergé, U. Peschel, and F. Lederer. *Interaction of femtosecond light filaments with obscurants in aerosols*. Physical Review Letters, 93(2), 2004.

- [42] W. Liu, J. Gravel, F. Théberge, A. Becker, and S. L. Chin. *Background reservoir: its crucial role for long-distance propagation of femtosecond laser pulses in air*. Applied Physics B, 80(7):857–860, 2005.
- [43] T. Xi, X. Lu, and J. Zhang. *Interaction of light filaments generated by femtosecond laser pulses in air*. Physical Review Letters, 96(2):025003, 2006.
- [44] S. Hosseini, et al. *Competition of multiple filaments during the propagation of intense femtosecond laser pulses*. Physical Review A, 70(3), 2004.
- [45] W. Liu, et al. *Experimental observation and simulations of the self-action of white light laser pulse propagating in air*. New Journal of Physics, 6:6–6, 2004.
- [46] H. Schroeder. *Visualization of the evolution of multiple filaments in methanol*. Optics Communications, 234(1-6):399–406, 2004.
- [47] R. Ackermann, et al. *Optimal control of filamentation in air*. Applied Physics Letters, 89(17):171117, 2006.
- [48] A. Zair, et al. *Spatio-temporal characterization of few-cycle pulses obtained by filamentation*. Optics Express, 15(9):5394, 2007.
- [49] D. Walter. *Adaptive Control of Ultrashort Laser Pulses for High-Harmonic Generation*. PhD thesis, Julius-Maximilians-Universität Würzburg, Experimentelle Physik I, Physikalisches Institut, 12 2006.
- [50] N. H. Burnett, H. A. Baldis, M. C. Richardson, and G. D. Enright. *Harmonic generation in CO₂ laser target interaction*. Applied Physics Letters, 31(3):172, 1977.
- [51] A. McPherson, et al. *Studies of multiphoton production of vacuum-ultraviolet radiation in the rare gases*. Journal of the Optical Society of America B, 4(4):595, 1987.
- [52] M. Ferray, A. L’Huillier, X. F. Li, L. A. Lompre, G. Mainfray, and C. Manus. *Multiple-harmonic conversion of 1064 nm radiation in rare gases*. Journal of Physics B: Atomic, Molecular and Optical Physics, 21(3):L31, 1988.
- [53] K. Burnett, V. C. Reed, and P. L. Knight. *Atoms in ultra-intense laser fields*. Journal of Physics B: Atomic, Molecular and Optical Physics, 26(4):561–598, 1993.
- [54] P. Corkum. *Plasma perspective on strong field multiphoton ionization*. Physical Review Letters, 71(13):1994–1997, 1993.
- [55] K. C. Kulander, K. J. Schafer, and J. L. Krause. *Dynamics of short-pulse excitation, ionization and harmonic conversion*. , In M. G. Blain and G. D. Tipton, (editors), "Super-intense laser-atom physics", NATO Workshop, Han-Sur-Lesse, Belgium, 8-14 Jan. 1993, New York, 1993. Plenum Press.

- [56] M. Lewenstein, P. Balcou, M. Ivanov, A. L’Huillier, and P. Corkum. *Theory of high-harmonic generation by low-frequency laser fields*. Physical Review A, 49(3):2117–2132, 1994.
- [57] P. B. Corkum and F. Krausz. *Attosecond science*. Nature Physics, 3(6):381–387, 2007.
- [58] F. Krausz and M. Ivanov. *Attosecond physics*. Reviews of Modern Physics, 81(1):163–234, 2009.
- [59] D. Schäfer, et al. *Compact x-ray microscopes for EUV- and soft x-radiation with spectral imaging capabilities*. In Proceedings of SPIE, pages 631704–631704–9, San Diego, CA, USA, 2006.
- [60] M. Benk, K. Bergmann, D. Schäfer, and T. Wilhein. *Compact soft x-ray microscope using a gas-discharge light source*. Optics Letters, 33(20):2359, 2008.
- [61] R. Sandberg, et al. *Lensless diffractive imaging using tabletop coherent High-Harmonic Soft-X-Ray beams*. Physical Review Letters, 99(9), 2007.
- [62] M. Wieland, T. Wilhein, C. Spielmann, and U. Kleineberg. *Zone-plate interferometry at 13 nm wavelength*. Applied Physics B: Lasers and Optics, 76(8):885–889, 2003.
- [63] M. Protopapas, C. H. Keitel, and P. L. Knight. *Atomic physics with super-high intensity lasers*. Reports on Progress in Physics, 60(4):389, 1997.
- [64] P. Antoine, A. L’Huillier, M. Lewenstein, P. Salières, and B. Carré. *Theory of high-order harmonic generation by an elliptically polarized laser field*. Physical Review A, 53(3):1725–1745, 1996.
- [65] L. V. Keldysh. *Ionization in the field of a strong electromagnetic wave*. Soviet Physics JETP, 20:1307–1314, 05 1965.
- [66] M. Ammosov, N. Delone, and V. Krainov. *Tunnel ionization of complex atoms and of atomic ions in an alternating electromagnetic field*. Soviet Physics Journal of Experimental and Theoretical Physics, 64(6):1191–1194, 12 1986.
- [67] E. Mevel, et al. *Atoms in strong optical fields: Evolution from multiphoton to tunnel ionization*. Physical Review Letters, 70(4):406–409, 1993.
- [68] T. Pfeifer. *Adaptive Control of Coherent Soft X-Rays*. PhD thesis, Julius-Maximilians-Universität Würzburg, Experimentelle Physik I, Physikalisches Institut, 06 2004.
- [69] J. Krause, K. Schafer, and K. Kulander. *High-order harmonic generation from atoms and ions in the high intensity regime*. Physical Review Letters, 68(24):3535–3538, 1992.

- [70] A. L’Huillier and P. Balcou. *High-order harmonic generation in rare gases with a 1-ps 1053-nm laser*. Physical Review Letters, 70(6):774–777, 1993.
- [71] J. Macklin, J. Kmetec, and C. Gordon. *High-order harmonic generation using intense femtosecond pulses*. Physical Review Letters, 70(6):766–769, 1993.
- [72] T. Zuo, A. Bandrauk, M. Ivanov, and P. Corkum. *Control of high-order harmonic generation in strong laser fields*. Physical Review A, 51(5):3991–3998, 1995.
- [73] T. Pfeifer, L. Gallmann, M. J. Abel, P. M. Nagel, D. M. Neumark, and S. R. Leone. *Heterodyne mixing of laser fields for temporal gating of High-Order harmonic generation*. Physical Review Letters, 97(16), 2006.
- [74] P. Raith, C. Ott, and T. Pfeifer. *Attosecond twin-pulse control by generalized kinetic heterodyne mixing*. Optics Letters, 36(2):283, 2011.
- [75] P. Balcou, P. Salières, A. L’Huillier, and M. Lewenstein. *Generalized phase-matching conditions for high harmonics: The role of field-gradient forces*. Physical Review A, 55(4):3204–3210, 1997.
- [76] A. L’Huillier, P. Balcou, S. Candel, K. Schafer, and K. Kulander. *Calculations of high-order harmonic-generation processes in xenon at 1064 nm*. Physical Review A, 46(5):2778–2790, 1992.
- [77] J. Tisch, R. Smith, J. Muffett, M. Ciarrocca, J. Marangos, and M. Hutchinson. *Angularly resolved high-order harmonic generation in helium*. Physical Review A, 49(1):R28–R31, 1994.
- [78] J. E. Muffett, C. G. Wahlstrom, and M. H. R. Hutchinson. *Numerical modelling of the spatial profiles of high-order harmonics*. Journal of Physics B: Atomic, Molecular and Optical Physics, 27(23):5693–5706, 12 1994.
- [79] P. Salières, A. L’Huillier, and M. Lewenstein. *Coherence control of High-Order harmonics*. Physical Review Letters, 74(19):3776–3779, 1995.
- [80] S. Saltiel, S. Tanev, and A. D. Boardman. *High-order nonlinear phase shift caused by cascaded third-order processes*. Optics Letters, 22(3):148, 1997.
- [81] R. Spitzenpfeil. *Enhancing the Brilliance of High-Harmonic Generation*. PhD thesis, Julius-Maximilians-Universität Würzburg, Experimentelle Physik I, Physikalisches Institut, in preparation.
- [82] D. Strickland and G. Mourou. *Compression of amplified chirped optical pulses*. Optics Communications, 56(3):219–221, 1985.
- [83] R. Kemmer. *Adaptive räumliche und zeitliche Formung von ultrakurzen Laserpulsen*. Diplomarbeit, Julius-Maximilians-Universität Würzburg, Experimentelle Physik I, Physikalisches Institut, 01 2005.

- [84] HAMAMATSU PHOTONICS. *Datasheet for SLM module: PPM X8267 series*. HAMAMATSU PHOTONICS K.K. Electron Tube Division, 04 2006.
- [85] HAMAMATSU PHOTONICS. *Datasheet for LCOS-SLM X10468 series*. HAMAMATSU PHOTONICS K.K. Central Research Laboratory, 06 2009.
- [86] Wikipedia, the free encyclopedia. *Optimization algorithms*. Published online. http://en.wikipedia.org/wiki/Optimization_algorithm. (2011-02-13, 10:07 UTC+01:00), 02 2011.
- [87] R. Judson and H. Rabitz. *Teaching lasers to control molecules*. Physical Review Letters, 68(10):1500–1503, 1992.
- [88] S. Eyring. *Konstruktion und Bau eines Spektrometers für den XUV-Bereich zur Charakterisierung von Hohen Harmonischen*. Diplomarbeit, Julius-Maximilians-Universität Würzburg, Experimentelle Physik I, Physikalisches Institut, 03 2006.
- [89] FEMTOLASERS Produktions GmbH. *User's manual for Dispersion Minimized Autocorrelator FEMTOMETER*. FEMTOLASERS Produktions GmbH, 10 2009.
- [90] R. Trebino, et al. *Measuring ultrashort laser pulses in the time-frequency domain using frequency-resolved optical gating*. Review of Scientific Instruments, 68(9):3277, 1997.
- [91] C. Iaconis and I. Walmsley. *Spectral phase interferometry for direct electric-field reconstruction of ultrashort optical pulses*. Optics Letters, 23(10):792, 1998.
- [92] A. Paulus. *Entwicklung und Bau eines Elektronenflugzeitspektrometers*. Diplomarbeit, Julius-Maximilians-Universität Würzburg, Experimentelle Physik I, Physikalisches Institut, 08 2004.
- [93] Andor[®] Technology. *User's Guide to the Andor Classic PCI CCD*. Andor[®] Technology, 2007.
- [94] M. Nisoli, S. D. Silvestri, and O. Svelto. *Generation of high energy 10 fs pulses by a new pulse compression technique*. Applied Physics Letters, 68(20):2793, 1996.
- [95] M. Nisoli, et al. *Compression of high-energy laser pulses below 5 fs*. Optics Letters, 22(8):522, 1997.
- [96] B. Schenkel, et al. *Generation of 3.8-fs pulses from adaptive compression of a cascaded hollow fiber supercontinuum*. Optics Letters, 28(20):1987, 2003.
- [97] S. L. Chin, S. Petit, F. Borne, and K. Miyazaki. *The white light supercontinuum is indeed an ultrafast white light laser*. Japanese Journal of Applied Physics, 38(Part 2, No. 2A):L126–L128, 1999.

- [98] M. Mlejnek, M. Kolesik, J. Moloney, and E. Wright. *Optically turbulent femtosecond light guide in air*. Physical Review Letters, 83(15):2938–2941, 1999.
- [99] O. Kosareva, et al. *Controlling a bunch of multiple filaments by means of a beam diameter*. Applied Physics B, 82(1):111–122, 2005. ISSN 0946-2171. <http://www.springerlink.com/index/10.1007/s00340-005-1958-3>.
- [100] G. Fibich, S. Eisenmann, B. Ilan, and A. Zigler. *Control of multiple filamentation in air*. Optics Letters, 29(15):1772, 2004.
- [101] T. D. Grow and A. L. Gaeta. *Dependence of multiple filamentation on beam ellipticity*. Optics Express, 13(12):4594, 2005.
- [102] D. Walter, S. Eyring, J. Lohbreier, R. Spitzenpfeil, and C. Spielmann. *Spatial optimization of filaments*. Applied Physics B, 88(2):175–178, 2007.
- [103] E. T. J. Nibbering, et al. *Conical emission from self-guided femtosecond pulses in air*. Optics Letters, 21(1):62, 1996.
- [104] X. Gu, S. Akturk, and R. Trebino. *Spatial chirp in ultrafast optics*. Optics Communications, 242(4-6):599–604, 2004.
- [105] A. Mysyrowicz, A. Couairon, and U. Keller. *Self-compression of optical laser pulses by filamentation*. New Journal of Physics, 10(2):025023, 2008.
- [106] T. Pfeifer, L. Gallmann, M. J. Abel, D. M. Neumark, and S. R. Leone. *Circular phase mask for control and stabilization of single optical filaments*. Optics Letters, 31(15):2326, 2006.
- [107] FEMTOLASERS Produktions GmbH. *User’s manual for Femtosecond Multipass Amplifier FEMTOPOWER Compact PRO*. FEMTOLASERS Produktions GmbH, 08 2003.
- [108] M. Mäder. *Nonlinear Frequency Conversion of Ti:Sapphire Laser Pulses for Spectroscopy*. Diplomarbeit, Julius-Maximilians-Universität Würzburg, Experimentelle Physik I, Physikalisches Institut, 02 2006.
- [109] C. P. Hauri, A. Trisorio, M. Merano, G. Rey, R. B. Lopez-Martens, and G. Mourou. *Generation of high-fidelity, down-chirped sub-10 fs mJ pulses through filamentation for driving relativistic laser-matter interactions at 1 kHz*. Applied Physics Letters, 89(15):151125, 2006.
- [110] G. Stibenz, N. Zhavoronkov, and G. Steinmeyer. *Self-compression of millijoule pulses to 7.8 fs duration in a white-light filament*. Optics Letters, 31(2):274, 2006.
- [111] J. Odnor, D. Romanov, and R. Levis. *Self-Shortening dynamics measured along a femtosecond laser filament in air*. Physical Review Letters, 105(12):125001, 2010.

- [112] T. Pfeifer, et al. *Spatial control of high-harmonic generation in hollow fibers*. Optics Letters, 30(12):1497, 2005.
- [113] T. Pfeifer, D. Walter, C. Winterfeldt, C. Spielmann, and G. Gerber. *Controlling the spectral shape of coherent soft x-rays*. Applied Physics B, 80(3):277–280, 2005.
- [114] R. Bartels, et al. *Shaped-pulse optimization of coherent emission of high-harmonic soft x-rays*. Nature, 406(6792):164–166, 07 2000.
- [115] D. H. Ko, K. T. Kim, J. Park, J. hwan Lee, and C. H. Nam. *Attosecond chirp compensation over broadband high-order harmonics to generate near transform-limited 63as pulses*. New Journal of Physics, 12(6):063008, 2010.
- [116] T. Pfeifer, C. Spielmann, and G. Gerber. *Femtosecond x-ray science*. Reports on Progress in Physics, 69(2):443–505, 2006.
- [117] C. Winterfeldt, C. Spielmann, and G. Gerber. *Colloquium: Optimal control of high-harmonic generation*. Rev. Mod. Phys., 80(1):117–140, 01 2008.
- [118] J. Lohbreier, S. Eyring, R. Spitzenpfeil, C. Kern, M. Weger, and C. Spielmann. *Maximizing the brilliance of high-order harmonics in a gas jet*. New Journal of Physics, 11(2):023016, 2009.
- [119] R. Spitzenpfeil, et al. *Enhancing the brilliance of high-harmonic generation*. Applied Physics A, 96(1):69–81, 2009.
- [120] J. Gautier, et al. *Optimization of the wave front of high order harmonics*. The European Physical Journal D, 48(3):459–463, 2008.
- [121] P. Mercère, et al. *Hartmann wave-front measurement at 13.4 nm with $\lambda_{EUV}/120$ accuracy*. Optics Letters, 28(17):1534, 2003.
- [122] C. Spielmann, et al. *Near-keV coherent x-ray generation with sub-10-fs lasers*. IEEE Journal of Selected Topics in Quantum Electronics, 4(2):249–265, 04 1998.
- [123] P. Salières, T. Ditmire, M. D. Perry, A. L’Huillier, and M. Lewenstein. *Angular distributions of high-order harmonics generated by a femtosecond laser*. Journal of Physics B: Atomic, Molecular and Optical Physics, 29(20):4771, 1996.
- [124] H. Merdji, M. Kovacev, W. Boutu, P. Salières, F. Vernay, and B. Carré. *Macroscopic control of high-order harmonics quantum-path components for the generation of attosecond pulses*. Physical Review A, 74(4), 2006.
- [125] L. L. Déroff, P. Salières, and B. Carré. *Beam-quality measurement of a focused high-order harmonic beam*. Optics Letters, 23(19):1544, 1998.

- [126] D. Yoshitomi, et al. *Phase-matched enhancements of high-harmonic soft x-rays by adaptive wave-front control with a genetic algorithm*. Applied Physics B: Lasers and Optics, 78(3-4):275–280, 2004.
- [127] P. Villorosi, et al. *Optimization of high-order harmonic generation by adaptive control of a sub-10-fs pulse wave front*. Optics Letters, 29(2):207, 2004.
- [128] B. Henke, E. Gullikson, and J. Davis. *X-Ray Interactions: Photoabsorption, Scattering, Transmission, and Reflection at $E = 50\text{--}30,000$ eV, $Z = 1\text{--}92$* . Atomic Data and Nuclear Data Tables, 54(2):181–342, 1993. http://henke.lbl.gov/optical_constants/.
- [129] S. Eyring. *Extended Manual for McPherson 248/310G and LabVIEW software*. Institute for Optics and Quantum-electronics, Friedrich-Schiller University Jena, 09 2010.
- [130] J. Henneberger. *Aufbau eines Mikrotropfensystems für die Erzeugung von XUV-Strahlung mit ultrakurzen Laserpulsen*. Diplomarbeit, Julius-Maximilians-Universität Würzburg, Experimentelle Physik I, Physikalisches Institut, 08 2008.
- [131] W. Martin, A. Musgrove, S. Kotochigova, and J. Sansonetti. *Ground levels and ionization energies for the neutral atoms*. NIST Standard Reference Database 111, 07 2010. http://www.nist.gov/pml/data/ion_energy.cfm.
- [132] A. B. Bhatia, E. Wolf, and M. Born. *On the circle polynomials of zernike and related orthogonal sets*. Mathematical Proceedings of the Cambridge Philosophical Society, 50(01):40–48, 1954.
- [133] R. J. Noll. *Zernike polynomials and atmospheric turbulence*. Journal of the Optical Society of America, 66(3):207–211, 1976.
- [134] V. N. Mahajan. *Zernike annular polynomials for imaging systems with annular pupils*. Journal of the Optical Society of America, 71(1):75–85, 1981.
- [135] W. Swantner and W. W. Chow. *Gram-Schmidt orthonormalization of zernike polynomials for general aperture shapes*. Applied Optics, 33(10):1832, 1994.
- [136] ZEMAX[®] – Optical Design Program. *User's Manual*. ZEMAX Development Corporation, 04 2010.
- [137] K. Weicker. *Evolutionäre Algorithmen*. Teubner, Wiesbaden, 2nd edition, 2007.
- [138] McPherson, Inc. *Instruction Manual – Model 248/310 Grazing Incidence Monochromator*. McPherson, Inc., 12 2009.
- [139] McPherson, Inc. *Instruction Manual – Model 789A-3 Scan Controller*. McPherson, Inc., 12 2009.

-
- [140] Directed Energy, Inc. *PVX-4150 Pulse Generator – Operation Manual*. DEI Inc., 12 2009.
- [141] X-Ray and Specialty Instruments, Inc. *Users’s Manual for BrightView Model XUV-2040*. XSI Inc., 12 2009.
- [142] Wikipedia, the free encyclopedia. *Phosphor*. Published online. <http://en.wikipedia.org/wiki/Phosphor>. (2010-09-21, 12:15 UTC+02:00), 09 2010.
- [143] Andor[®] Technology. *User’s Guide to Andor iDus*. Andor[®] Technology, 2008.
- [144] Wikipedia, the free encyclopedia. *Epoch (reference date)*. Published online. [http://en.wikipedia.org/wiki/Epoch_\(reference_date\)](http://en.wikipedia.org/wiki/Epoch_(reference_date)). (2010-09-03, 12:58 UTC+02:00), 09 2010.

List of Figures

1.1	Gaussian beam width, beam divergence and wavefront curvature.	9
1.2	Influence of \mathcal{M}^2 on beam width and divergence.	12
1.3	A “non-Gaussian” Gaussian beam.	14
2.1	Thin lens altering the wavefront of an incident beam.	16
2.2	Influence of aberrations on beam propagation.	17
2.3	Concept of the early Hartmann test as used in astronomy.	19
2.4	Concept of the Shack–Hartmann sensor.	21
2.5	Concept of the Hartmann sensor.	23
4.1	The effect of self-phase modulation.	34
4.2	The effects which lead to filamentation.	37
5.1	The different regimes of high-order harmonic generation.	39
5.2	The three-step-model of high-order harmonic generation.	40
5.3	Possible ionization scenarios.	41
5.4	Illustration of the two different quantum paths.	46
6.1	Overview of the experimental setup.	57
6.2	The laser system.	58
6.3	The Hamamatsu PPM-SLM.	59
6.4	The Hamamatsu LCOS-SLM	60
6.5	High-order harmonic generation in a gas-filled nickel tube.	63
6.6	The vacuum setup.	64
7.1	The filamentation setup.	66
7.2	Picture of the actual filament.	67
7.3	Beam profile after filamentation (VIS and IR).	68
7.4	Evaluation of spatial chirp.	69
7.5	Beam profile before and after optimization.	71
7.6	Spectrum and spatial chirp before and after optimization.	72
7.7	Phase mask and calculated beam profile after optimization.	73
7.8	Optimized high-order harmonic spectrum after filamentation.	74
8.1	Setup for measuring the wavefronts of high-order harmonics.	76
8.2	The Hartmann mask.	77
8.3	Typical spectrum of high-order harmonics.	78
8.4	Example of a wavefront measurement with high-order harmonics.	79
8.5	Intensity/divergence plotted vs. pressure.	81
8.6	Astigmatism plotted vs. pressure	82

8.7	Intensity/divergence plotted vs. z -position	83
8.8	Astigmatism plotted vs. z -position	84
8.9	Beam profile and wave aberration of high-order harmonic beam	85
9.1	Setup for wavefront controlled high-order harmonic generation.	88
9.2	XUV transmission of thin metallic filters.	89
9.3	Evolution of fitness during optimization.	91
9.4	Spectrum of high-order harmonics before and after optimization.	92
9.5	Beam profile of the reference beam and the optimized beam (from Shack-Hartmann data).	93
9.6	Measured beam profile of the reference beam.	94
9.7	Phase-mask applied to SLM to create optimized beam.	95
9.8	Calculated and measured beam profiles of the optimized beam.	96
B.1	Plot of the Zernike polynomial Z_4	112
B.2	The radius of curvature R of a beam.	113
B.3	Plots of the Zernike polynomials Z_3 and Z_5	114
B.4	Effect of the 45° astigmatism and the 90° astigmatism on a Gaussian beam.	115
C.1	Comparison between binning and tiltable planes	119
C.2	Example of a phase mask created by the genetic algorithm using Zernike polynomials	120
D.1	The McPherson 248/310G XUV spectrometer.	121
D.2	Principle of the Rowland Circle.	122
D.3	Effect of spectral foreshortening.	123
D.4	Principle of an imaging Rowland circle spectrometer.	124
D.5	Rowland circle spectrometer in generalized configuration.	126
D.6	User interface of the McPherson software.	129
D.7	User interface of the ASDX-Viewer&Converter software.	130

List of Tables

9.1	Parameters of the genetic algorithm used for wavefront optimization.	91
B.1	Zernike polynomials in Cartesian coordinates.	111